공학박사학위논문

Numerical Study on Plenum Mixing Chamber and Diffusers of Arc-Heated Wind Tunnel and Predicting Correlation between Arc-Heater Parameters using Multi-Layer Perceptron

아크 가열식 풍동의 플레넘 혼합실과 디퓨저에 대한 수치적 연구 및 멀티 레이어 퍼셉트론을 이용한 아크히터 변수들의 상관 관계 예측

2023년 2월

서울대학교 대학원
기계항공공학부
백 진 솔

공학박사학위논문

Numerical Study on Plenum Mixing Chamber and Diffusers of Arc-Heated Wind Tunnel and Predicting Correlation between Arc-Heater Parameters using Multi-Layer Perceptron

아크 가열식 풍동의 플레넘 혼합실과 디퓨저에 대한 수치적 연구 및 멀티 레이어 퍼셉트론을 이용한 아크히터 변수들의 상관 관계 예측

2023년 2월

서울대학교 대학원
기계항공공학부
백 진 솔

Numerical Study on Plenum Mixing Chamber and Diffusers of Arc-Heated Wind Tunnel and Predicting Correlation between Arc-Heater Parameters using Multi-Layer Perceptron

Advisor: Prof. Kyu-Hong Kim

Submitting a Ph.D. Dissertation of Engineering

November 2022

Graduate School of Engineering
Seoul National University
Mechanical and Aerospace Engineering

Jinsol Baek

Confirming the Ph.D. Dissertation written by
Jinsol Baek

December 2022

Chair	Prof. Chongam Kim
Vice Chair	Prof. Kyu-Hong Kim
Examiner	Prof. Kwanjung Yee
Examiner	Prof. Hyungrok Do
Examiner	Dr. Jae-Jung Na

Numerical Study on Plenum Mixing Chamber and Diffusers of Arc-Heated Wind Tunnel and Predicting Correlation between Arc-Heater Parameters using Multi-Layer Perceptron

아크 가열식 풍동의 플레넘 혼합실과 디퓨저에 대한 수치적 연구 및 멀티 레이어 퍼셉트론을 이용한 아크히터 변수들의 상관 관계 예측

지도교수 김 규 홍

이 논문을 공학박사 학위논문으로 제출함

2022년 11월

서울대학교 대학원

기계항공공학부

백 진 솔

백진솔의 공학박사 학위논문을 인준함

2022년 12월

위 원 장	김 종 암
부위원장	김 규 홍
위 원	이 관 중
위 원	도 형 록
위 원	나 재 정

Abstract

An essential ground test facility for research on heat-resistant materials and thermal protection systems of hypersonic flight vehicles and re-entry vehicles is an arc-heated wind tunnel that generates high enthalpy flow using arc plasma. Research on the arc-heated facilities has been conducted since the 1950s to secure the safety of manned spacecraft, and advanced countries in aerospace industries such as the United States, Europe, and Russia have built facilities of various sizes and have been using them until now. However, few arc-heated wind tunnels exist in the Republic of Korea; therefore, it is required to build a new facility, and upgrade the exist facility using the infrastructure of research institute reducing construction costs. In addition, overseas facilities are also constantly in need of improvement to conduct re-entry research on other planets. Therefore, in this study, to be useful in the design, improvement, and expansion of arc-heated facilities, studies on a computational analysis program, preliminary configuration design, and performance analysis studies using an artificial neural network model are conducted. The specific contents are as follows.

1.Improve and validate flow analysis program

The ARCFLO4, a code for an arc-heater analysis, is improved, verified, and validated as an analysis code for an entire arc-heated wind tunnel. The ARCFLO4 code for high-pressure, high-temperature, and low-velocity thermal/chemical equilibrium arc plasma analysis has been improved by expanding the computation region of thermodynamic properties and transfer coefficients to enable flow analysis in the supersonic/hypersonic region of arc-heated wind tunnels. In addition, the dual time stepping time integration method for unsteady flow analysis is adopted. The improved flow analysis program is verified and validated by comparing the numerical results and experimental values of the JAXA 0.75 MW arc-heater, NASA Ames 20 MW IHF

arc-heater, and NASA Langley's Mach 4.9 and Mach 6 nozzles.

2. Configuration proposal and flow analysis on plenum mixing chamber and diffuser

A plenum mixing chamber with a heater nozzle was proposed to ensure the stability of the arc plasma according to the flow change inside the chamber when there is additional flow injection into the chamber. Even if the flow inside the plenum mixing chamber changes, it was confirmed that there is no flow change inside the arc heater due to the choking effect by the heater nozzle, and it was found that the mixing of the high-temperature heater flow and the room-temperature additional flow occurred in shorter length. In the numerical study on the diffusers, flow analysis was performed on the representative diffuser types; the center-body diffuser and the second throat cylindrical diffuser, and after identifying the advantages and disadvantages of each type, a novel diffuser configuration was proposed. In the case of the novel diffuser that the center body is located in the subsonic region, it was confirmed that the diffuser efficiency was maintained and the flow temperature at the exit was the lowest due to the increase in the cooling area.

3. Predicting correlation between arc-heater parameters using multi-layer perceptron

A code for predicting the performance of an arc-heated wind tunnel is developed using the multi-layer perceptron model. Databases were built using the numerical results of segmented arc-heaters, and major design variables were selected through flow analysis; then training was performed to predict the correlation between arc heater parameters. For verification of the multi-layer perceptron model, the predicted pressure, arc voltage, enthalpy, and efficiency, which are performance parameters of arc-heater, are compared with experimental values of existing arc-heaters in various sizes.

Keywords: Arc-heated wind tunnel, Computational fluid dynamics (CFD), Arc-Heater, Plenum mixing chamber, Diffuser, Multi-layer perceptron

Student Number: 2017-34718

Name: Baek, Jin-sol

Contents

Abstract **i**

Contents **iv**

List of Tables **vii**

List of Figures **ix**

1 INTRODUCTION **1**

1.1 Introduction to Arc-heated Wind Tunnel 1

1.2 Research Status of Arc-Heated Wind Tunnel 7

1.3 Outline of Thesis 10

1.3.1 Motivation and objectives 10

1.3.2 Outline of chapters 11

2 MATERIALS AND METHODS **12**

2.1 Analysis Program Overview 12

2.1.1 Summary of physical models and boundary conditions 13

2.1.2 Flow chart and numerical schemes 15

2.2 Physical Modeling 16

2.2.1 Governing equations 16

2.2.2 Thermodynamic properties and transport coefficients 18

2.2.3 Joule heating models 25

2.2.4 Radiation model 29
2.2.5 Turbulence models 35
2.3 Numerical Methods 40
2.3.1 Flux schemes 40
2.3.2 Time integration schemes 44
2.4 Boundary Conditions 48
2.4.1 Wall boundary conditions 48
2.4.2 Inflow conditions 50
2.4.3 Outflow conditions 52
2.4.4 Axisymmetric boundary condition 52
2.4.5 Injection boundary condition 53
2.5 Validation and Verification 54
2.5.1 High pressure and high temperature arc flow 54
2.5.2 Supersonic/Hypersonic flow 60

3 NUMERICAL ANALYSIS AND INVESTIGATION 63

3.1 Plenum Mixing Chamber with a Heater Nozzle 64
3.1.1 Arc-heater and plenum mixing chamber 64
3.1.2 Plenum mixing chamber with heater nozzle 65
3.1.3 Results and analysis depending on additional injection flow rate and direction 78
3.1.4 Parametric study on heater nozzle 86
3.2 Diffusers in Various Types 92
3.2.1 General diffusers 92
3.2.2 A novel diffuser 106
3.2.3 Performance evaluation of diffusers 110

4 PREDICTING CORRELATION USING MULTI-LAYER PERCEPTRON **121**
4.1 Multi-Layered Perceptron (MLP) 123
4.2 Predicting Correlation between Arc-Heater Parameters 126
4.2.1 Database building 126
4.2.2 MLP training information 130
4.2.3 Performance prediction 131
4.3 An Example of Sizing a Segmented Type Arc-Heater 139

5 CONCLUSIONS **144**
5.1 Conclusion 144
5.2 Future Works 147

Abstract (In Korean) **157**

List of Tables

1.1 Arc-heated facilities of the world 8

2.1 Configuration information of AHSTF nozzles 60

2.2 Experimental results of AHSTF nozzles 61

3.1 Specification and analysis condition of the PM 67

3.2 Case information of additional injection 78

3.3 Heater performaces for all cases 79

3.4 Case information of heater nozzles 86

3.5 Total pressure and ratio of parametric study 88

3.6 Specification of diffusers 93

3.7 Specification of the novel diffuser 106

3.8 Location of the final shock wave 111

4.1 Input parameters and values for MLP training 127

4.2 MLP training information for pressure prediction 130

4.3 MLP training information for other performance parameters 130

4.4 Comparing JAXA 0.75 MW heater results (Pressure) 132

4.5 Comparing AEDC 5 MW heater results (Pressure) 133

4.6 Comparing NASA 60 MW IHF heater results (Pressure) 134

4.7 Comparing JAXA 0.75 MW heater results (Arc-voltage, Mass averaged enthalpy and efficiency) 135

4.8 Comparing AEDC 5 MW heater results (Arc-voltage, Mass averaged enthalpy and efficiency) 136
4.9 Comparing NASA 60 MW IHF heater results (Arc-voltage, Mass averaged enthalpy and efficiency) 137
4.10 Average error comparison between scaling study and MLP results, [%] 138

List of Figures

1.1 Schematic of general supersonic/hypersonic wind tunnel facility . . . 2

1.2 Reservoir System of wind tunnels 3

1.3 Wind tunnel capabilities [1] 3

1.4 Pressure and enthalpy envelop of arc-heaters [2] 5

1.5 Types of arc-heaters 6

1.6 Timeline of arc-heated wind tunnels 8

2.1 Physical models and boundary conditions of an arc-heated wind tunnel 14

2.2 Flow chart of the analysis program 15

2.3 Boundary and undervalue of polynomial formula and table 24

2.4 An example of current distribution along the axis 27

2.5 Cylindrical coordinate system for the radiation model 30

2.6 Schematic of the $k\omega - SST$ model 37

2.7 Left(L) and right(R) values at a computation cell interface 40

2.8 An example of inflow condition from saved data 51

2.9 JAXA 0.75 MW heater results 56

2.10 20 MW AHF heater results 59

2.11 NASA AHSTF supersonic/hypersonic nozzle exit results 62

3.1 Schematic of an arc-heater with plenum mixing chamber 64

3.2 Schematic of an arc-heater with plenum mixing chamber and heater nozzle 65
3.3 General PM configuration and computational domain 66
3.4 PM with heater nozzle configuration and computational domain . . . 66
3.5 Pressure results of two PM cases 69
3.6 Temperature results of two PM cases 70
3.7 Mach number results of two PM cases 71
3.8 Radial temperature distributions along the axis 75
3.9 Total pressure results of two PM cases 77
3.10 Temperature and streamlines inside the PM 81
3.11 Radial temperature distributions of various inject cases 83
3.12 Radial temperature distributions inside the heater 85
3.13 Averaged total pressure results of heater nozzle parametric study . . . 87
3.14 Heat flux at the heater nozzle throat 89
3.15 Radial temperature distributions of parametric study cases 91
3.16 Configuration of general diffusers 92
3.17 Computational domain of the center-body diffuser 94
3.18 Pressure contour and averaged total pressure of converging section . . 97
3.19 Averaged results along the converging section axis 99
3.20 Pressure contour and averaged total pressure of throat section 100
3.21 Averaged results along the throat section axis 102
3.22 Pressure contour and averaged total pressure of diverging section . . . 103
3.23 Averaged results along the diverging section axis 105
3.24 Configuration of a novel diffuser 106
3.25 Pressure contours of the novel diffuser in various back pressures . . . 107
3.26 Averaged results along the novel diffuser axis 109
3.27 Averaged wall pressure of diffusers in various back pressure 113
3.28 Averaged temperature of diffusers in various back pressure 117

3.29 Exit temperature and enthalpy of diffusers in various back pressure . . 118
3.30 Exit velocity and deceleration rate of diffusers in various back pressure 120

4.1 Outline of the multi-layered perceptron 123
4.2 ReLU function 124
4.3 Overview and calculation method of Adam 125
4.5 Database of segmented arc-heaters 129
4.6 Relation of current and enthalpy using scaling study 140
4.7 Inputs and outputs of predicting heater pressure using MLP (Example case) 142
4.8 Inputs and outputs of predicting heater parameters using MLP (Example case) 143

CHAPTER 1. INTRODUCTION

1.1 Introduction to Arc-heated Wind Tunnel

In aerospace engineering, supersonic and hypersonic wind tunnels are experimental facilities that simulate the flight environment of a vehicle on the ground and predict the actual flight performance of a vehicle at a lower cost than flight tests. Generally, as shown in Figure 1.1, it consists of a reservoir, a nozzle, a test-section, a pressure recovery system, and a vacuum chamber. The reservoir is a device that stores or creates an experimental flow, and experiment conditions are determined by its pressure and temperature of it. The nozzle expands and accelerates the high-pressure flow inside the reservoir to the supersonic/hypersonic flow required for an experiment. The test-section is where the model and material of a flight vehicle are located to experience the experimental flow, and actual measurements are done inside. The pressure recovery system usually consists of a diffuser and a heat exchanger, and of these, the diffuser is an essential device. The diffuser is connected to the test-section to capture the supersonic/hypersonic experimental flow, and a continuous shock wave is generated to decelerate and compress the flow aerodynamically. The vacuum chamber is located at the rearmost part of the test device to make the test-section in a vacuum state for simulating the high-altitude environment before the experiment, and during the test, the flow accumulates and prevents the low-pressure high-speed flow from being discharged directly into the atmosphere.

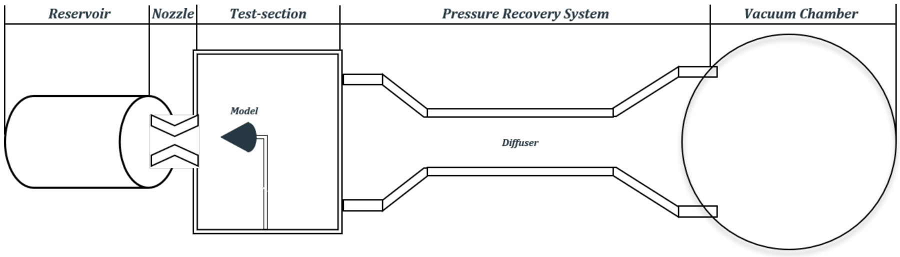

Figure 1.1: Schematic of general supersonic/hypersonic wind tunnel facility

Supersonic and hypersonic wind tunnels can be divided into blowdown wind tunnels, shock tube tunnels, and arc-heated wind tunnels as shown in Figure 1.2 according to the method of generating and storing reservoir flow. The flow duration time, temperature, and velocity characteristics of wind tunnels are shown in Figure 1.3 [1]. The blowdown wind tunnel uses a compressor to compress the working gas into a compression tank; then, the stored high-pressure gas blows down to the nozzle when the pressure valve is open. The gas temperature inside the compression tank can increase using a heater, yet the stagnation temperature is lower than that of the arc-heated wind tunnel. The shock tube wind tunnel divides a long tube into two spaces, increasing the gas pressure in one tube and lowering the pressure in the other tube, and using this pressure difference to create high-velocity flow. It is characterized by a high stagnation temperature of the experimental flow due to the initial shock caused by the pressure difference; however, it has a very short duration time. The arc-heated wind tunnel (i.e., Plasma wind tunnel) creates a high-temperature, high-pressure flow using an arc generator connected to a power supply, and it can simulate the high enthalpy flow that a supersonic/hypersonic flight vehicle experiences. The arc-heated wind tunnel can stably maintain high enthalpy flow for a long time compared to other wind tunnels; therefore, it is used for research on the thermal protection system (TPS) and ablation phenomenon of materials.

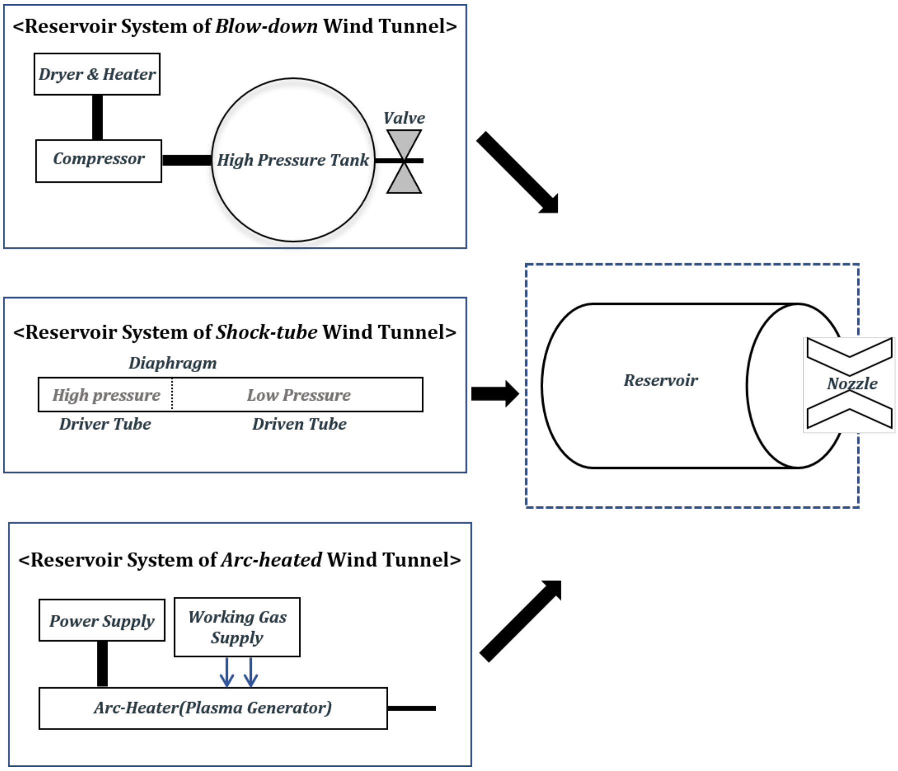

Figure 1.2: Reservoir System of wind tunnels

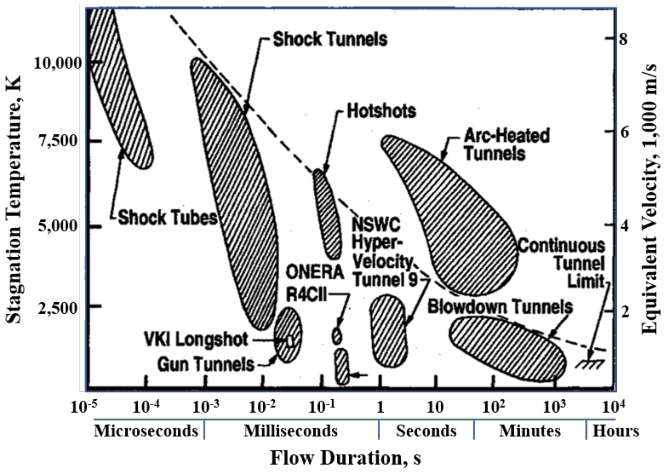

Figure 1.3: Wind tunnel capabilities [1]

An arc-heater is the most important equipment of the arc-heated facility because the experimental flow range varies depending on its type and size of it. The arc-heater generates high-temperature plasma using the anode and cathode's discharge effect, creating the high-temperature and high-pressure reservoir condition of the wind tunnel. Arc-heaters are generally divided into four types: Segmented, Hules, Induced Coupled Plasma (ICP), and MPD according to the high-temperature plasma generation method and configuration. Typical enthalpy and pressure characteristics that each heater can generate are shown in Figure 1.4. In the segmented arc heater, as shown in Figure 1.5a, electrodes are located on both sides of the constrictor tube, and current flows through it. Then, the current makes working gas discharged creating high-temperature plasma. The biggest feature of the segmented heater is that the generated arc is attached to both electrodes so that the arc length is fixed, and the constrictor tube is made up of packs of disks that can be attached and detached, and the length and power of the arc can be adjusted. Representative wind tunnels using segmented arc-heaters are the National Aeronautics and Space Administration (NASA) Ames Interaction Heating Facility (IHF) [3] and Aerodynamic Heating Facility (AHF) [3]. The Huels-type arc-heater has a relatively simple shape and is shown in Figure 1.5b. The electrodes are long tubular and are separated by swirl chambers, and working gas is injected between them. Unlike segmented-type heaters, Huels-type heaters do not have a fixed arc length, and arcs are naturally formed depending on operating conditions such as flow rate, pressure, and current, and can be attached anywhere on the tubular electrode. The arc can be attached to the electrode at the position of a magnetic coil to stabilize the arc. Representative Huels arc-heater facilities are the Arnold Engineering Development Complex (AEDC) H-2 [4] and NASA Langley's Arc Heated Scramjet Test Facility (AHSTF) [5]. The configuration of the Induced Coupled Plasma (ICP) heater is shown in Figure 1.5c, and it uses the electromagnetic field generated from the coil connected to the radio frequency (RF) generator to heat the working gas. Because there are no electrodes inside the flow (no plasma pollution), it is possible to research catalytic behavior and reactive gases. The University of Stuttgart Institute of Space Systems (IRS)'s PWK3 [6] and Belgium's Von Karman Institute (VKI)'s Plasmatron [7] are representative devices using ICP heaters. The Magneto Plasma Dynamic (MPD) heater, operating the same principle as the MPD thruster, is shown in Figure 1.5d. Unlike other heaters in which the heated working gas flows in and accelerates through the nozzle, electrodes are located at the inlet and end of the nozzle, so the ionized working gas is accelerated through the nozzle and electric/magnetic field. It is known that IRS' PWK 1 and 2 [8] use MPD heaters.

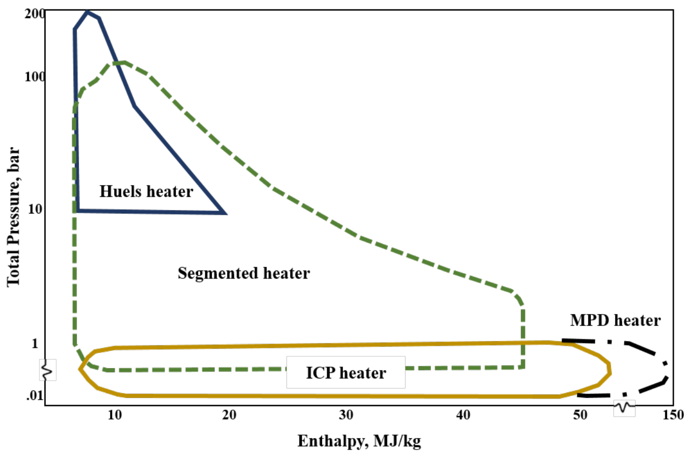

Figure 1.4: Pressure and enthalpy envelop of arc-heaters [2]

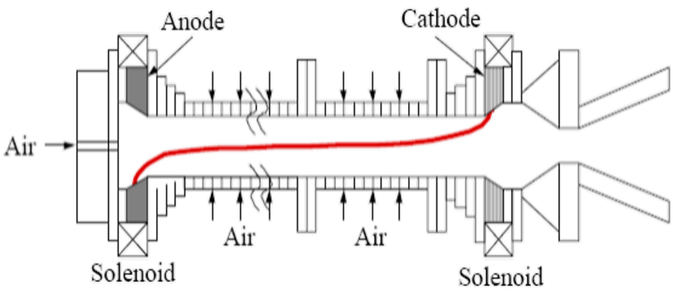

(a) Segmented type

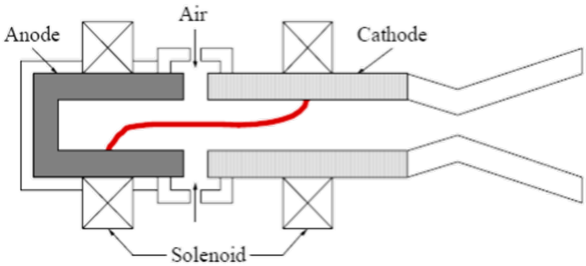

(b) Huels type

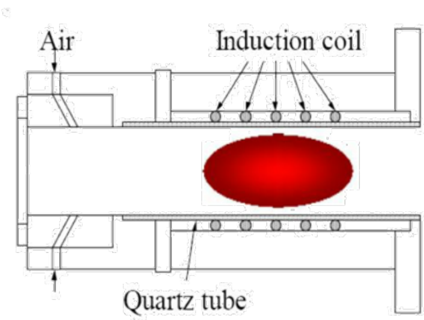

(c) ICP type

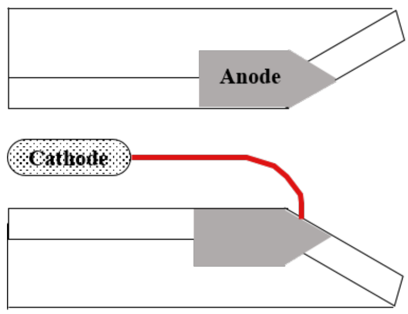

(d) MPD type

Figure 1.5: Types of arc-heaters

1.2 Research Status of Arc-Heated Wind Tunnel

Arc-heated wind tunnel facility has been studied since the 1950s to ensure the safety of a manned spacecraft's earth escape and re-entry, and devices were manufactured and operated from small-scale heaters in the 1960s. [1] Table 1.1 summarizes the operating facility status of advanced countries in aerospace so far. In the United States, various institutions centered on NASA have more than 10 arc-heated facilities of various sizes and types ranging from several kW to several tens of MW. Europe also has more than 10 facilities, including German Aerospace Center (DLR) L2K, L3K, and IRS's PWK series. Russia also has arc-heated facilities of various sizes, and Japan is known to own three devices by the Japan Aerospace Exploration Agency (JAXA). Recently, China's Aerodynamics Research and Development Center (CARDC) has one arc-heated facility each for small, medium, and large sizes. [9] The main development timeline of the arc-heated wind tunnels is summarized and shown in Figure 1.6. Various arc-heated facilities were actively researched and produced until the 1980s and 1990s, and they are currently in the trend of optimizing existing facilities or upgrading research that expands the operating area. In the Republic of Korea, along with Japan and China, interest in the development of hypersonic flight vehicles and heat-resistant materials is increasing; therefore, the demand for research, design, and construction of arc-heated facilities is steadily rising.

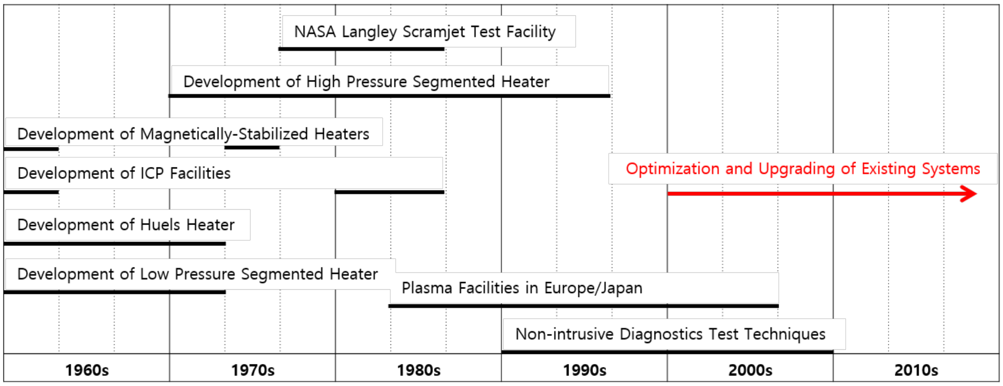

Figure 1.6: Timeline of arc-heated wind tunnels

Table 1.1: Arc-heated facilities of the world

	USA	Europe	Russia	Asia
Number of facilities	10 <	10 <	10 <	6 <
Representative Facilities	▶ NASA Ames AHF, IHF, RFD, PTF ▶ NASA Langley AHSTF ▶ AEDC H-Series ▶ Boeing LCAT	▶ DLR L2K, L3K ▶ IRS PWK1, 2, 3 ▶ CIRA Scirocco GHIBLI ▶ Von Karman VKI	▶ TsNIMASH TT1, TT2, T-1, T-2 ▶ Inst. for Prob. of Mechanics IPG3, 4 ▶ TsAGI VTS	▶ JAXA Plasma wind tunnels ▶ CARDC FD-Series

As various arc-heated wind tunnels have been operated for more than 60 years, enormous experimental research has been conducted. Large numbers of TPS materials have been developed, and research on the development and improvement of measurement and observation equipment could also have been conducted. Meanwhile, Computation equipment has also advanced and the level of computational fluid dynamic (CFD) has risen, and the results of computational analysis have been used to supplement the experimental results that were only made with observation and measurement. As a result, the physical phenomena occurring in the experiments are now better understood. Moreover, it is possible to design and evaluate wind tunnels using CFD. For instance, Pugazenthi et al. [10] identified the tendency of wind tunnel performance for the design parameters of plasma wind tunnel diffuser using numerical analysis and conducted a design guide study. Jung [11] conducted research on the design and manufacture of an arc heater device using CFD analysis. Recently, Agostinelli et al. [12] redesigned the diffuser of the GHIBLI plasma wind tunnel through aerothermodynamic analysis, and Foulade and Farahani [13] numerically investigated the correlation between nozzle internal flow and wind tunnel performance. General CFD analysis of a wind tunnel can be performed through a commercial analysis program (i.e., ANSYS fluent, STAR CCM, etc.), but to study the detailed and complex physical phenomena that occur in arc-heated wind tunnels such as high-temperature plasma flow with chemical reaction and supersonic/hypersonic flow with shock-shock and shock-boundary interaction, it is better to use in-house codes including high-accuracy physical models and numerical techniques. ARCFLO series is a representative in-house code for an arc-heater analysis. ARCFLO was developed by Nicolet et al. [14], and improvements have been made. The viscous effect is considered by Kim et al. [15], and Sakai et al. [16] included radiative heat transfer model for this high-temperature plasma to ARCFLO. The most recent ARCFLO code is ARCFLO4, which was developed by Lee et al. [17] to account for turbulence using the two equation Reynolds Averaged Navier-Stokes (RANS) equation, and it also considered the mixture of air and shield gas. [18]

1.3 Outline of Thesis

1.3.1 Motivation and objectives

There is a continuing need for upgrades and optimization of arc-heated wind tunnels because of the obsolescence of 1950s and 60s devices and the development of re-entry objects to other planets in the solar system. Especially, since arc-heated facilities are rare in the Republic of Korea, demand for research to build arc-heated facilities arises as interest in space development increases. Research on arc-heated wind tunnel design and improvement using CFD analysis can identify the operation range of existing equipment, and optimal design of facilities is possible. In addition, by simulating the experiment, the normal operation and the flow duration of the wind tunnel are identified to enable efficient experiments. Then, after the experiment, it is possible to obtain high-accuracy research results by analyzing physical phenomena such as similarity problems and boundary layer effects in a wind tunnel by complementing the experimental values.Moreover, since research using machine learning or artificial intelligent (AI) is being actively conducted in various fields, arc-heated wind tunnel study using CFD has advantages in building a numerical simulation result database for wind tunnel design or performance evaluation, and verifying necessary results. Therefore, the present study has the following objectives to help with the design, performance evaluation, and research of an arc-heated wind tunnel.

Objectives

1. Improve and verify the analysis program for time-efficient initial design, performance evaluation, and identification of the experiments range in an arc-heated wind tunnel.

2. Suggest a method to ensure arc-plasma stability because research on the arc heater itself is highly important in the absence of a medium and large-scale arc-heated facility in republic of Korea.

3. Introduce a diffuser configuration that can mitigate the performance of the vacuum system (heat exchanger, vacuum chamber) to increase the power of the arc heater, which is a major component in a situation where the total power of the arc-heated facility is limited.

4. Present and verify a time-efficient and highly accurate arc-heater initial sizing method

1.3.2 Outline of chapters

Chapter 2, “Materials and methods”, describes the analysis program, such as the physical models and numerical techniques used for the analysis of an arc-heated wind tunnel and components of the facility. The governing equations, thermal and chemical equilibrium gas calculation, Joule heating and radiation for arc plasma analysis, and turbulence models are explained, and the discretization and solution of the physical models for computational analysis are introduced. In addition, validation and verification results for arc-heated wind tunnel analysis are included.

In chapter 3, “Numerical analysis and investigation”, numerical analysis on the plenum mixing chamber with heater nozzle and diffusers of an arc-heated wind tunnel is performed. The heater nozzle is used to stabilize arc plasma inside the arc-heater using choking effect of nozzle throat. In addition, in this chapter, diffusers of representative types in arc-heated wind tunnel are numerically investigated, and a novel configuration that can compensate disadvantaged of the typical diffusers.

Chapter 4, “Predicting correlation using multi-layer perceptron”, describes the artificial neural network model for predicting performance parameters of a segmented arc-heater. The multi-layered perceptron model is used for training correlation between parameters of the heater. To validate trained prediction model, various sizes of arc-heaters results are compared with experimental values; then, an example of sizing a segmented arc-heater is described in this chapter.

CHAPTER 2. MATERIALS AND METHODS

The numerical analysis program for an arc-heated wind tunnel is structured finite volume method (FVM) in-house code based on Fortran [19] language. Based on the ARCFLO4 [17] code for arc-heater analysis, the code is improved and verified through this study to enable analysis of hypersonic nozzles, test-sections, diffusers, and vacuum chambers.

2.1 Analysis Program Overview

Complex physical phenomena occur inside an arc-heated wind tunnel, and various physical models and numerical techniques are required in the analysis program to simulate them. In the present study, the analysis program uses various physical models, numerical schemes, and boundary conditions, from Joule heating and radiative heat transfer by high-temperature plasma generated inside the arc heater to simulation of the cooling effect by the wall of the device. In this section, to see the various models and methods at a glance, the physical model and boundary conditions used in each component analysis are summarized in Figure 2.1, and a flow chart (Figure 2.2) is provided to understand each calculation step of the analysis program. Detailed descriptions of the physical models and numerical methods are written in the following sections (sections 2.2 and 2.3), respectively.

2.1.1 Summary of physical models and boundary conditions

Basically, the analysis program uses two-dimensional or axisymmetric Navier-Stokes Equations as the governing equation, and the two-equation Reynolds averaged Navier-Stokes (RANS) models are used as the turbulence model. The flow is assumed to be thermally and chemically equilibrium state; then, the thermodynamic properties and transport coefficients are calculated by using a polynomial formula or by interpolating tables of values calculated using statistical thermodynamics. In the case of low temperature and high Mach number flow that exceeds the calculation range of the polynomial formula and tables, the perfect gas equation of state is used assuming a frozen state. The transformation of the governing equations (2D or Axisymmetric), the turbulence model to be used, and the method of calculating thermodynamic properties can be specified through user input.

The injection boundary condition can be used to simulate the working gas injection into the arc-heated wind tunnel. The isothermal wall (temperature of 1,000 K) condition for the arc heater wall and the isothermal (temperature of 300 K) wall condition for the other walls are basically set. When there is an experimental model in the test-section, an adiabatic or isothermal wall condition is given to the object, and a constant pressure outflow condition is used at the diffuser exit to simulate the pressure rise in the vacuum chamber. Wall boundary conditions, wall temperature, and mass flow rate of working gas can be set in the user input file.

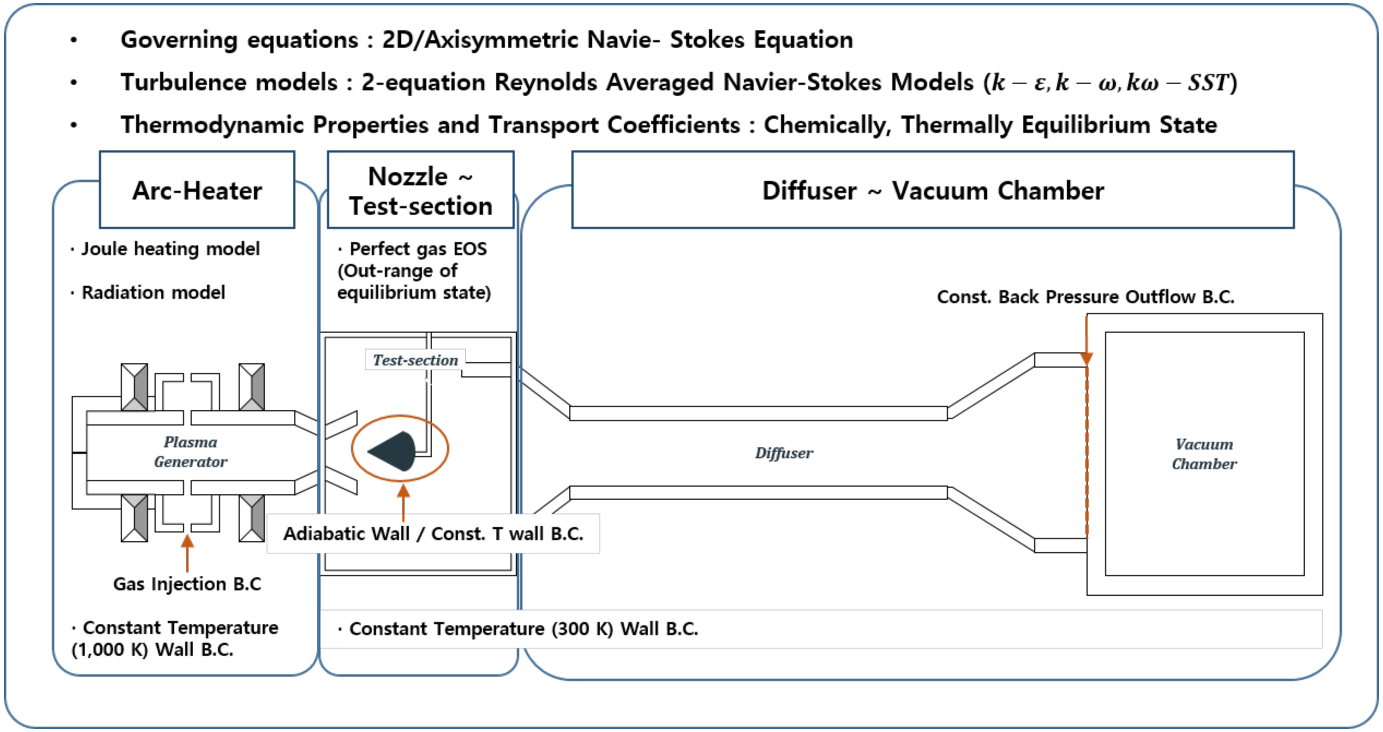

Figure 2.1: Physical models and boundary conditions of an arc-heated wind tunnel

2.1.2 Flow chart and numerical schemes

Figure 2.2 shows the flow chart of the numerical analysis code for an arc-heated wind tunnel. The numerical schemes and physical models used in each calculation step are organized.

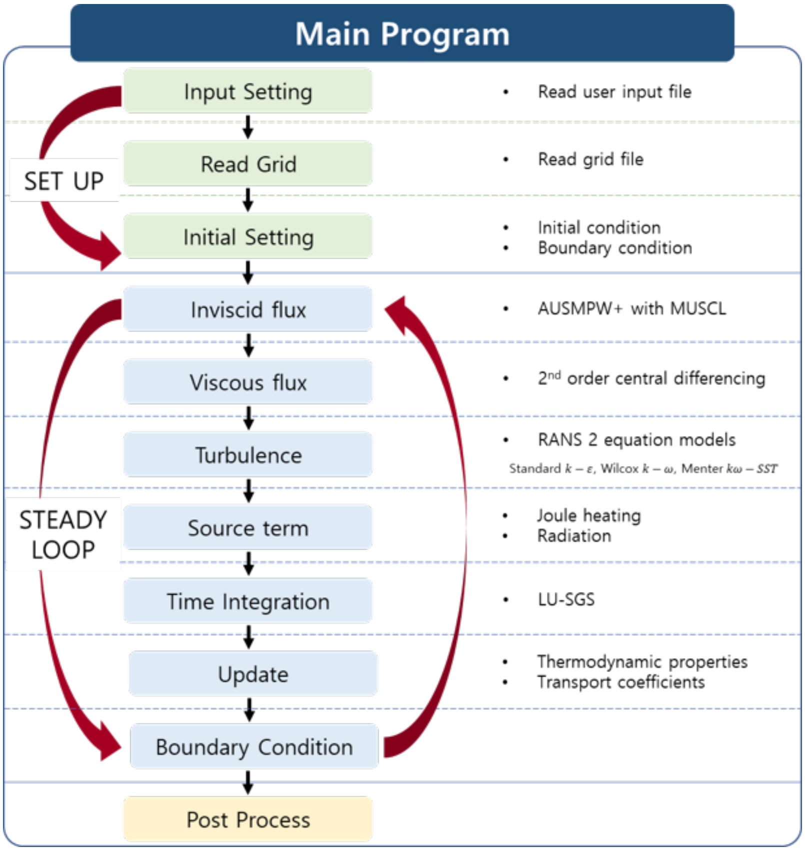

Figure 2.2: Flow chart of the analysis program

2.2 Physical Modeling

2.2.1 Governing equations

The time-dependent two-dimensional or axisymmetric Navier–Stokes equations are used as the governing equations. The continuity, momentum, and energy equations in vector form are expressed in Equation (2.1). In the governing equations, a continuity equation considering the density (ρ_2) and diffusion (D_2) of the second species is added to simulate the injection of shield gas or when the working gas is a mixture (e.g., Air and Argon). Variables such as density, velocity, and internal energy in the governing equation are the total value of the working gas, and the density of the main gas can be obtained by subtracting the density (ρ_2) of the second species from the total density. If the working gas is a single gas, the calculation is performed excluding the continuity equation of the second species. Also, the axisymmetric terms (H, H_v) and energy source due to Joule heat (jE) and radiation ($q_{R,x}, q_{R,y}$). The Joule heating and radiant heat flux source terms are calculated only inside the arc heater where high-temperature plasma exists, and are excluded from source terms when calculating nozzles, test-sections, diffusers, vacuum chambers, etc.

$$\frac{\partial \mathbf{Q}}{\partial t} + \frac{\partial \mathbf{E}}{\partial x} + \frac{\partial \mathbf{F}}{\partial y} = \frac{\partial \mathbf{E_v}}{\partial x} + \frac{\partial \mathbf{F_v}}{\partial y} + \alpha(\mathbf{H_v} - \mathbf{H}) + \mathbf{I} \tag{2.1}$$

Where,

$$\mathbf{Q} = \begin{bmatrix} \rho \\ \rho_2 \\ \rho u \\ \rho v \\ \rho e_t \end{bmatrix}, \mathbf{E} = \begin{bmatrix} \rho u \\ \rho u_2 \\ \rho u^2 + p \\ \rho u v \\ \rho h u \end{bmatrix}, \mathbf{F} = \begin{bmatrix} \rho v \\ \rho v_2 \\ \rho u v \\ \rho v^2 + p \\ \rho h v \end{bmatrix},$$

$$\mathbf{E_v} = \begin{bmatrix} 0 \\ \rho D_2 \dfrac{\partial c_2}{\partial x} \\ \boldsymbol{\tau}_{\mathbf{xx}} \\ \boldsymbol{\tau}_{\mathbf{xy}} \\ u\boldsymbol{\tau}_{\mathbf{xx}} + v\boldsymbol{\tau}_{\mathbf{xy}} - q_{c,x} - q_{R,x} \end{bmatrix}, \mathbf{F_v} = \begin{bmatrix} 0 \\ \rho D_2 \dfrac{\partial c_2}{\partial y} \\ \boldsymbol{\tau}_{\mathbf{xy}} \\ \boldsymbol{\tau}_{\mathbf{yy}} \\ u\boldsymbol{\tau}_{\mathbf{xy}} + v\boldsymbol{\tau}_{\mathbf{yy}} - q_{c,y} - q_{R,y} \end{bmatrix},$$

$$\mathbf{H_v} = \frac{1}{y} \begin{bmatrix} 0 \\ \rho D_2 \dfrac{\partial c_2}{\partial x} \\ (h_v)_2 \\ (h_v)_3 \\ (h_v)_4 \end{bmatrix}, \mathbf{H} = \frac{1}{y} \begin{bmatrix} \rho v \\ \rho v_2 \\ \rho uv \\ \rho v^2 + p \\ \rho hv \end{bmatrix}, \mathbf{I} = \begin{bmatrix} 0 \\ 0 \\ 0 \\ 0 \\ -jE \end{bmatrix}$$

$$\boldsymbol{\tau}_{\mathbf{ij}} = \mu \left(\frac{\partial u_i}{\partial x_j} + \frac{\partial u_j}{\partial x_i} \right) - \frac{2}{3}\mu(\nabla \cdot \vec{V})\delta_{i,j}, \quad i,j = x,y$$

$$\boldsymbol{\tau}_{\boldsymbol{\theta\theta}} = -\frac{2}{3}\mu \left(\frac{\partial u}{\partial x} + \frac{\partial v}{\partial y} \right) + \frac{3}{4}\mu \frac{v}{y}$$

$$(h_v)_2 = \boldsymbol{\tau}_{\mathbf{yx}} - \frac{2}{3}\frac{\partial}{\partial x}\left(\mu \frac{v}{y} \right)$$

$$(h_v)_3 = \boldsymbol{\tau}_{\mathbf{yy}} - \boldsymbol{\tau}_{\boldsymbol{\theta\theta}} - \frac{2}{3}\left(\mu \frac{v}{y} \right) - \frac{2}{3} y \frac{\partial}{\partial y} \left(\mu \frac{v}{y} \right)$$

$$(h_v)_4 = u\boldsymbol{\tau}_{\mathbf{yx}} + v\boldsymbol{\tau}_{\mathbf{yy}} + \frac{\mu}{Pr(\gamma-1)}\frac{\partial T}{\partial y} - \frac{2}{3}\left(\mu \frac{v^2}{y} \right) - \frac{2}{3} y \frac{\partial}{\partial y}\left(\mu \frac{v^2}{y} \right) - \frac{2}{3} y \frac{\partial}{\partial y}\left(\mu \frac{uv}{y} \right)$$

2.2.2 Thermodynamic properties and transport coefficients

When the air temperature exceeds 600 K, molecular vibration is observed and the specific heat ratio becomes a function of density and energy. Moreover, a chemical dissociation occurs as the air temperature exceeds 2,000 K. [20] Therefore, thermodynamic properties (e.g., pressure, temperature, and enthalpy) and transport coefficients (e.g., viscosity and Prandtl number) in the high-temperature region should be calculated while considering the specific heat ratio changes and chemical reaction. In an arc-heated wind tunnel, an arc-heater makes a high-enthalpy flow using arc-plasma that the total temperature is over 10,000 K. In addition, the static temperature of the flow could exceed 2,000 K when the flow meets the experimental model or wall inside the facility making a strong shock wave. Then, the specific heat ratio is no longer constant and chemical reactions should be considered.

In order to consider the specific heat ratio change and chemical reactions of working gas, thermal and chemical equilibrium are assumed. In the thermally and chemically equilibrium state, the characteristic time for chemical reactions (τ_c) is much shorter than the time for the flow characteristics to change (τ_f), and all chemical reactions occur before the flow changes. According to characteristic of hypersonic flow, arc-heated wind tunnel facilities $\tau_c/\tau_f \ll 1$; then, the inside flow can be assumed thermal and chemical equilibrium. However, Takahashi [21] proves non-equilibrium effect should be considered after the nozzle throat. Thus, thermally and chemically non-equilibrium states may be considered at the nozzle and test-section which are the supersonic/hypersonic flow region in the facility. However, in order to calculate non-equilibrium flow, the calculation must be performed by adding all species to the governing equation, resulting in a huge increase in the calculation time. Increasing calculation time makes it difficult to achieve the goal of this study to quickly grasp the initial design and operability of the wind tunnel, so thermal and chemical equilibrium are considered in the present study. Nevertheless, when performing numerical analysis for detailed design and ablation simulation, the non-equilibrium flow should be considered.

In the validation and verification section, numerical results of supersonic/hypersonic nozzle and experimental values are compared to make reference to the error range based on the equilibrium assumption.

According to Anderson [20], there are four methods to calculate thermodynamic properties and transport coefficients.

1. Directly calculate thermodynamic properties with equations obtained from statistical thermodynamics.

2. Using properties from a graphical plots such as the Mollier diagram.

3. Polynomial formulations using the relation among thermodynamic properties.

4. Interpolating tables of thermodynamic properties of high-temperature gases. The values of these tables are calculated based on statistical thermodynamics.

In the present study, the methods 3 and 4 are used.

A. Polynomial formula

To calculate thermodynamic properties using polynomial formula, the curve fitted data by Srinivasan et. al [23] is used, and for the transport coefficients calculation, the formula suggested by Gupta et al. [24] These curve fitting methods uses eleven species of the air ($O_2, N_2, O, N, NO, O^+, N^+, NO^+, O^{++}, N^{++}, e^-$) equilibrium table, and the temperature data range is up to 30,000 K, whereas the pressure data ranges from 10^-4 to 10^2 atm. The polynomial formulations for curve fitting data are defined as follows.

1. Pressure: $p = p(e, \rho) = \rho e(\tilde{\gamma} - 1)$

   The specific heat ratio ($\tilde{\gamma}$) is calculated as formulation bellows.

$$
\begin{aligned}
\tilde{\gamma} = a_1 + a_2Y + a_3Z + a_4YZ + a_5Y^2 + a_6Z^2 + a_7Y^2Z + a_8YZ^2 + a_9Y^3 \\
+a_{10}Z^3 + (a_{11} + a_{12}Y + a_{13}Z + a_{14}YZ + a_{15}Y^2 + a_{16}Z^2 + a_{17}Y^2Z \\
+a_{18}YZ^2 + a_{19}Y^3 + a_{20}Z^3)/[1 \pm exp(a_{21} + a_{22}Y + a_{23}Z + a_{24}YZ)]
\end{aligned}
\tag{2.2}
$$

   Where, $Y = \log_{10}(\rho/\rho_0)$ and $Z = \log_{10}(e/RT_0)$.

   The reference values (ρ_0,T_0) are those of the atmosphere air state.

2. Temperature: $T = T(\rho, p)$

$$
\begin{aligned}
\log_{10}(T/T_0) = d_1 + d_2Y + d_3Z + d_4YZ + d_5Y^2 + d_6Z^2 + d_7Y^2Z \\
+d_8YZ^2 + d_9Y^3 + d_{10}Z^3 + (d_{11} + d_{12}Y + d_{13}Z + d_{14}YZ \\
+d_{15}Y^2 + d_{16}Z^2 + d_{17}Y^2Z + d_{18}YZ^2 + d_{19}Y^3 + d_{20}Z^3) \\
/[1 \pm exp(d_{21} + d_{22}Y + d_{23}Z + d_{24}YZ)]
\end{aligned}
\tag{2.3}
$$

   Where, $Y = \log_{10}(\rho/\rho_0)$, $X = \log_{10}(p/p_0)$, and $Z = X - Y$.

3. Enthalpy: $h = h(\rho, p) = \frac{p}{\rho}(\frac{\tilde{\gamma}}{\tilde{\gamma}-1})$

   The general form of $\tilde{\gamma}$ is calculated as formulation bellows.

$$\begin{aligned}\tilde{\gamma} = c_1 + c_2Y + c_3Z + c_4YZ + c_5Y^2 + c_6Z^2 + c_7Y^2Z + c_8YZ^2 + c_9Y^3 \\ +c_{10}Z^3 + (c_{11} + c_{12}Y + c_{13}Z + c_{14}YZ + c_{15}Y^2 + c_{16}Z^2 + c_{17}Y^2Z \\ +c_{18}YZ^2 + c_{19}Y^3 + c_{20}Z^3)/[1 \pm exp(c_{21} + c_{22}Y + c_{23}Z + c_{24}YZ)]\end{aligned} \tag{2.4}$$

4. Viscosity(μ)

$$\mu = A_\mu + B_\mu\chi + C_\mu\chi^2 + D_\mu\chi^3 + E_\mu\chi^4 + F_\mu\chi^5, \chi = T/1000 \tag{2.5}$$

5. Thermal conductivity(κ)

$$\kappa = A_\kappa\chi^4 + B_\kappa\chi^3 + C_\kappa\chi^2 + D_\kappa\chi + E_\kappa, \chi = ln(T/1000) \tag{2.6}$$

6. Prandtl number(Pr)

$$Pr = A_{Pr} + B_{Pr}\chi + C_{Pr}\chi^2 + D_{Pr}\chi^3 + E_{Pr}\chi^4 + F_{Pr}\chi^5, \chi = T/1000 \tag{2.7}$$

B. Tables based on mixture model

The polynomial formula, introduced in the present study, is available only in the air; Therefore, when using a mixture as a working gas, use the mixture model used in [22] to create a table of thermodynamic properties and transport coefficients according to the composition ratio, and interpolate the values. Thermodynamic properties are tabulated based on the chemical equilibrium with the application by NASA [23], and transport coefficients are calculated using the approximation formula by Gupta et al. [24] and Yos et al. [25]. The detailed calculation procedure and theory are well explained by Lee [22] and Bae [26].

For example, as the working gas is a mixture of air and argon, the calculation procedure of thermodynamic properties and transport coefficients is as follows the procedure.

1. Create REPT, PTRE, diffusion, and mole tables depending on the concentration of mixture gas.

   Example of tables) Air only (Air 100 %+ Argon 0 %), Air 90 % + Argon 10 %, Air 80 % + Ar 20 %, . . . , Argon only (Air 0 %+ Ar 100 %)

2. Use the tables as input for the analysis program.

3. Calculate the concentration of the mixture using total flow density(ρ) and species density (ρ_2) during flow calculation.

4. Calculate thermodynamic properties and transport coefficients by bilinear interpolation of two mixture tables with corresponding concentrations.

C. Values under the limit of polynomial formula and tables

Polynomial formulas and tables are basically used for arc-heater analysis, so there is no problem in calculating high temperatures (maximum 30,000 K) and high pressures (maximum 100 atm). However, in the present study, the flow is supersonic/hypersonic and accelerates as it passes through the nozzle and the test- section, so there are cases where the calculation of low-temperature and low-pressure flow is necessary and beyond the calculation range. Therefore, in order to analyze the entire components of the arc-heated facility, a method of calculating reasonable values for thermodynamic properties and transport coefficients that are out of the calculation range is required. There are two methods for calculating the thermodynamic properties and transport coefficients of high Mach number flow outside the equilibrium calculation region: One is a calculation method of non-equilibrium flow, and the other is a calculation method of frozen flow. Non-equilibrium flow analysis is necessary for ablation simulation;

however, it is time inefficient in the initial design stage. In addition, according to references [27, 28], it can be seen that the frozen state results in the high Mach number and low-pressure region are closer to the experimental value than the equilibrium state, and the error due to the non-equilibrium effect is not large. Therefore, frozen flow is assumed in the present study.

When values of the equilibrium state are out of the calculable range, thermodynamic properties are calculated using the perfect gas equation of state, and transport coefficients use Sutherland's law [29]. This method may cause convergence problems due to discontinuous regions as shown in Figure 2.3a when calculations are performed again in the polynomial formula and table range.

To solve this, a smoothing function (Equation (2.8)) for an arbitrary physical quantity (ϕ) is used, as shown in Figure 2.3b.

$$\phi = \phi_1 + (\phi_2 - \phi_1)\frac{\phi_2 - \phi_{min}}{\phi_{max} - \phi_{min}} \tag{2.8}$$

Here, the range of values for smoothing is $\phi_{min} < \phi < \phi_{max}$, and each value is as follows.

When smoothing thermodynamic properties,

$$\begin{cases} \phi_1 : \text{Perfect gas state of equation values} \\ \phi_2 : \text{Polynomial formula or table values} \end{cases}$$

When smoothing transport coefficients,

$$\begin{cases} \phi_1 : \text{Values obtained from Sutherland law} \\ \phi_2 : \text{Polynomial formula or Table values} \end{cases}$$

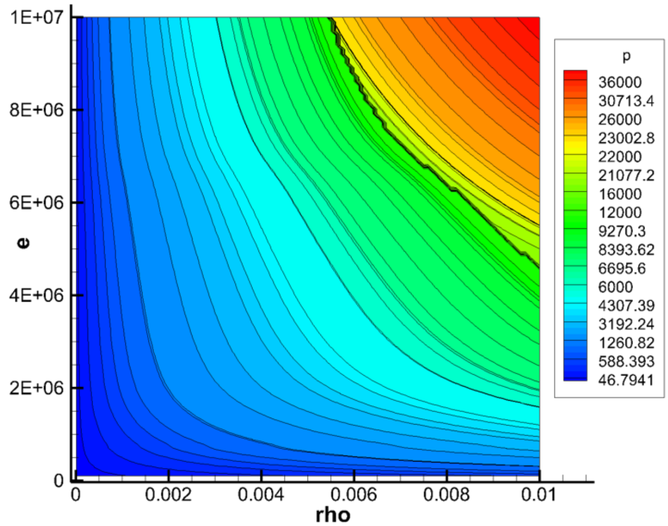

(a) Before smoothing

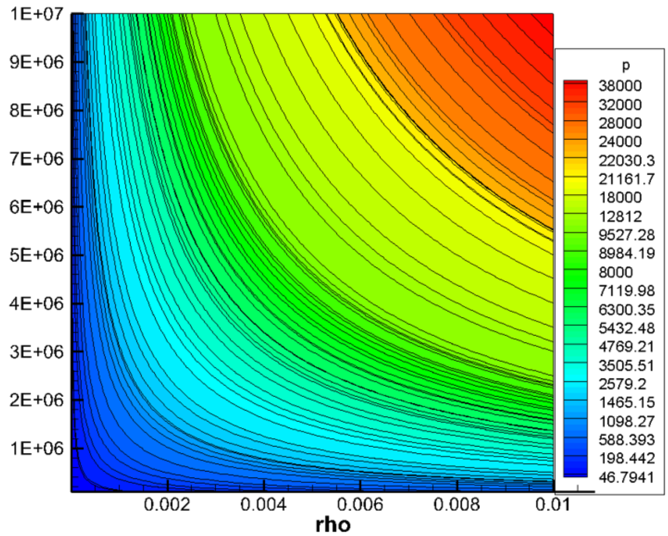

(b) After smoothing

Figure 2.3: Boundary and undervalue of polynomial formula and table

2.2.3 Joule heating models

Joule heating of arc plasma can be obtained by solving Maxwell's equations. Maxwell's equations consist of Gauss' Law, Gauss' Magnetism Law, Faraday's Law, and Ampere's Law, and they are defined as follows.

$$
\begin{aligned}
&\boldsymbol{\nabla} \cdot \mathbf{D} = q, && \textit{Gauss' Law} \\
&\boldsymbol{\nabla} \cdot \mathbf{B} = 0, && \textit{Gauss' Magnetism Law} \\
&\boldsymbol{\nabla} \cdot \times E = -\frac{\partial B}{\partial t}, && \textit{Faraday's Law} \\
&\boldsymbol{\nabla} \cdot \times H = \frac{\partial D}{\partial t} + J, && \textit{Ampere's Law}
\end{aligned}
\tag{2.9}
$$

Where,

$$
\begin{aligned}
&D = \epsilon E, && \textit{Constitutive equation} \\
&H = B/\mu_0, && \textit{Constitutive equation} \\
&J = \sigma E, && \textit{Ohm's Law} \\
&E = -V \boldsymbol{\nabla} \cdot \phi
\end{aligned}
\tag{2.10}
$$

In the present study, the following two models are used with appropriate assumptions for each type to calculate Joule heating of various types of arc-heaters.

A. Long cylindrical arc-plasma

Joule heating model for long cylindrical arc-plasma can be used for the analysis of a segmented heater and Huels heater that arc length can be assumed by coil location. If the current distribution is known, the Joule heating could be simply calculated by Ohm's Law. Since the constrictor of the segmented type heater is insulated, the current is constant along the axis. Then, assuming that the voltage gradient is independent of the radius and that the arc shape is a long cylindrical, Joule heating can be simplified.

Ohm's law for a cylindrical column is defined as Equation (2.11), and it can be rewritten in Equation (2.12).

$$j(x,y) = \sigma(x,y)E(x) \tag{2.11}$$

$$E(x) = \frac{j(x,y)}{\sigma(x,y)} = \frac{\int_0^R 2\pi y j(x,y)\,dy}{\int_0^R 2\pi y\sigma(x,y)\,dy} = \frac{I}{\int_0^R 2\pi y\sigma(x,y)\,dy} \tag{2.12}$$

Where,

$$I = \int_0^R \pi y j(x,y)\,dy = \textit{constant or} I(x) \tag{2.13}$$

In the Equation (2.13), the current (I) is input value, and it can be constant or a linear function of x [15]. An example of linear function of current distribution is shown in Figure 2.4.

Then, the joule heating ($S_{\textit{Joule heat}}$), which is source term of the energy equation, is given in Equation (2.14).

$$\begin{aligned} S_{\textit{Joule heat}} &= j(x,y)\cdot E(x) \\ &= \sigma(x,y)\cdot E(X)\cdot E(x) \\ &= \frac{\sigma(x,y)I^2}{[\int_0^R 2\pi y\sigma(x,y)\,dy]^2} \end{aligned} \tag{2.14}$$

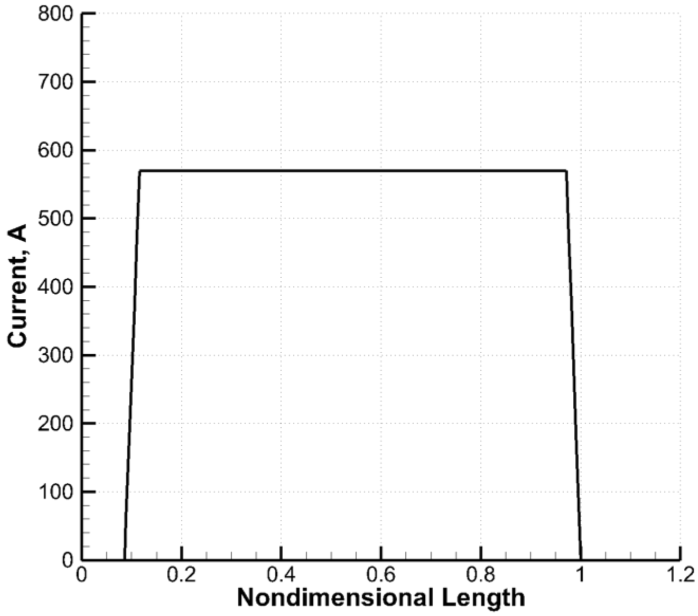

Figure 2.4: An example of current distribution along the axis

B. General arc-plasma

The Joule heating model for general arc plasma can be used in most arc-heaters except for inductively coupled plasma (ICP) heaters. Assuming the fluid inside heaters is electrically neutral, the electric current continuity equation from Maxwell's equation is expressed in Equation (2.15).

$$\frac{\partial(\boldsymbol{\nabla}\cdot D)}{\partial t} = -\boldsymbol{\nabla}\cdot J = \frac{\partial q}{\partial t} \tag{2.15}$$

$$\boldsymbol{\nabla}\cdot J = 0 \tag{2.16}$$

Using Ohm's law, Equation (2.16) is expressed as Equation (2.17), which is the electric potential equation.

$$\boldsymbol{\nabla}\cdot(\sigma\nabla\phi) = 0 \tag{2.17}$$

The electric potential equation for the axisymmetric form is as follows.

$$\frac{\partial}{\partial x}(\sigma\frac{\partial\phi}{\partial x}) + \frac{\partial}{\partial y}(\sigma\frac{\partial\phi}{\partial y}) + \frac{1}{y}(\frac{\partial\phi}{\partial y}) = 0 \tag{2.18}$$

By solving electric potential equation, arc-voltage and the electric field can be calculated as follow equations.

$$V = I/(-\int_0^R \sigma\nabla\phi 2\pi r\, dr) \tag{2.19}$$

$$E = -V\nabla\phi \tag{2.20}$$

Finally, the joule heating ($S_{Jouleheat}$) can be obtained directly.

$$S_{jouleheat} = j(x,y)\cdot E(x) = \sigma(x,y)\cdot E(x)\cdot E(x) \tag{2.21}$$

To solve the electric potential equation numerically, the discretized form of the axisymmetric electric potential equation and numerical method are explained by Park [30] (See chapter 2.3 Electric filed modeling).

2.2.4 Radiation model

Inside arc-heaters, the flow temperature is high enough to occur radiation; therefore, Pegot et al. [31] adopted radiation to numerical calculation. In the present study, the radiation model of Sakai et al. [32] is used, with five assumptions.

Assumptions:

- Scattering of photons by molecules is negligible.
- Heater wall is a black body with a constant temperature.
- Cylinder length is infinite to a simple calculation of radiant heat flux in cylindrical coordinates.
- Temperature gradients in the radial direction are larger than those in the axial direction.
- Exponential kernel approximation is used to simple integration of the radiant flux.

A. Cylindrical radiative transport model

The radiative heat flux equation is defined as Equation (2.22).

$$-\frac{1}{\rho\kappa_\nu}\frac{dI_\nu}{ds} = I_\nu - B_\nu \tag{2.22}$$

Here, I_ν is the radiative intensity traveling along the ray (s). κ_ν is the absorption coefficient, and B_ν represents black body function.

When the radiative intensity at a point is calculated for all directions, the radiant flux per unit frequency in cylindrical coordinates can be calculated as follows.

$$q_\nu(r) = \int_\Omega I_\nu(r) cos\Theta \, d\Omega \tag{2.23}$$

The cylindrical geometry and coordinate system are shown in Figure 2.5.

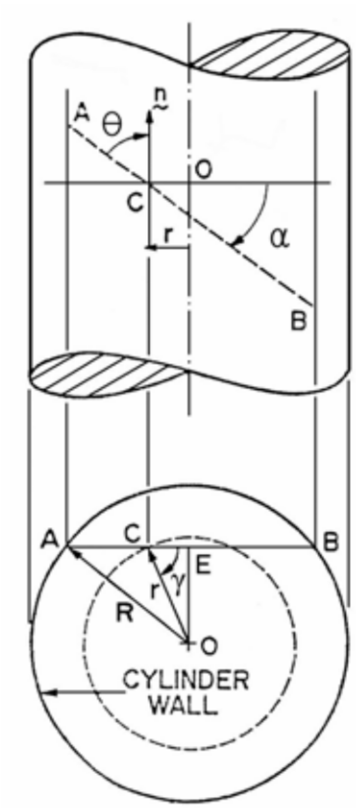

Figure 2.5: Cylindrical coordinate system for the radiation model

In the Figure 2.5 and Equation (2.23), Θ is the angle between the ray and normal direction of outward to the surface, and Ω is the solid angle.

Integrate Equation (2.22) and substitute it to Equation (2.23); then, the radiant heat flux can be expressed as follows.

$$
\begin{aligned}
q_\nu(r) =& 4\int_0^{\pi/2} cos\gamma[B_\nu(R)D_3(\int_0^{(R^2-r^2sin^2\gamma)^{\frac{1}{2}}} \mu(y)\,dy + \int_0^{(rcos\gamma)} \mu(y)\,dy) \\
&+ \int_0^{(R^2-r^2sin^2\gamma)^{\frac{1}{2}}} B_\nu(y)\mu(y)D_2(\int_0^{y} \mu(y')\,dy' + \int_0^{rcos\gamma} \mu(y)\,dy)\,dy \\
&+ \int_0^{rcos\gamma} B_\nu(y)\mu(y)D_2(\int_0^{rcos\gamma} \mu(y')\,d(y'))\,dy]\,d\gamma \\
&- 4\int_0^{\pi/2} cos\gamma[B_\nu(R)D_3(\int_{rcos\gamma}^{(R^2-r^2cos^2\gamma)^{\frac{1}{2}}} \mu(y)\,dy) \\
&+ \int_{rcos\gamma}^{(R^2-r^2sin^2\gamma)^{\frac{1}{2}}} B_\nu(y)\mu(y)D_2(\int_{rcos\gamma}^{y} \mu(y')\,dy')\,dy]\,d\gamma
\end{aligned}
\tag{2.24}
$$

Where y, y', and $D_n(x)$ are defined as follows.

$$
\begin{aligned}
y &= (r'^2 - r^2sin^2\gamma)^{1/2} \\
y' &= (r''^2 - r^2sin^2\gamma)^{1/2} \\
D_n(X) &= \int_0^1 \frac{z^{n-1}}{\sqrt{1-z^2}} exp(-\frac{x}{z})\,dz
\end{aligned}
$$

Here, the $D_n(x)$ is a function of exponential integral function using kernel approximation, and for the present study, for n equals three.

The local radiant heat flux is the sum of the radiant flux directed away from the location r (i.e.,$q_\nu^+(r)$) and that of directed toward the location r (i.e., $q_\nu^-(r)$).

$$q_\nu(r) = q_\nu^+(r) + q_\nu^-(r) \tag{2.25}$$

Using the angular directional fluxes (i.e., $G^{\pm}(r,\gamma)$), the equation (2.25) is expressed and discretized as Equations (2.26) and (2.27), and detailed calculation method of it is well explained by Lee [22]. (See chapter 2.4 Radiation modeling)

$$q_{\nu}^{\pm}(r) = \int_{0}^{\pi/2} cos\gamma G^{\pm}(r,\gamma)\, d\gamma \tag{2.26}$$

$$q_{\nu}^{\pm}(r_i) = \sum_{j=2}^{j=N} (\frac{G_{i,j}^{\pm} + G_{i,j-1}^{\pm}}{2})(sin\gamma_{i,j} - sin\gamma_{i,j-1}) \tag{2.27}$$

Finally, total radiative heat flux with radius, r, can be calculated by integral Equation (2.28) overall frequency.

$$q_R(r) = \int_{0}^{\infty} q_{\nu}(r)\, d\nu \tag{2.28}$$

When the band-averaged model is used, the total radiative flux can be expressed as follows.

$$q_R(r) = \sum_{l=1}^{m} q_l(r) \tag{2.29}$$

B. Three-band model

The absorption coefficient (κ_ν) of the radial transfer equation is a coefficient representing the degree of energy absorption, and it is a function of pressure, temperature, and frequency. For accurate radiation heat transfer calculation, it is necessary to calculate the absorption coefficient for each frequency (line-by-line calculation), but it is essential to use a band-averaging model for efficient calculation time. Using the band averaging model, the absorption coefficient becomes a function of temperature and pressure. In the present study, based on the Planck, Rosseland, and Gray-gas (PRG) model [34], the three-band model developed by Sakai et al. [32], which has an accuracy similar to the line-by-line calculation method for arc-heater analysis is used.

The absorption coefficient of the three-band model is divided into the following three areas.

1) $\kappa_\lambda > acm^{-1}$ and $\lambda < 2000\mathring{A}$

2) $\kappa_\lambda < acm^{-1}$ and $\lambda < 2000\mathring{A}$

3) $\kappa_\lambda > 2000\mathring{A}$

Here, a is a user defined value, and a is set to 5 cm^{-1} in the present study.

The averaged absorption coefficients are determined by the escape factor (ϕ). The factor is defined as Equation (2.30), and it represents the probability that an emitted photon traveling distance (d) without absorption.

$$\phi = \frac{\int_0^\infty E_\lambda exp(-\kappa_\lambda d)\, d\lambda}{\int_0^\infty E_\lambda\, d\lambda} \tag{2.30}$$

Where E_λ is an emission coefficient, and κ_λ is the absorption coefficient at a wavelength λ. Assuming the averaged absorption coefficients exist over a certain rage, the absorption as follows.

$$\kappa = \frac{-\,log(\phi)}{d} \tag{2.31}$$

The total specific radiant intensity (I) is calculated using Equation (2.32) to obtain the mean wavelength black body function (Planck function).

$$I = \int_0^{\infty} I_\lambda \, d\lambda = \int_0^{\infty} B_\lambda (1 - exp(-\kappa_\lambda)) \, d\lambda \tag{2.32}$$

Where B_λ is black body function at a wave length λ.

With the gray-gas approximation, the radiant intensity is rewritten as Equation (2.33).

$$I = B[1 - exp(-\kappa d)] \tag{2.33}$$

Finally, using κ, d, and I above equations, the averaged wave length black body function (B) is obtained as follows.

$$B = \frac{1}{1 - exp(\kappa d)} \tag{2.34}$$

In the present study, the following set is used for the traveling distance d according to the temperature of the flow.

$$\begin{cases} d_1 = d_2 = 2cm \text{ for } T > 10,000K \\ d_1 = d_2 = 3cm \text{ for } T < 10,000K \\ d_3 = 20cm \end{cases}$$

2.2.5 Turbulence models

The standard $k-\varepsilon$ [33], $k-\omega$ model of Wilcox [34], and Menter's $k\omega$-SST [35] are adopted to the analysis code as turbulence models. These three models are Reynolds Averaged Navier-Stokes (RANS) two-equation models, and they are the popular models solving transport equations for turbulence kinetic energy. The Reynolds stress (τ_{ij}) of all the models is modeled in terms of the eddy viscosity (μ_t), and it is expressed in Equation (2.35).

$$\tau_{t,ij} = 2\mu_t(S_{ij} - S_{nn}\delta_{ij}/3) - 2\rho k\delta_{ij}/3 \tag{2.35}$$

A. $k-\varepsilon$ Model

The two turbulence transport equations of the $k-\varepsilon$ model by Jones and Launder are defined in Equations (2.36) and (2.37). The first equation represents the turbulence energy(k) transport equation, and the second one represents energy dissipation (ε) transport equation.

$$\frac{\partial \rho k}{\partial t} + \frac{\partial}{\partial x_j}(\rho u_j \frac{\partial k}{\partial x_j} - (\mu + \frac{\mu_\tau}{\sigma_k})\frac{\partial k}{\partial x_j}) = \tau_{t,ij}s_{ij} - \rho\varepsilon \tag{2.36}$$

$$\frac{\partial \rho\varepsilon}{\partial t} + \frac{\partial}{\partial x_j}(\rho u_j\varepsilon - (\mu + \frac{\mu_\tau}{\sigma_\varepsilon})\frac{\partial \varepsilon}{\partial x_j}) = c_{\varepsilon 1}\frac{\varepsilon}{k}\tau_{t,ij}s_{ij} - c_{\varepsilon 2}\rho\frac{\varepsilon^2}{k} \tag{2.37}$$

Here, the constants of the model are defined as follows,

$$c_\mu = 0.09, c_{\varepsilon 1} = 1.45, c_{\varepsilon 1} = 1.92,$$
$$\sigma_k = 1.0, \sigma_\varepsilon = 1.3, Pr_t = 0.9$$

The eddy viscosity (μ_t) is defined as a function of the turbulent kinetic energy, and the turbulent dissipation rate as below.

$$\mu_t = c_\mu f_\mu \rho k^2/\varepsilon \tag{2.38}$$

This turbulence model is known to give reasonable results for free-shear layer flows with small pressure gradients. Therefore, the model has good agreement with experimental results for small mean pressure gradients. However, the model requires a fine grid spacing near solid walls and explicit wall-damping functions.

B. $k-\omega$ **Model**

The two turbulence transport equations of the Wilcox $k-\omega$ model are defined in Equations (2.39) and (2.40). The first equation represents the turbulence energy(k) transport equation, and the second one represents the specific dissipation rate (ω) equation.

$$\frac{\partial \rho k}{\partial t}+\frac{\partial}{\partial x_j}(\rho u_j k-(\mu+\sigma^*\mu_\tau)\frac{\partial k}{\partial x_j})=\tau_{t,ij}s_{ij}-\beta^*\rho\omega k \tag{2.39}$$

$$\frac{\partial \rho k}{\partial t}+\frac{\partial}{\partial x_j}(\rho u_j \omega-(\mu+\sigma\mu_\tau)\frac{\partial \omega}{\partial x_j})=\alpha\frac{\omega}{k}\tau_{t,ij}s_{ij}-\beta\rho\omega^2 \tag{2.40}$$

Here, the constants of the Wilcox model are defined as follows.

$$\alpha=\frac{5}{9},\beta=\frac{3}{40},\beta^*=\frac{9}{100},$$
$$\sigma=0.5,\sigma^*=0.5,Pr_t=0.9$$

The eddy viscosity (μ_t) of the Wilcox model is defined as a function of the turbulent kinetic energy, and the specific dissipation rate is as follows.

$$\mu_t=\rho k/\omega \tag{2.41}$$

The $k-\omega$ model of Wilcox does not require wall damping functions as does the $k-\varepsilon$ model due to the large values of the specific dissipation rate (ω) near the wall region. This turbulence model has advantages in numerical stability, and it gives a good agreement with experimental results in the logarithmic region for mild adverse pressure gradients. However, in free-shear layer and adverse pressure gradient boundary layer flows, the results of the model are sensitive to the specific dissipation rate of the free stream.

C. $k\omega - SST$ Model

The biggest feature of Menter's $k\omega - SST$ (shear stress transport) model is that the Wilcox $k - \omega$ model is used in the near wall region, and the standard $k - \epsilon$ model is used in the boundary layer edge and free shear layer region by using the blending function. (Figure 2.6)

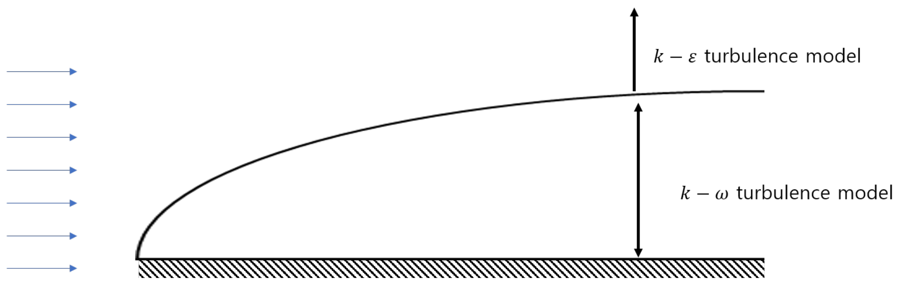

Figure 2.6: Schematic of the $k\omega - SST$ model

The transport equation for the turbulent kinetic energy (k) is defined in Equation (2.42), and the specific dissipation (ω) equation is written in Equation (2.43).

$$\frac{\partial \rho k}{\partial t} + \frac{\partial}{\partial x_j}(\rho u_j k - (\mu + \sigma_k \mu_T)\frac{\partial k}{\partial x_j}) = \tau_{t,ij} s_{ij} - \beta^* \rho \omega k \tag{2.42}$$

$$\frac{\partial \rho \omega}{\partial t} + \frac{\partial}{\partial x_j}(\rho u_j \omega - (\mu + \sigma \mu_T)\frac{\partial \omega}{\partial x_j}) = P_\omega - \beta \rho \omega^2 + 2(1 - F_1)\frac{\rho \sigma_{\omega 2}}{\omega}\frac{\partial k \partial \omega}{\partial x_j \partial x_j} \tag{2.43}$$

Where the production term (P_ω) of the specific dissipation is as follows.

$$P_\omega \equiv 2\gamma\rho(2s_{ij} - \omega s_{nn}\delta_{ij}/3)s_{ij} \tag{2.44}$$

The auxiliary blending function (F_1) is defined in Equation (2.45).

$$F_1 = \tanh\left\{\min\left[\max[\frac{\sqrt{k}}{0.09\omega y}, \frac{500\mu}{\rho\omega y^2}], \frac{4\rho\sigma_{\omega 2}k}{CD_{k\omega}y^2}\right]^4\right\} \tag{2.45}$$

In the blending function, $CD_{k\omega}$ stands for cross-diffusion in the k-ω model, and it is expressed as follows.

$$CD_{k\omega} = \max\left[2\rho\sigma_{\omega 2}\frac{1}{\omega}\frac{\partial k}{\partial x_j}\frac{\partial \omega}{\partial x_j}, 10^{-20}\right] \tag{2.46}$$

The function F_1 is designed to take the values one on the wall surfaced, and it goes to zero at the boundary layer edge. The constants of the model are as follows.

$$\alpha_1 = 0.31, \beta^* = 0.09, \kappa = 0.41$$

Also, the coefficients β, γ, σ_k,and σ_ω can be noted with the symbol ϕ as Equation (2.47), defined by blending the coefficients of the ϕ_1 (coefficients of the $k - \omega$ model) with those of the ϕ_2 (coefficients of the $k - \varepsilon$ model).

$$\phi = F_1\phi_1 + (1 - F_1)\phi_2 \tag{2.47}$$

And the coefficients of the original models are as follows.

$$\sigma_{k1} = 0.85, \sigma_{\omega 1} = 0.5, \beta_1 = 0.075,$$
$$\gamma_1 = \beta_1/\beta^* - \sigma_{\omega 1}\kappa^2/\sqrt{\beta^*} = 0.553$$
$$\sigma_{k2} = 1.0, \sigma_{\omega 2} = 0.856, \beta_2 = 0.0828,$$
$$\gamma_2 = \beta_2/\beta^* - \sigma_{\omega 2}\kappa^2/\sqrt{\beta^*} = 0.440$$

Then, the eddy viscosity (μ_t) of the $k\omega - SST$ model is defined as follows.

$$\mu_t = \frac{\rho k/\omega}{max[1, \Omega F_2/a_1\omega]} \tag{2.48}$$

Here, the F_2 is another auxiliary function of the model to modify the eddy viscosity in the boundary region improving the prediction of separated flows. In this model, the function, F_2, is defined using wall distance (y) as follows.

$$F_2 = \tanh\left\{(\max\left[2\frac{\sqrt{k}}{0.09\omega y}, \frac{500\mu}{\rho\omega y^2}\right])^2\right\} \tag{2.49}$$

2.3 Numerical Methods

2.3.1 Flux schemes

A. AUSMPW+

An improved version of the advection upstream splitting method by pressure-based weight functions (AUSMPW+) [36] is used as a numerical scheme to calculate the vectors E and F, which are the Euler terms of the governing equation.

The AUSMPW+ method is a numerical method of the AUSM family [37] and was developed to remove oscillations on the wall that occurred after a strong shock wave or near the wall in the AUSM+ scheme [38]. The AUSMPW+ scheme shows high accuracy and robustness in the analysis of chemically reactive flows and supersonic/hypersonic flows.

The flux of the cell interface (i.e., subscripts 1/2) using the AUSMPW+ scheme is equal to Equation (2.50).

$$F_{\frac{1}{2}} = \overline{M}_L^+ c_{\frac{1}{2}} \phi_L + \overline{M}_R^- c_{\frac{1}{2}} \phi_R + (P_L^+ P_L + P_R^- P_R) \tag{2.50}$$

Where, $\phi = (\rho, \rho u, \rho H)^T$, $P = (0, p, 0)^T$, and subscripts L and R indicate the left and right status of the cell interface as shown in Figure 2.7.

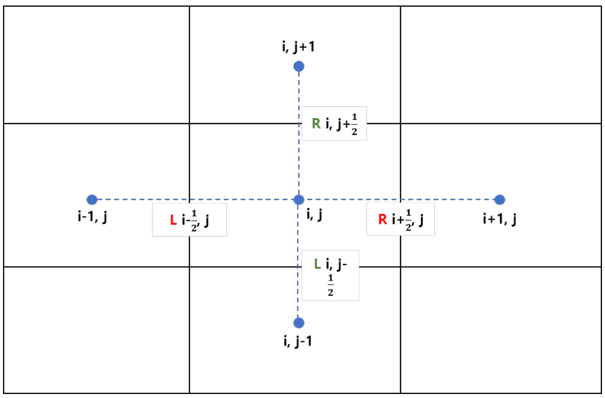

Figure 2.7: Left(L) and right(R) values at a computation cell interface

Mach number is defined as follows.

$$m_{\frac{1}{2}} = M_L^+ + M_R^- \tag{2.51}$$

Where, $\overline{M}_L^+$ and $\overline{M}_R^-$ are as follows.

i) $m_{\frac{1}{2}} = M_L^+ + M_R^- \geq 0$, then

$$\overline{M}_L^+ = M_L^+ + M_R^-[(1-w)(1+f_R) - f_L] \tag{2.52}$$

$$\overline{M}_R^- = w(1+f_R) \tag{2.53}$$

ii) $m_{\frac{1}{2}} = M_L^+ + M_R^- < 0$, then

$$\overline{M}_L^+ = M_L^+ + w(1+f_L) \tag{2.54}$$

$$\overline{M}_R^- = M_R^- + M_L^+[(1-w)(1+f_L) - f_R] \tag{2.55}$$

The w in Equations (2.52)   (2.55) is defined as Equation (2.56).

$$w(P_L, P_R) = 1 - min(\frac{P_L}{P_R}, \frac{P_R}{P_L})^3 \tag{2.56}$$

And the pressure weighted function f_L and f_R are as follows.

$$f_{L,R} = (\frac{P_{L,R}}{P_s} - 1), P_s \neq 0 \tag{2.57}$$

Where,

$$P_s = P_L^+ P_L + P_R^- P_R \tag{2.58}$$

$M^{\pm}$ and $P^{\pm}$ according to the Mach number are defined as follows.

$$M^{\pm} = \begin{cases} \pm\frac{1}{4}(M \pm 1)^2, & |M| \leq 1 \\ \frac{1}{2}(M \pm |M|), & |M| > 1 \end{cases} \tag{2.59}$$

$$P^{\pm} = \begin{cases} \pm\frac{1}{4}(M \pm 1)^2(2 \mp M), & |M| \leq 1 \\ \frac{1}{2}(M \pm sign(M)), & |M| > 1 \end{cases} \tag{2.60}$$

The Mach numbers in the L and R directions are defined as in Equation (2.61).

$$M_{L,R} = \frac{U_{L,R}}{c_{1/2}} \tag{2.61}$$

Here, the speed of sound ($c_{1/2}$) at the midpoint is as follows.

$$c_{1/2} = \begin{cases} \min\left[\frac{c^{*2}}{\max(|U_L|, c^*)}\right], & \frac{1}{2}(U_L + U_R) > 0 \\ \min\left[\frac{c^{*2}}{\max(|U_R|, c^*)}\right], & \frac{1}{2}(U_L + U_R) < 0 \end{cases} \tag{2.62}$$

Where,

$$c^* = \sqrt{2(\gamma - 1)/(\gamma + 1)H_{normal}} \tag{2.63}$$

$$H_{normal} = \frac{1}{2}(H_L - \frac{1}{2}V_L^2 + H_R - \frac{1}{2}V_R^2) \tag{2.64}$$

B. MUSCL

In the flux equation (Equation (2.50)), $\phi_{(L,R)}$ is the point values at the cell interface between i and i+1 cell. If spatial scheme uses $\phi_L = \phi_i$ and $\phi_R = \phi_{(i+1)}$, it has first-order accuracy in space. In the present study, the monotonic upstream-centered scheme for conservation laws (MUSCL) [39] is used to improve spatial accuracy. The accuracy is improved by linear reconstruction using slope limiters [40, 41]. The basic form of spatial reconstruction with limiters is as follows,

$$\phi_L = \phi_i + 0.5 \times \varphi_L \times (\phi_{i+1} - \phi_i) \tag{2.65}$$

$$\phi_R = \phi_{i+1} + 0.5 \times \varphi_R \times (\phi_i - \phi_{i+1}) \tag{2.66}$$

where, φ is a slope limiter.

The slope limiters used in the present study are the Minmod, Van Leer, and Superbee limiters.

Minmod Limiter :

$$\varphi(r) = \max[0, \min(1, r)] \tag{2.67}$$

Van Leer Limiter :

$$\varphi(r) = \frac{r + |r|}{1 + |r|} \tag{2.68}$$

Superbee Limiter :

$$\varphi(r) = \max[0, \min(2r, 1), \min(r, 2)] \tag{2.69}$$

C. Central diferencing method

The viscous term (vector E_v and F_v) of the governing equation is discretized using the second-order central differencing method

2.3.2 Time integration schemes

A. LU-SGS

The Lower-Upper Symmetric Gauss-Seidel (LU-SGS) method by Yoon et al. [42] is used as a time integration method. The method is an implicit time integration scheme based on a lower-upper factorization and Gauss-Seidel relaxation. Also, it requires only the scalar calculation for inversion, reducing computation memory and time.

In the governing equations, the time differential equation with spatial flux discretizing separately can be written as follows.

$$\frac{1}{J}\frac{dQ}{dt} + R = 0 \tag{2.70}$$

Then, the left-hand side of the equation can be a combination of matrices by the LU-SGS method as follows.

$$(LD^{-1}U)\triangle Q^n_{i,j} = -R^n_{i,j} \tag{2.71}$$

Where,

$$\begin{aligned} L &= \frac{1}{J\triangle t} + D^-_\xi A^+ + D^-_\eta B^+ - A^- - B^- \\ D &= \frac{1}{J\triangle t} + A^+ - A^- + B^+ - B^- \\ U &= \frac{1}{J\triangle t} + D^+_\xi A^- + D^+_\eta B^- - A^+ - B^+ \end{aligned} \tag{2.72}$$

The flux Jacobian Matrices (A, B) can be split to yield diagonal dominance as Equations (2.73) and (2.74).

$$A^\pm = \frac{1}{2}[A \pm \rho(\overline{A})I] = \frac{1}{2}[A \pm k \max\left|\frac{\lambda_i(A)}{J}\right| I] \tag{2.73}$$

$$B^\pm = \frac{1}{2}[A \pm \rho(\overline{B})I] = \frac{1}{2}[A \pm k \max\left|\frac{\lambda_i(B)}{J}\right| I] \tag{2.74}$$

with, $1.01 \leq k \leq 1.05$.

The Equations (2.73) and (2.74) are the approximate Jacobian matrix and using it, the term inside Equation (2.71) can be simplified as follows.

$$\frac{1}{J\triangle t} + (A^{+} - A^{-})_{ij} + (B^{+} - B^{-})_{ij} = [\frac{1}{J\triangle t} + \rho(\overline{A}) + \rho(\overline{B})]I \qquad (2.75)$$

Then, the final form of LU-SGS (Equation (2.75)) is expressed in Equation (2.76) and Equation (2.77).

$$\begin{aligned} &[\frac{1}{J\triangle t} + \rho(\overline{A}) + \rho(\overline{B})]\triangle\overline{Q^{*}}_{ij} \\ &\cong -R_{ij} + A^{*}_{i-1,j}\triangle Q_{i-1,j} + B^{+}_{i,j-1}\triangle Q_{i,j-1} \\ &= LS_{ij} \end{aligned} \qquad (2.76)$$

$$\begin{aligned} &[\frac{1}{J\triangle t} + \rho(\overline{A}) + \rho(\overline{B})]\triangle Q_{i,j} \\ &\cong -LS_{ij}D + A^{-}_{i+1,j}\triangle Q_{i+1,j} + B^{-}_{i,j+1}\triangle Q_{i,j+1} \end{aligned} \qquad (2.77)$$

B. Dual time stepping (DTS)

In order to analyze the initial shock wave moving over time, the flow inside the test-section and the pressure change in the vacuum chamber, unsteady flow analysis is required. For unsteady flow analysis, a dual-time stepping method, that can improve time accuracy by performing repeated calculations for each physical time step using pseudo-time stepping, is used. In the present study, a dual-time stepping method with second-order accuracy for time is used. In the governing equation, the flux vectors E, F, E_V, F_V, H, H_V, and S are expressed as residual (R), and the derivative of time is differentiated by the second-order backward implicit formula and then moved to the right side as follows.

$$0 = -\frac{1.5Q^{n+1} - 2Q^n + 0.5Q^{n-1}}{J\triangle t} - \hat{R}^{n+1} \tag{2.78}$$

Using pseudo time (τ), add the derivative of Q to the left side of Equation (2.78).

$$\frac{1}{J}\frac{\partial Q^{n+1}}{\partial \tau} = -\frac{1.5Q^{n+1} - 2Q^n + 0.5Q^{n-1}}{J\triangle t} - \hat{R}^{n+1} = -\hat{S}^{n+1} - \hat{R}^{n+1} \tag{2.79}$$

Differentiate the time derivative for the pseudo time with the first-order Euler implicit formula.

$$\frac{1}{J}\frac{Q^{n+1,m+1} - Q^{n+1,m}}{\triangle \tau} = -\hat{R}^{n+1,m+1} - \hat{S}^{n+1,m+1} \tag{2.80}$$

Where subscript m is iteration in Pseudo time. Then, the final formula of the dual time stepping method is written in Equation (2.81).

$$\left[\frac{1}{J\triangle\tau} + \left\{\frac{\partial \hat{R}}{\partial Q} + \frac{\partial \hat{S}}{\partial Q}\right\}^{n+1,m}\right] \triangle Q^{n+1,m} = -\hat{R}^{n+1,m} - \hat{S}^{n+1,m} \tag{2.81}$$

C. Local time stepping

A representative method for time-efficiently obtaining a steady-state solution is local time stepping. It updates each cell using individual time steps to accelerate convergence time. The time step for steady solution (or Psuedo time step in DTS) in the governing equation is based only on the convection and diffusion time step, and it is formed by the spectral radius of the flux Jacobians of the linearized Navier-stokes equations.

$$\frac{1}{J}\frac{\partial Q}{\partial t} + A\frac{\partial Q}{\partial \xi} + B\frac{\partial Q}{\partial \eta} = C\frac{\partial^2 Q}{\partial \xi^2} + D\frac{\partial^2 Q}{\partial \eta^2} + E\frac{\partial^2 Q}{\partial \xi \partial \eta} \tag{2.82}$$

In the linearized Navier-stokes equation (Equation (2.82)), A and B are the inviscid (Euler) flux Jacobians, and C, D, and E are the viscous flux Jacobian. Then, the individual time step(Δt) is calculated as the Equation (2.83).

$$\frac{1}{\triangle t} = \frac{1}{\triangle t_{\text{convective}}} + \frac{1}{\triangle t_{\text{diffusion}}} \tag{2.83}$$

Where,

$$\triangle t_{\text{convective}} = \frac{CFL}{\rho(A) + \rho(B)} \tag{2.84}$$

$$\triangle t_{\text{diffusion}} = \frac{1}{4}\frac{CFL}{\rho(C) + \rho(D) + \rho(E)} \tag{2.85}$$

Here, CFL is the Courant number, and each term is defined as follows.

$$\rho(A) = \lambda_\xi = |u\xi_x + v\xi_y| + c\sqrt{\xi_x^2 + \xi_y^2} \tag{2.86}$$

$$\rho(B) = \lambda_\eta = |v\eta_x + u\eta_y| + c\sqrt{\eta_x^2 + \eta_y^2} \tag{2.87}$$

$$\rho(C) = (\lambda_d)_\xi = \frac{1}{Re_c}\frac{\gamma\mu}{\rho Pr}(\xi_x^2 + \xi_y^2) \tag{2.88}$$

$$\rho(D) = (\lambda_d)_\eta = \frac{1}{Re_c}\frac{\gamma\mu}{\rho Pr}(\eta_x^2 + \eta_y^2) \tag{2.89}$$

$$\rho(E) = (\lambda_d)_{\xi\eta} = \frac{1}{Re_c}\frac{1}{\rho}\left[(\lambda + 3\mu)(\xi_x\eta_x + \xi_y\eta_y) + (\lambda + \mu)\sqrt{(\xi_x^2 + \xi_y^2)(\eta_x^2 + \eta_y^2)}\right] \tag{2.90}$$

2.4 Boundary Conditions

2.4.1 Wall boundary conditions

Constant temperature wall boundary condition and adiabatic wall boundary condition are used to analyze various arc-heated wind tunnels. Both boundary conditions are no-slip conditions, and the wall pressure is calculated as equal to the pressure inside the boundary layer.

A. Constant temperature wall

Inside an arc-heated wind tunnel, the flow temperature is very high, and since the temperature rise rate by the shock wave is also large, various cooling methods are used to protect the wall from ablation. In numerical analysis, constant wall temperature is used as one of the wall boundary conditions to simulate it.

The wall temperature of the arc heater is set to 1,000 K considering the melting point of the material, and the wall temperature of other components such as the nozzle, test-section, and diffuser is set to 300 K. When the heater and the nozzle are analyzed together, numerical instability occurs because the wall temperature rapidly decreases from 1,000 K to 300 K. Therefore, for numerical stability, the wall temperature at position x between the heater and the nozzle is given by Equation (2.91). Using the equation, the wall temperature is calculated from 1,000 K to 300 K depending on the distance.

$$T_{wall}(x) = T_{\text{heater wall}} - \frac{T_{\text{heater wall}} - T_{\text{nozzle wall}}}{x_{\text{heater}} - x_{\text{nozzle}}}(x - x_{\text{heater}}) \tag{2.91}$$

B. Adiabatic wall

In the case of a device without a cooling effect such as an experimental model, the adiabatic wall boundary condition is used. The adiabatic wall boundary condition is satisfying Equation (2.92) conditions, which means there is no temperature gradient between the flow and the wall.

$$\left(\frac{\partial T}{\partial n}\right)_{wall} = 0 \tag{2.92}$$

2.4.2 Inflow conditions

Inflow boundary conditions are required when analyzing each device with inflow, such as the nozzle, test-section, and diffuser. In the present study, two types of inflow conditions can be used: the general inflow condition, which assumes that the inflow is a uniform flow, and the inflow condition which saved flow information of upstream.

A. General inflow condition

For the general inflow condition, which assumes that the inflow is uniform, the boundary can be given with three user inputs: pressure, temperature, and velocity or mass flow. If the mass flow rate is set as the inflow condition, the axial velocity is calculated for each cell using the specific density calculated by the area of the inflow boundary condition cells. The specific density is calculated by input pressure and temperature.

B. Inflow condition from CFD solution

The inflow condition using the analysis information of the upstream component is useful to understand the performance or analyze the characteristics by changing the downstream condition under the same inflow condition. For example, the diffuser analysis is performed for various configurations and back pressure conditions for diffuser design, it is inefficient to perform numerical analysis with the same nozzle. Therefore, the calculation time can be greatly reduced by performing the nozzle-only analysis separately, saving the exit flow information, and then using it as the inflow condition of the diffuser analysis. Figure 2.8 shows this inflow condition for better understanding. In this case, the shape and grid of both devices must be the same.

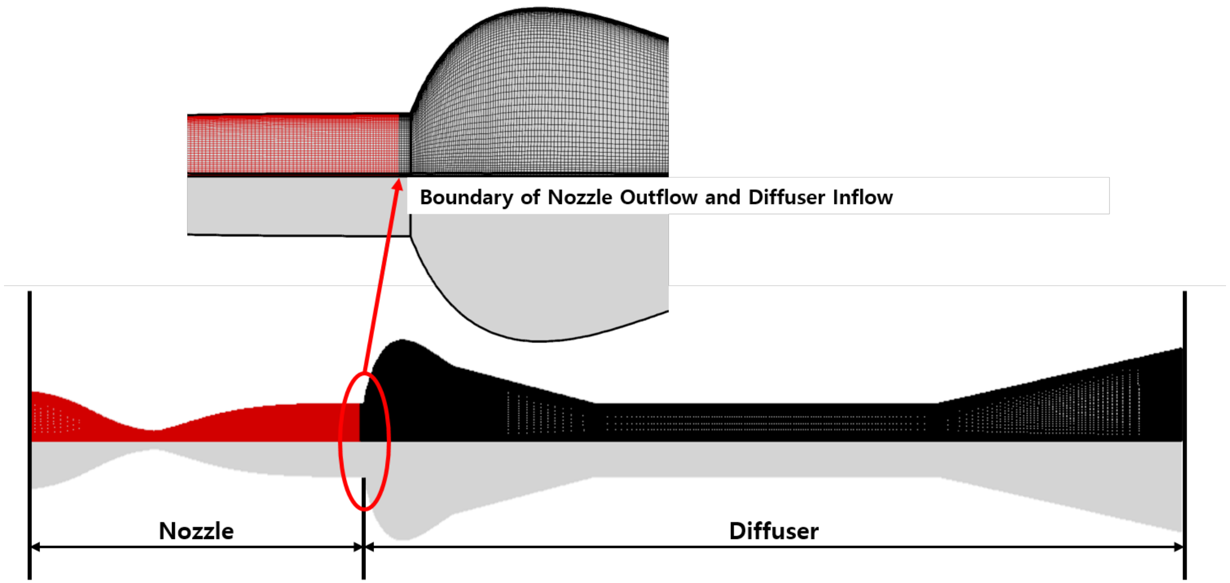

Figure 2.8: An example of inflow condition from saved data

2.4.3 Outflow conditions

A. Supersonic/hypersonic outflow condition

In the numerical analysis of the components in the arc-heated wind tunnel, except for the pressure recovery system (nozzle, test section, etc.), the outflow is supersonic and hypersonic. Therefore, an outflow boundary condition obtained by extrapolating the values of the inner computational domain is used.

B. Constant pressure outflow condition

During the actual operation of the arc-heated wind tunnel, the experimental flow passes through each component and flows into the vacuum chamber, and the pressure in the back gradually increases with time. When the steady state solution is obtained for a specific time during device operation, the constant pressure outflow condition must be used to simulate it. The constant pressure outflow condition performs analysis by assigning constant back pressure of user input only to the pressure value to the value obtained by extrapolating the inner cells.

2.4.4 Axisymmetric boundary condition

As the axial boundary condition, the axisymmetric boundary condition is used. This boundary condition gives only the opposite velocity component in the radial direction to the value of the inner computational cell so that there is no flux gradient in the radial direction from the axis.

2.4.5 Injection boundary condition

Among the components of the arc-heated wind tunnel, the working gas is injected through the arc heater through the gap between the constrictor disks or between the electrodes, and when there is a plenum mixing chamber or ejector, additional mass flow flows into the wind tunnel. To simulate this, an injection boundary condition is required. For the gas injection boundary, the amount of injection mass flow rate and the direction is set at the user input. As the gap and diameter of the injection holes are known, each injection area can be calculated, and the velocity of the injected air also can be calculated using Equations (2.93) and (2.94) derived from the definition of mass flow rate. Then, the injected air velocity is used as the boundary condition of the injection hole, and the other flow values are the same as the wall boundary condition.

$$u = \frac{\dot{m}_{\text{inject}}}{\rho A_{\text{inject}}} \vec{n}_{x,inject} \tag{2.93}$$

$$v = \frac{\dot{m}_{\text{inject}}}{\rho A_{\text{inject}}} \vec{n}_{y,inject} \tag{2.94}$$

2.5 Validation and Verification

ARCFLO4 code validation was performed by analyzing various arc heaters. [43] However, before proceeding with the study, to verify the high-pressure and high-temperature arc flow analysis, the analysis is performed for a representative small heater and large heater respectively. In addition, the present study needs to analyze a hypersonic arc-heated wind tunnel, and the accuracy of the analysis program in the hypersonic region should be validated and verified. Therefore, a flow analysis of nozzles in arc-heated scramjet test facility (AHSTF) [5] is performed.

2.5.1 High pressure and high temperature arc flow

JAXA 0.75MW heater and NASA Ames 20 MW AHF heater analysis are performed, and verification is performed by comparing the experimental values with the numerical results.

A. JAXA 0.75 MW heater

The configuration, analysis condition, and experimental results of the JAXA 0.75 MW heater are same as those used by Sakai et al. [44] and Lee et al. [45]. Among many analysis cases, analysis was performed for three cases of the mass flow rate of 10, 16, and 20g/s with current 300 A. Four variables, the total pressure in chamber, arc-voltage, mass averaged enthalpy at nozzle throat, and efficiency, are compared with the experimental values, and the results are shown in Figure 2.9. The results are in good agreement with the experimental values without significant differences.

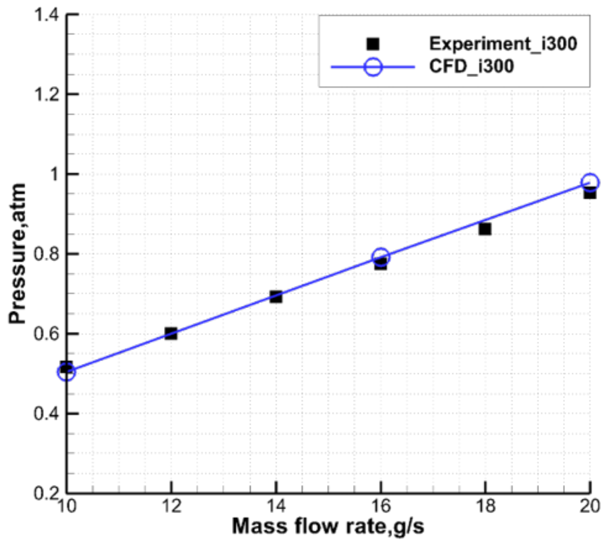

(a) Chamber pressure

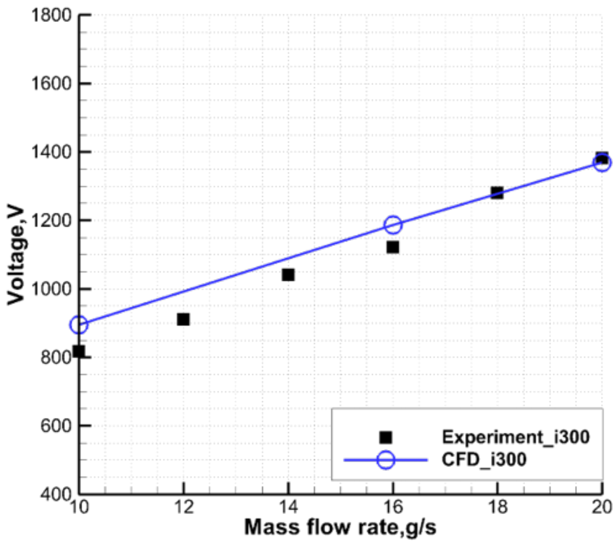

(b) Arc-voltage

Figure 2.9: JAXA 0.75 MW heater results(Cont.)

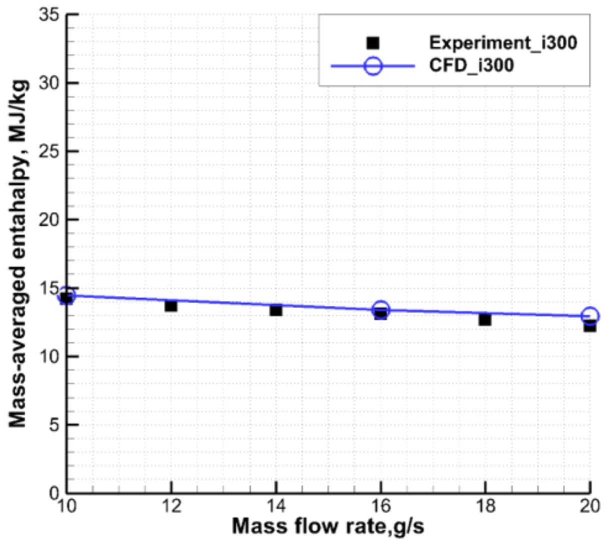

(c) Mass averaged enthalpy

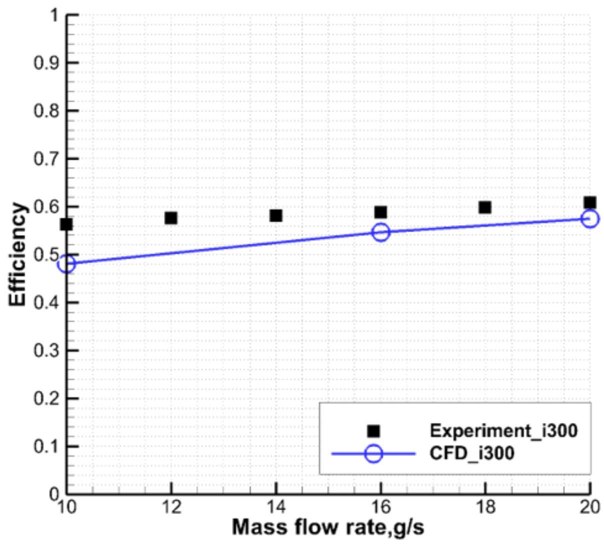

(d) Efficiency

Figure 2.9: JAXA 0.75 MW heater results

B. NASA Ames 20 MW AHF heater

The configuration, analysis condition, and experimental results of the NASA Ames 20MW AHF heater are the same as those used by Kim. [43] Among the analysis conditions, analysis was performed for four cases of mass flow rate 0.05, 0.15, 0.35, and 0.45 kg/s with current 1,600 A. Four variables, chamber total pressure, arc-voltage, mass averaged enthalpy at nozzle throat, and efficiency, are compared with the experimental values, and the results are shown in Figure 2.10. As a result of the comparison, the results are in good agreement without significant differences.

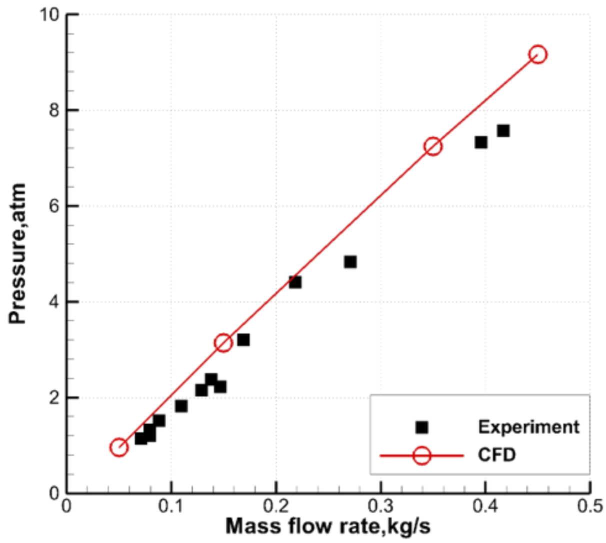

(a) Chamber pressure

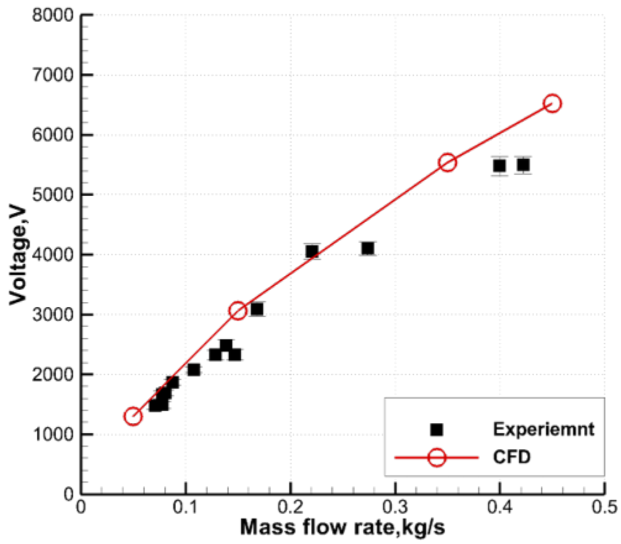

(b) Arc-voltage

Figure 2.10: 20 MW AHF heater results(Cont.)

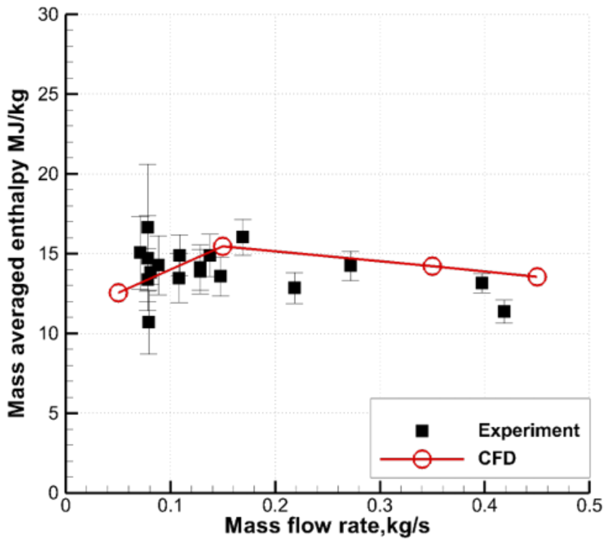

(c) Mass averaged enthalpy

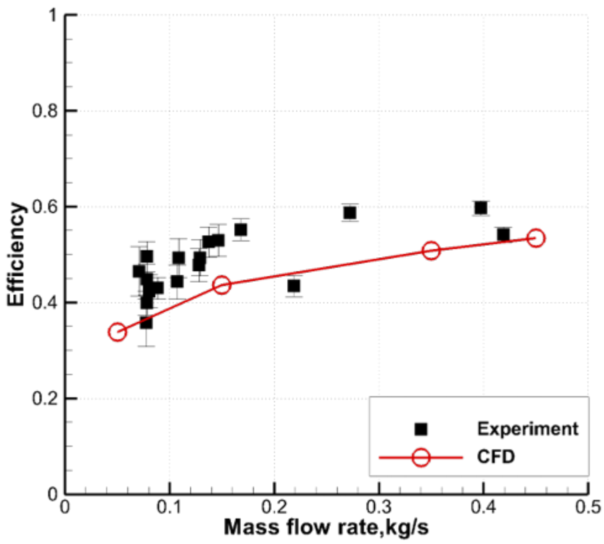

(d) Efficiency

Figure 2.10: 20 MW AHF heater results

2.5.2 Supersonic/Hypersonic flow

Flow analysis of nozzles with exit Mach numbers 4.9 and 6 was performed. The configuration and analysis conditions of the nozzle have been presented, [5,46] and are summarized in Tables 2.1 and 2.2. The results of the pressure and temperature at the nozzle exit are shown in Figure 2.11. On comparing the results with the experimental values, the averaged exit pressure and temperature showed an error range of 2.6–13.3 % and 7.3–14.5 %, respectively. In addition, the three turbulence models were within 0.007 % for temperature and 0.09 % for pressure; this difference is not significant.

The difference between experimental and CFD results can be attributed to the assumption of an equilibrium flow in the nozzle. It is generally known that the non-equilibrium effect increases inside the nozzle; [21] Therefore, the difference between the analysis results and experimental values is inevitable. In addition, the error value of the M6 nozzle, which increases the non-equilibrium effect due to the high-speed flow, is larger than that of the M4 nozzle. However, despite this difference, the code was used in this study because the computation time is more efficient than those of non-equilibrium analysis code, and getting a solution in a short time is important for the initial design.

Table 2.1: Configuration information of AHSTF nozzles

Nozzle Case	Exit Mach Number	Throat Area, m^2	Effective Area, m^2
M4.9 Nozzle	4.9	2.45×10^{-3}	67.1×10^{-3}
M6 Nozzle	6.0	0.89×10^{-3}	67.1×10^{-3}

Table 2.2: Experimental results of AHSTF nozzles

Case	Mass Flow Rate, kg/s	Reservoir Condition			Exit Condition		
		pressure, atm	Entalphy, MJ/kg	Temperature, K	Mach Number	Pressure, atm	Temperature, K
M4.9 Nozzle1	4.99	13.6	1.20	1123	4.8	0.033	212
M4.9 Nozzle2	4.54	13.1	1.33	1251	4.8	0.031	236
M4.9 Nozzle3	3.58	11.2	1.61	1468	4.8	0.027	285
M6 Nozzle1	2.91	35.1	1.84	1655	6.1	0.018	217
M6 Nozzle2	2.05	28.6	2.58	2216	6.0	0.014	306
M6 Nozzle3	1.43	23.0	3.56	2879	6.0	0.012	427

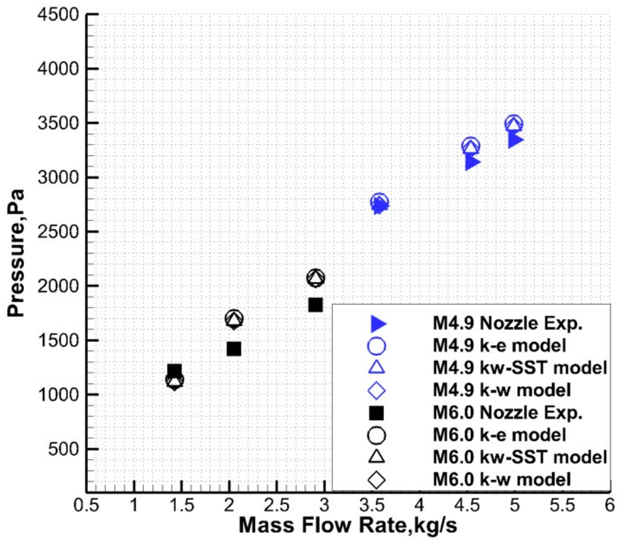

(a) Averaged pressure

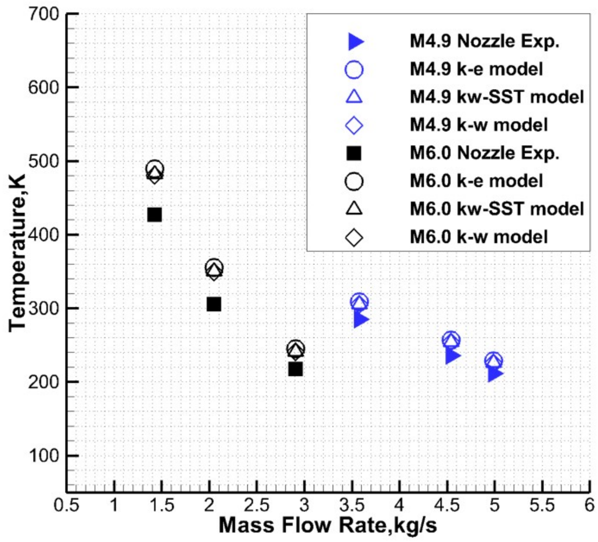

(b) Averaged temperature

Figure 2.11: NASA AHSTF supersonic/hypersonic nozzle exit results

CHAPTER 3. NUMERICAL ANALYSIS AND INVESTIGATION

In Chapter 3, numerical analysis and investigation are performed on an arc-heater with plenum mixing chamber and diffusers of an arc-heated wind tunnel. In section 3.1, a numerical study is conducted on a plenum mixing chamber with a heater nozzle that can secure the stability of arc plasma in the preliminary design and initial construction. In section 3.2, the numerical study of the various types of diffusers is performed. The numerical analysis on a center-body diffuser and second throat cylindrical diffuser, under the same arc-heated facility condition, is performed, and their characteristics are identified. Through numerical analysis of diffusers, a novel diffuser configuration that compensates for the disadvantages of existing diffusers is proposed, and through performance evaluation, it was confirmed that the novel diffuser can alleviate the requirements of the vacuum system behind the diffuser.

In this chapter, as a variable to identify the characteristics of the wind tunnel, the flow physical quantity (ϕ) is mass averaged and represented. The averaged values are weighted by the mass flow rate because it is conserved inside an arc-heater wind tunnel, and it clearly shows the tendency of the physical phenomenon along the axial direction. The averaging equation is shown below.

$$\phi_{avg} = \frac{1}{\int \rho u dA} \int \phi \rho u dA = \frac{1}{\dot{m}} \int \phi \rho u dA \tag{3.1}$$

3.1 Plenum Mixing Chamber with a Heater Nozzle

3.1.1 Arc-heater and plenum mixing chamber

Most studies on arc-heaters have already been performed: such as, a study on characterization using arc-heater flow analysis [18, 43], heater sizing study using scaling study [14, 47], empirical and experimental research on arc-heater [48], and arc-heater design and manufacturing research using CFD. [11] In the present study, a heater with plenum mixing chamber (PM) is numerically analyzed, and the reservoir flow characteristics of the arc-heated wind tunnel with PM are studied.

The plenum mixing chamber (PM) of an arc-heater is located behind the arc-heater and in front of the nozzle as shown in Figure 3.1, and its shape varies. The PM is a device making the temperature distribution of the high-temperature flow generated by the heater uniformly in the radial direction, and it lowers the enthalpy of the experimental flow by injecting additional mass flow. By adding the PM, the operating envelope of the heater is widened, and representative examples of PM are the plenum chamber of NASA's Langley AHSTF [49] and stilling chamber of AEDC's H-series [50, 51].

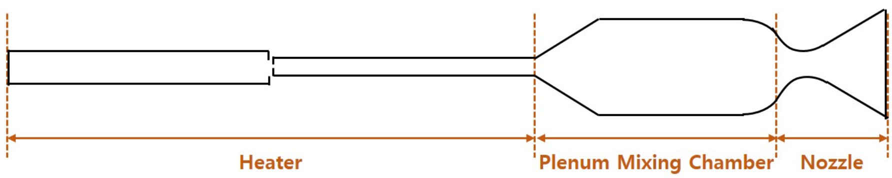

Figure 3.1: Schematic of an arc-heater with plenum mixing chamber

3.1.2 Plenum mixing chamber with heater nozzle

The additional mass flow of room-temperature gas into the plenum mixing chamber can lower the enthalpy of the experimental flow; thus, the operating range of the facility can be extended. If both the flow inside the heater and the PM are subsonic, additional flow injection may affect the upstream causing disturbances to arc-plasma inside the heater. As a result, the reservoir condition can be unstable, and this may cause a decrease in the reliability of experimental results.

In the present study, the concept of a heater nozzle, shown in Figure 3.2, is adapted to separate the heater and plenum mixing chamber flow. The high-temperature flow of an arc-heated facility is generated by discharge inside an arc-heater after making all components are vacuum state; therefore, a method to prevent the additional working gas flows into the heater from disrupting arc-plasma starting is required. Moreover, the disturbance of arc-plasma should be prevented by the change of the working gas injected into the PM during an experiment. Therefore, to ensure a stable arc-plasma state by generating flow choking between the arc-heater and the PM, a heater nozzle is used. To verify the role of the heater nozzle, a numerical study on a general PM case in which the internal flow of the heater and the PM is subsonic and PM with heater nozzle is performed.

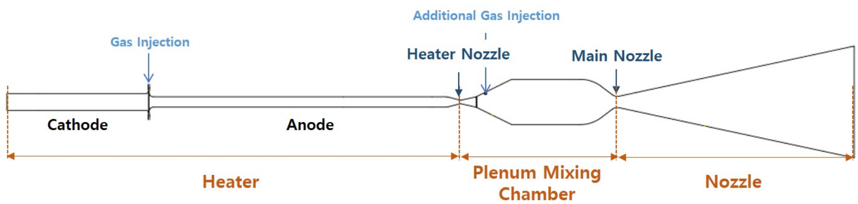

Figure 3.2: Schematic of an arc-heater with plenum mixing chamber and heater nozzle

A. Configuration and analysis condition

Figure 3.3 shows the computational domain including the configuration, grid, and boundary conditions for the general PM case. Figure 3.4 shows the configuration and computational domain when the heater and PM are choked. The specification and analysis conditions of the two cases are summarized in Table 3.1.

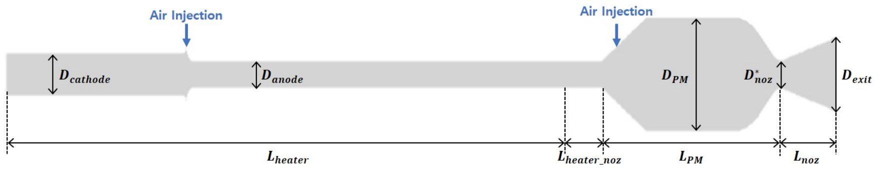

(a) Configuration

(b) Grids and boundary conditions

Figure 3.3: General PM configuration and computational domain

(a) Configuration

(b) Grids and boundary conditions

Figure 3.4: PM with heater nozzle configuration and computational domain

Table 3.1: Specification and analysis condition of the PM

Specifications (unit:cm)				
Heater			Plenum Mixing Chamber	
$D_{cathode}$	D_{anode}	L_{heater}	D_{PM}	L_{PM}
9.5	5.8	248	25	80
Heater Nozzle		Main Nozzle		
D^*_{heater}	D_{heater_noz}	D^*_{noz}	D_{exit}	L_{noz}
2.0	17	6.3	28	52

Analysis Condition		
Current, A	Mass Flow Rate, kg/s	
	Heater	Plenum Mixing Chamber
2,200	1.0	4.0

B. Results and analysis

Flow analysis of both the general case (i.e., without choking case) and the PM with heater nozzle case (i.e., choking case) are performed. Figure 3.5 shows the pressure contours and averaged pressure of the two cases. In the PM with heater nozzle case, the pressure inside the heater is higher than that of the general PM by the choking effect at the heater nozzle throat; whereas in the general case, the pressure of the heater and the PM was kept similar to about 16-18 atm. In temperature comparison, shown in Figure 3.6, the shape, length, and center temperature of the arc created inside the heater are similar in both cases. However, when there is no flow choking, the heated flow from the heater expands relatively less in the PM and maintains the temperature, and it is confirmed that the average temperature inside the chamber is 1500 K, which is higher than 1000 K of the choking case. Figure 3.7 shows the Mach number contour and averaged Mach number. In the general case, choking occurs at the main nozzle throat, and the flow velocity of the heater and plenum mixing chamber is maintained in subsonic.

In order to analyze the mixing of high-temperature air heated by the heater and additional room-temperature gas injected into the PM, Figure 3.8 compares the radial temperature distributions for each position inside the chambers of the two cases. In the case where flow choking occurs, the high-temperature gas expands supersonic by the heater nozzle, and the flow temperature decreases from the entrance of the chamber (Figure 3.8a), and the central temperature is lower than in the general case at all locations. In Figures 3.8b, 3.8c, and 3.8d, an additional injected air region forms near the wall and mixes with the high-temperature gas, and in both cases the core temperature gradually decreases. The flow temperature of the additional gas area near the wall is higher in the general case because as the high-temperature gas in the choked case is supersonic, the difference in momentum with the injected air is large, so heat transfer occurs actively to the low-temperature injected gas. Therefore, in Figures 3.8e, 3.8f, and 3.8g, which is the rear part of the plenum mixing chamber, the PM with heater nozzle case completes the mixing of the additional low enthalpy air and high enthalpy air, resulting in uniform temperature distribution, while the general case (without choking), the center temperature remains high, and it can be seen that the mixing of the two flows is not completely achieved inside the chamber. Figure 3.8h, which is the temperature distribution in the radial direction at the main nozzle throat, also shows that the temperature distribution in the general case is nonuniform.

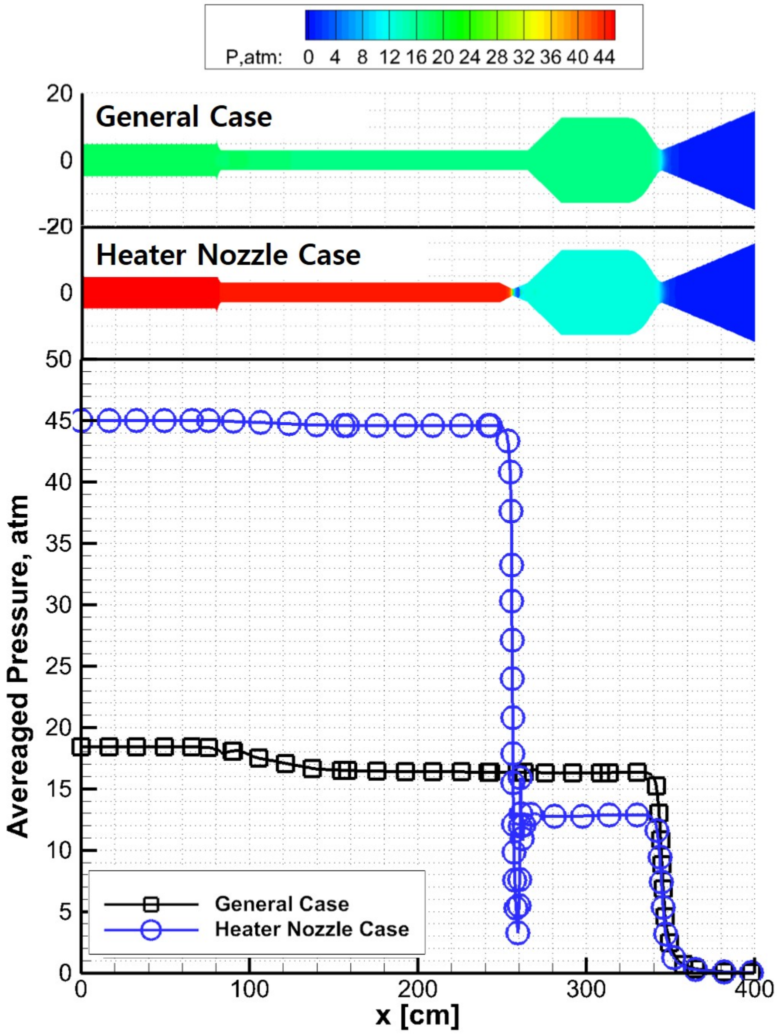

Figure 3.5: Pressure results of two PM cases

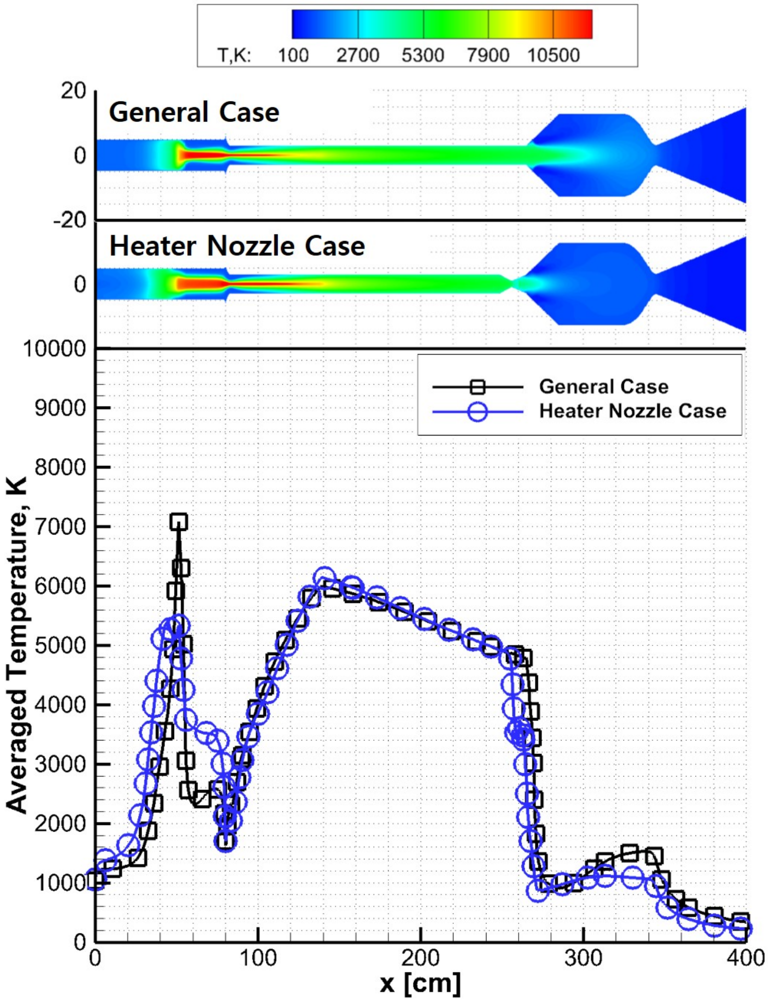

Figure 3.6: Temperature results of two PM cases

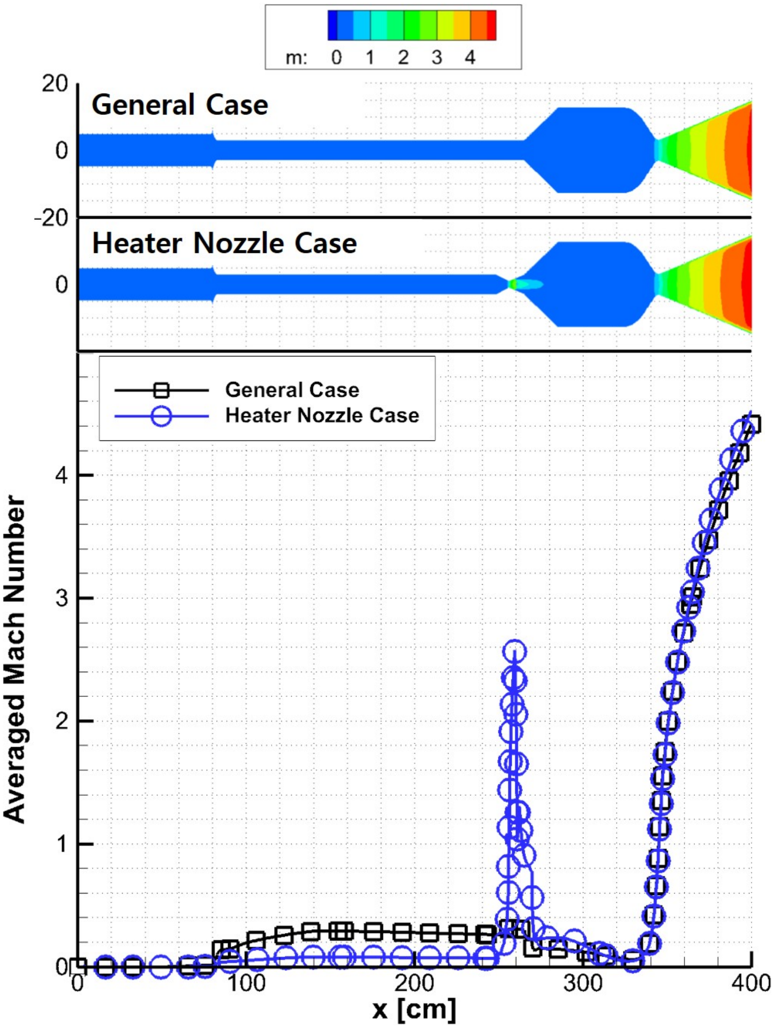

Figure 3.7: Mach number results of two PM cases

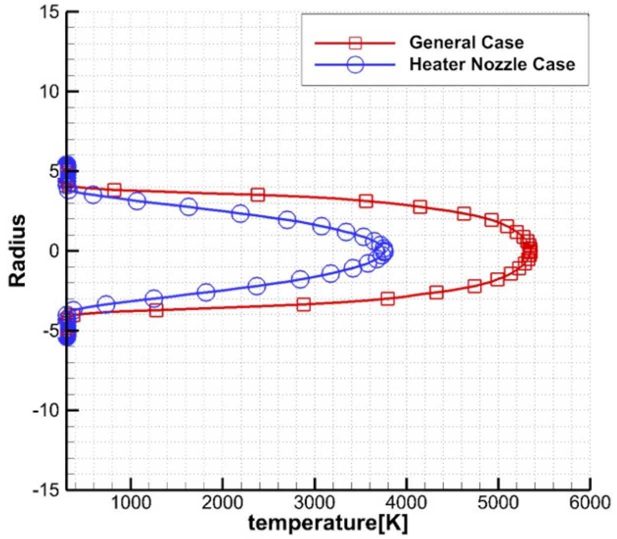

(a) x=270(Injection area)

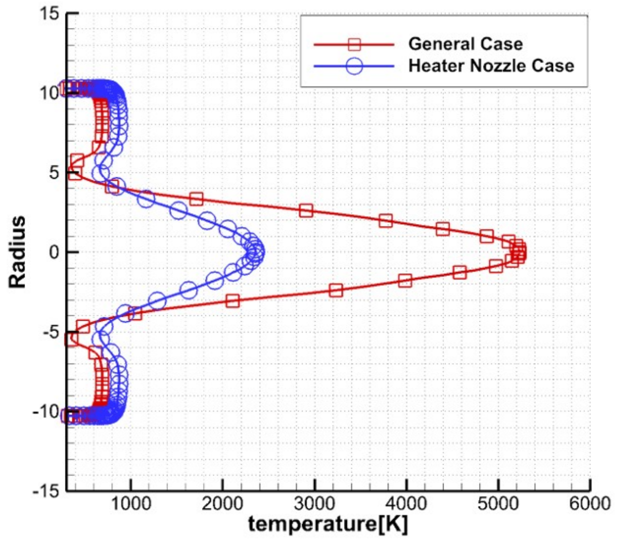

(b) x=280

Figure 3.8: Radial temperature distributions along the axis (Cont.)

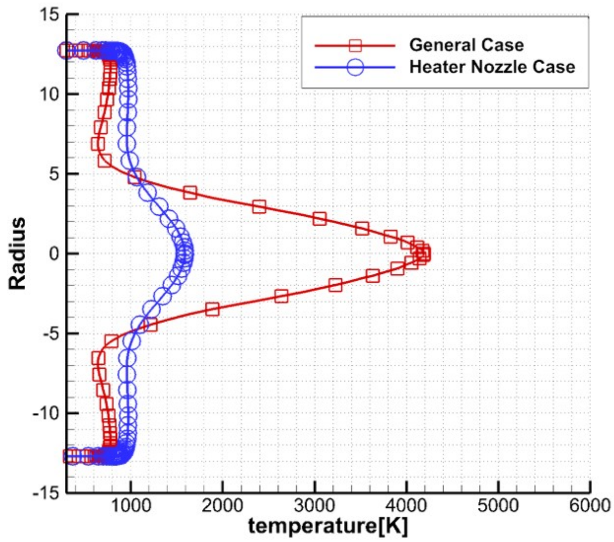

(c) x=290

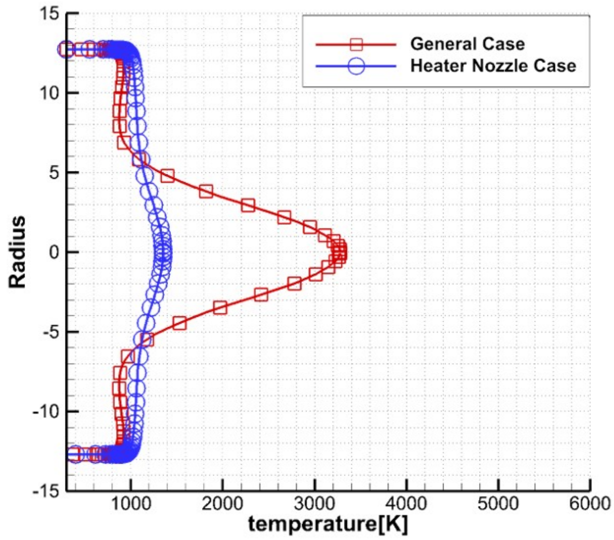

(d) x=300

Figure 3.8: Radial temperature distributions along the axis (Cont.)

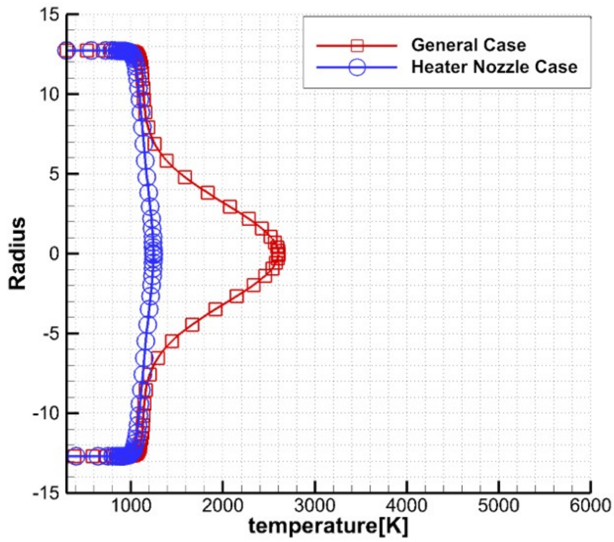

(e) x=310

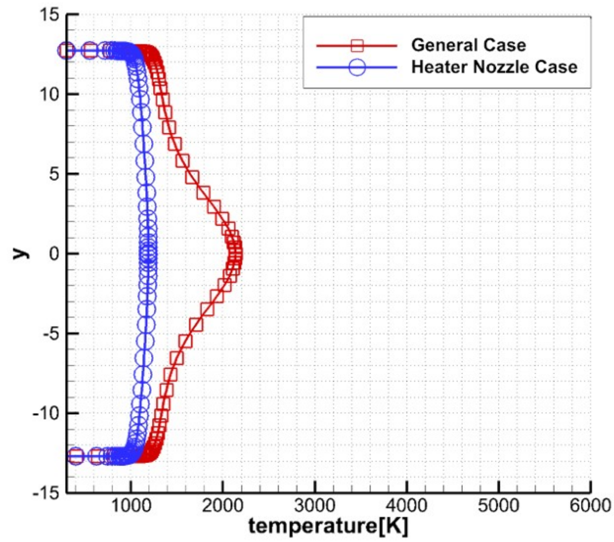

(f) x=320

Figure 3.8: Radial temperature distributions along the axis (Cont.)

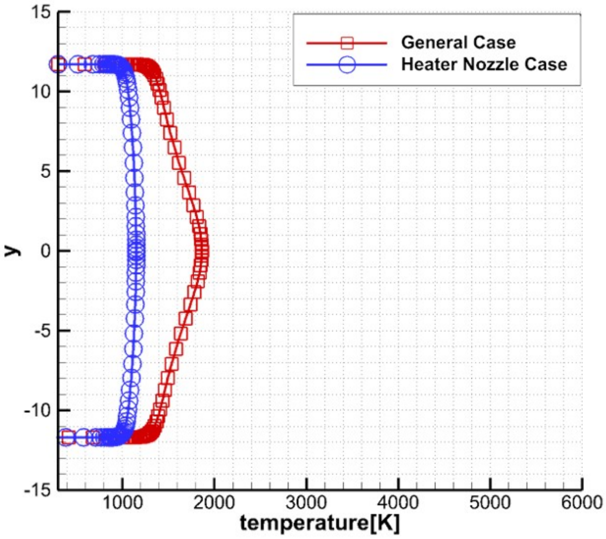

(g) x=330

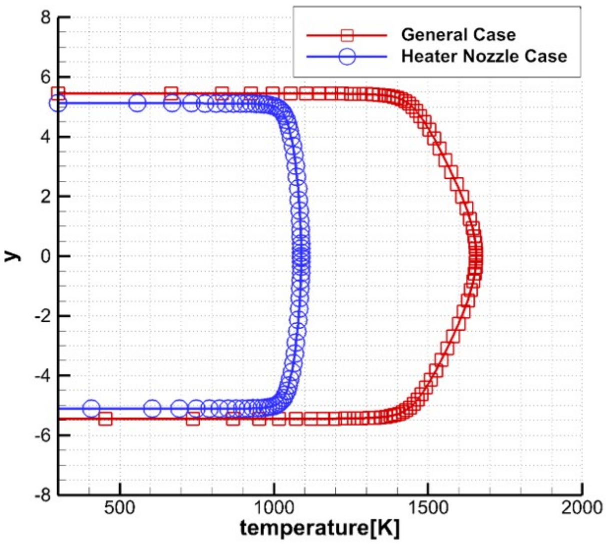

(h) x=340(Main nozzle throat)

Figure 3.8: Radial temperature distributions along the axis

C. Loss in the heater nozzle

When using the heater nozzle, the high-temperature main flow generated by the arc-heater accelerates and expands to supersonic flow, resulting in total pressure loss and enthalpy loss of the main flow. To grasp the amount of flow loss by the heater nozzle, the total pressure is compared with the case without a heater nozzle and shown in Figure 3.9. In the case of a heater nozzle, the total pressure ratio of the plenum mixing chamber and the heater ($P_{0,PM}/P_{0,\text{heater}}$) was 0.28, resulting in a total pressure loss of 72 $\%$, while the total pressure ratio of 'general case (i.e., no choking case)' was 0.9, confirming that the loss 10 $\%$ occurred. Because the total pressure of the reservoir performing the experiment is the total pressure of the plenum mixing chamber, through the total pressure ratio of the two cases ($P_{0,PM\text{heater noz}}/P_{0,PM\text{general}}$), it can be confirmed that about 30 $\%$ of the reservoir total pressure loss occurs when there is a heater nozzle.

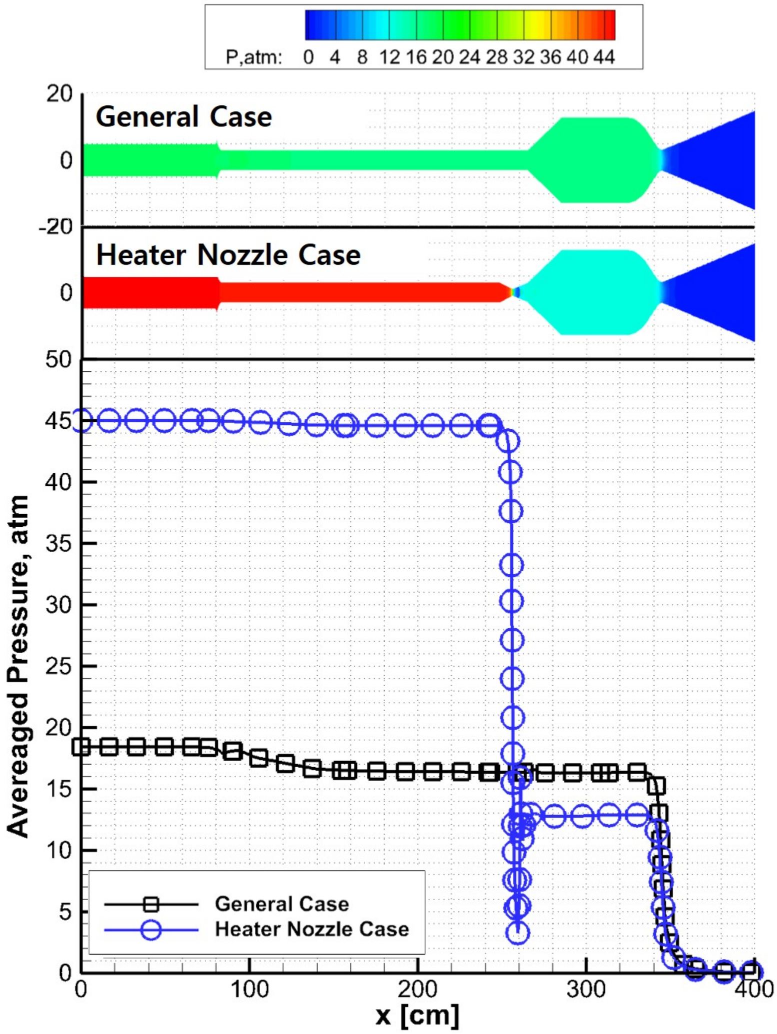

Figure 3.9: Total pressure results of two PM cases

3.1.3 Results and analysis depending on additional injection flow rate and direction

In order to confirm that there is no change in the heater flow when the flow changes in the plenum mixing chamber as intended by the configuration design of the heater nozzle, the mass flow rate and injection direction of the additional injection into the chamber were different from the base case and the analysis is performed. A total of four cases of information are summarized in Table 3.2.

Table 3.2: Case information of additional injection

Case Name	Mass Flow Rate,kg/s	Inject Direction
Base	4.0	Radial Direction
Axial Injection	4.0	Axial Direction
PM MFR1	1.0	Radial Direction
PM MFR2	2.5	Radial Direction

The temperature and streamlines of each case are shown in Figure 3.10. In the base case of Figure 3.10a, the low-enthalpy flow meets the high-velocity high-enthalpy flow, and momentum direction change occurred, creating a circulation region. Meanwhile, in the axial inject case, the momentum direction of the high-speed heater flow and the additional injection flow are the same, so there is no circulation area in the mixing chamber. In addition, comparing the temperature contours of the two cases, it is judged that the low enthalpy flow is not used for mixing as much as the area shown in Figure 3.10b and flowed to the back of the mixing chamber and is not mixed with the high-temperature flow as much as the base case. In Figures 3.10c and 3.10d, where the additional gas injected into the chamber is smaller than that of the base case, the temperature inside the mixing chamber increased as the mass flow rate of the low enthalpy flow decreased. The pressure inside the chamber of the PM MFR 1 case is 5 atm, and the PM MFR 2 case is 10 atm.

Figure 3.11 is the radial direction temperature distribution according to the location in the mixing chamber of each case. In the base case, it is confirmed that the low-enthalpy flow region from the wall to the radial direction occupied a larger portion than the axial inject case, and the temperature distribution became uniform. The average temperature at the end of PM inside the chamber of the base case is about 100 K lower than that of the axial injector.

Meanwhile, the flow and performance of the heater are the same in all cases due to choking between the heater and the mixing plenum chamber. In Figure 3.12, which shows the temperature distribution in the radial direction inside the heater in all cases, and Table 3.3, which summarizes the variables representing the performance, it can be seen that the inside of the heater is not affected even if the flow in the chamber changes.

Table 3.3: Heater performaces for all cases

	Arc Voltage [V]	Pressure [atm]	Mass-averaged entahlpy [MJ/kg]	Efficiency
Base	4,114	45	7.2	0.3
Axial Injection	4,115	45	7.2	0.3
PM MFR1	4,113	45	7.2	0.3
PM MFR2	4,114	45	7.2	0.3

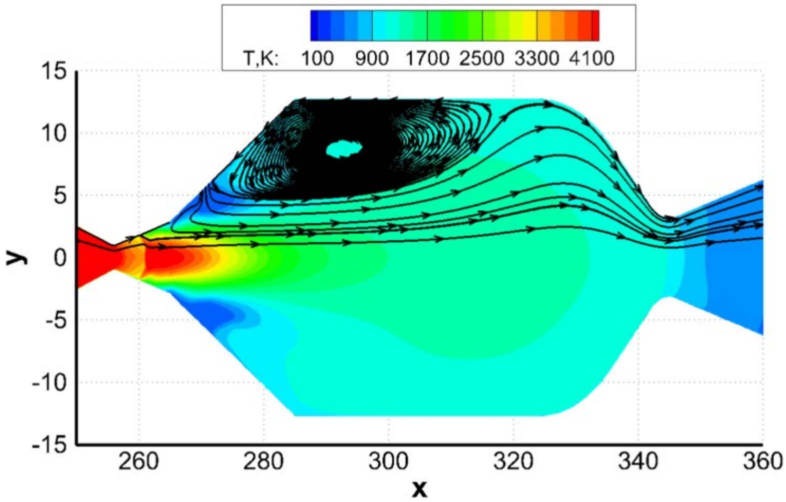

(a) Base case

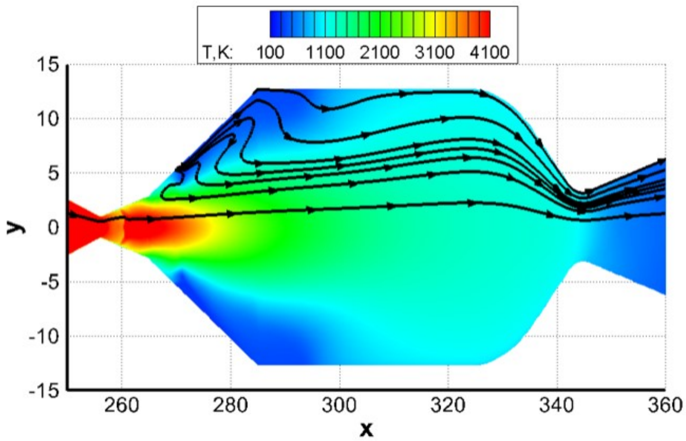

(b) Axial injection case

Figure 3.10: Temperature and streamlines inside the PM (Cont.)

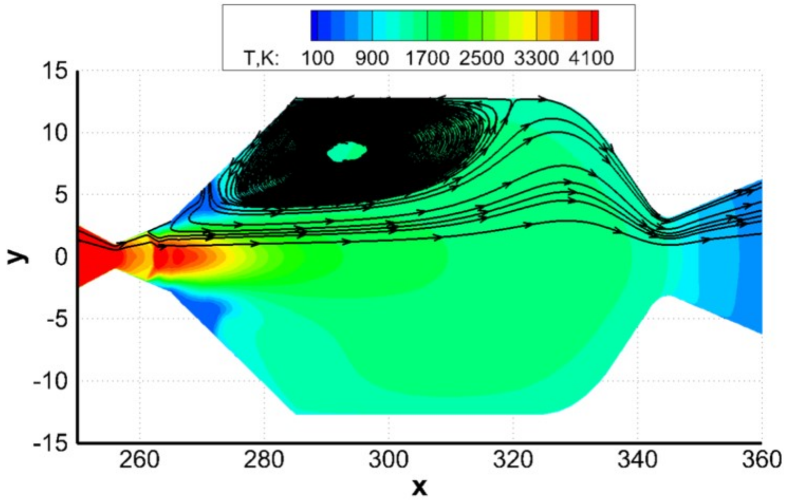

(c) PM MFR1 case

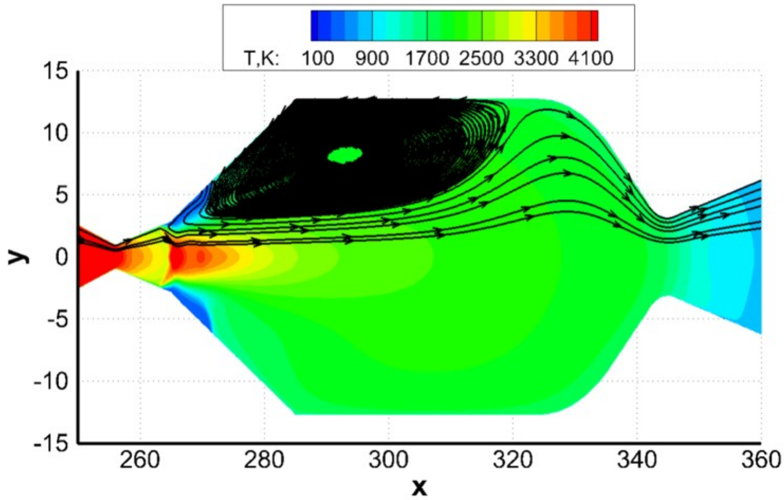

(d) PM MFR2 case

Figure 3.10: Temperature and streamlines inside the PM

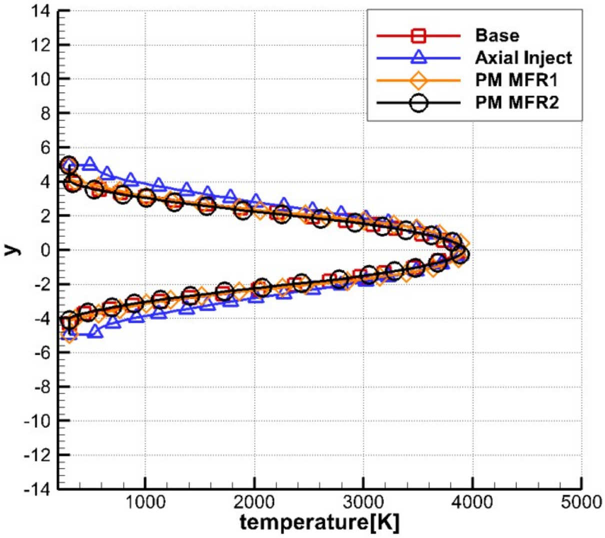

(a) Heater nozzle exit

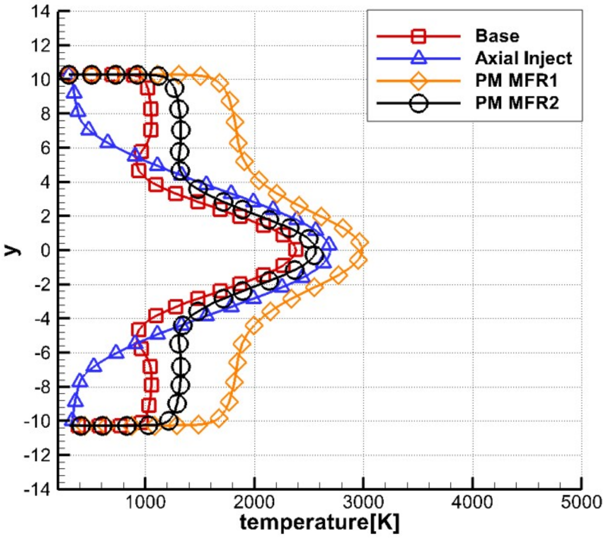

(b) Additional injection area

Figure 3.11: Radial temperature distributions of various inject cases (Cont.)

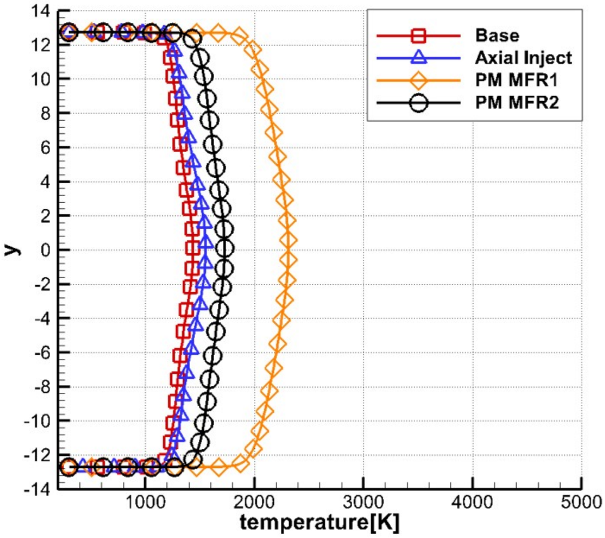

(c) Center of the PM

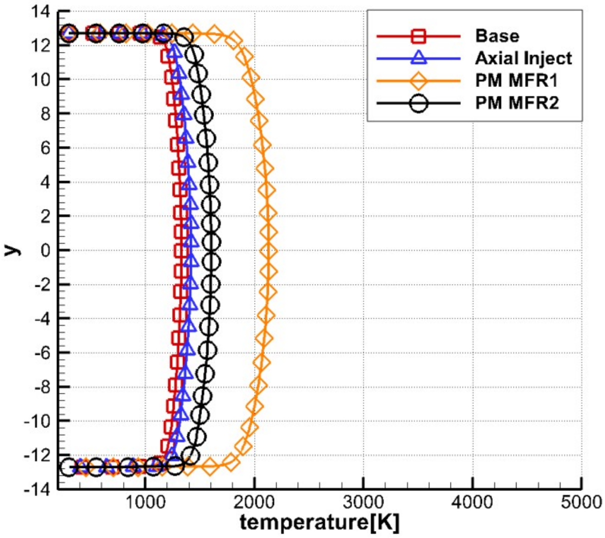

(d) End of the PM

Figure 3.11: Radial temperature distributions of various inject cases

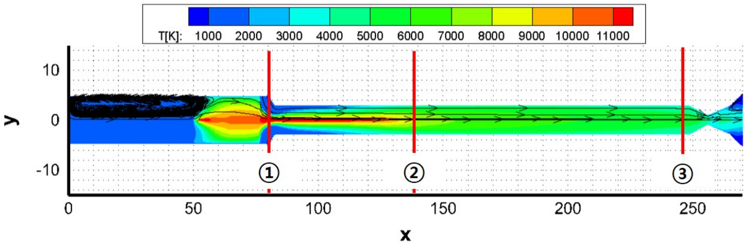

(a) Radial distribution results location inside the heater

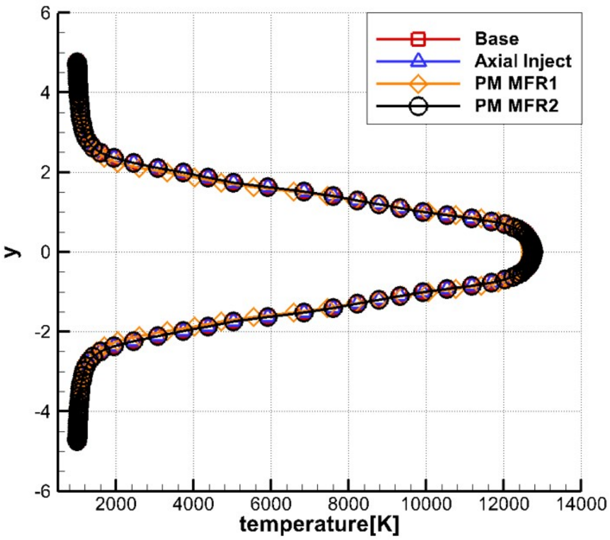

(b) Heater location 1

Figure 3.12: Radial temperature distributions inside the heater (Cont.)

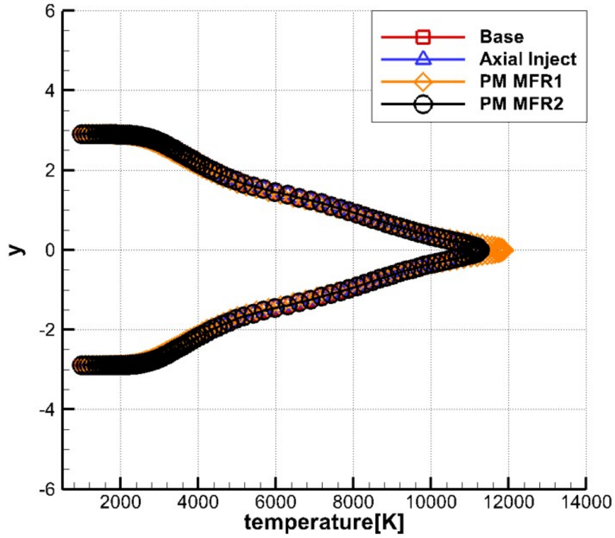

(c) Heater location 2

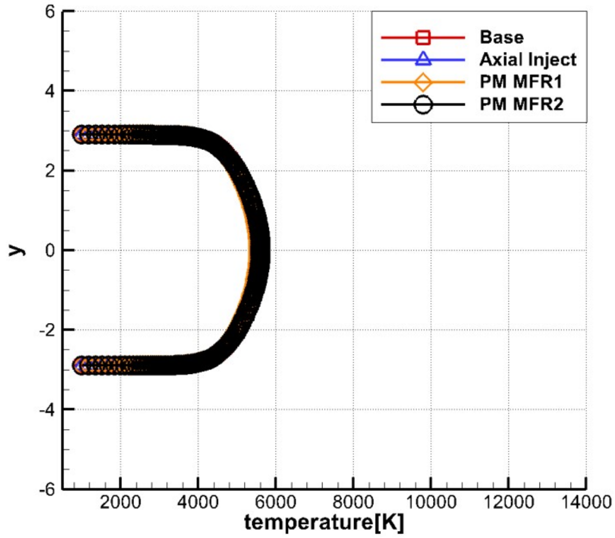

(d) Heater location 3

Figure 3.12: Radial temperature distributions inside the heater

3.1.4 Parametric study on heater nozzle

Since the flow loss by the heater nozzle is caused by the high-temperature main flow expanding to supersonic flow, it is expected that the flow loss will decrease if the exit Mach number of the heater nozzle is lowered. Methods of lowering the exit Mach number include: first, reducing the nozzle exit area, second, increasing the nozzle throat area. Therefore, using the heater nozzle configuration in the previous section as the base case, a parametric study is performed on case 1 in which the nozzle exit area is reduced, case 2 in which the nozzle throat area is increased, and case 3 in which the nozzle exit area is reduced and the nozzle throat area is increased. Only the throat and exit diameters of the heater nozzle are changed based, and the nozzle throat area and nozzle exit area information for each case are summarized in Table 3.4.

Table 3.4: Case information of heater nozzles

	Base	Case 1	Case 2	Case 3
D^* [cm]	2.0	2.0	2.83	2.83
A_{exit}/A^*	8.27	4.13	4.13	2.07

The averaged total pressure results for each case are shown in Figure 3.13. The heater total pressure of base and case 1 with the same heater nozzle throat area is 45.0 atm, case 2 and case 3 are 22.7 atm, and the 'general case (i.e., no choking case)' where the heater nozzle does not exist is 18.4 atm. To compare the total pressure loss by the heater nozzle, the ratio of the plenum mixing chamber to the heater pressure ($P_{0,PM}/P_{0,\text{heater}}$) and the total pressure ratio of each case to the total pressure of the plenum mixing chamber in the 'no choking case' ($P_{0,PM\text{cases}}/P_{0,PM\text{no choking}}$) are summarized in Table 3.5. The total pressure loss by the heater nozzle was about 0.3 in Base and Case 1, resulting in a loss of 70 %, and Case 2 and Case 3, which had the heater nozzle throat area twice as large, was about 0.6, resulting in a total pressure loss of about 40 %. There was no significant difference in total pressure loss in cases where the exit area of the heater nozzle was reduced while having the same throat area. The total pressure ratio of plenum mixing chamber based on the general case was 0.82 in the case 3, which has the largest heater nozzle throat area and smallest nozzle exit area, and the ratio was 0.05 (5 %) larger than the base case.

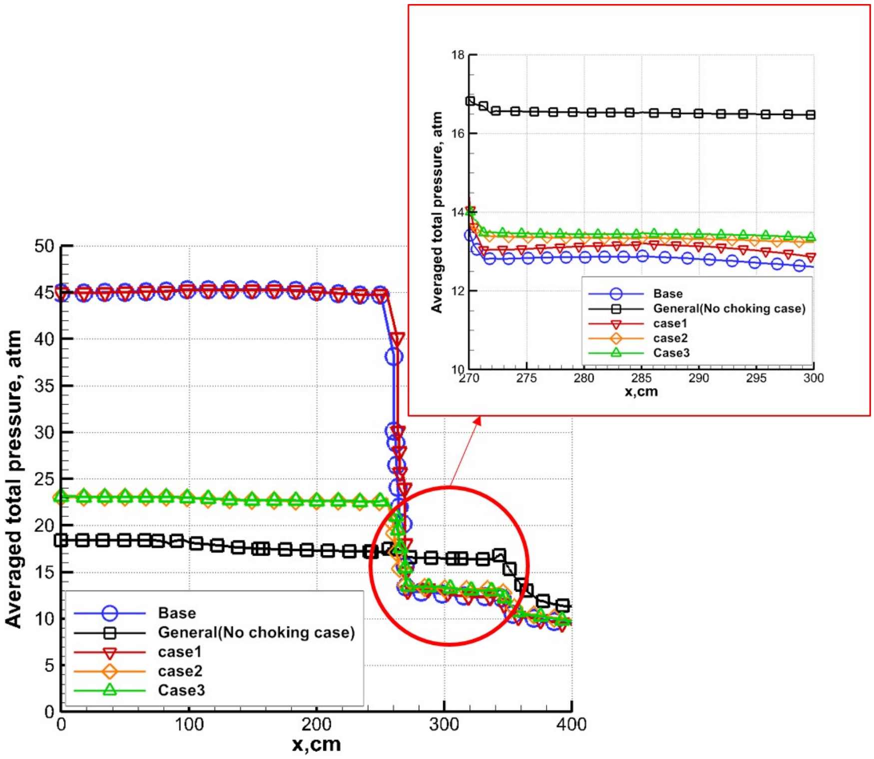

Figure 3.13: Averaged total pressure results of heater nozzle parametric study

Table 3.5: Total pressure and ratio of parametric study

	Base	General	Case 1	Case 2	Case 3
Heater pressure, atm	45.0	18.4	45.0	22.7	22.7
PM pressure, atm	12.7	16.4	13.0	13.3	13.4
$P_{0,PM}/P_{0,\text{heater}}$	0.28	0.89	0.29	0.59	0.59
$P_{0,PM}/P_{0,\text{general}}$	0.7	1.0	0.79	0.81	0.82

A cooling system for the heater and nozzle wall is essential to prevent damage caused by the high enthalpy flow generated in the arc-heater, and melting and ablation of the nozzle throat is severe where heat is concentrated. As heat flux prediction to the wall is required for cooling system design, the heat flux at the heater nozzle throat where the maximum heat flux occurs is calculated for each case and shown in Figure 3.14. The maximum heat flux of the base case is 2.91 kW/cm^2, and the heat flux of the general case (i.e., no-choking case) is 1.49 kW/cm^2 in the same location. The heat flux at the nozzle throat decreased as the nozzle throat area increased.

Through the parametric study, it was confirmed that increasing the heater nozzle throat area is more efficient than decreasing the nozzle exit area in terms of maximum heat flux and flow loss; while the mixing length remains almost same as shown in Figure 3.15.

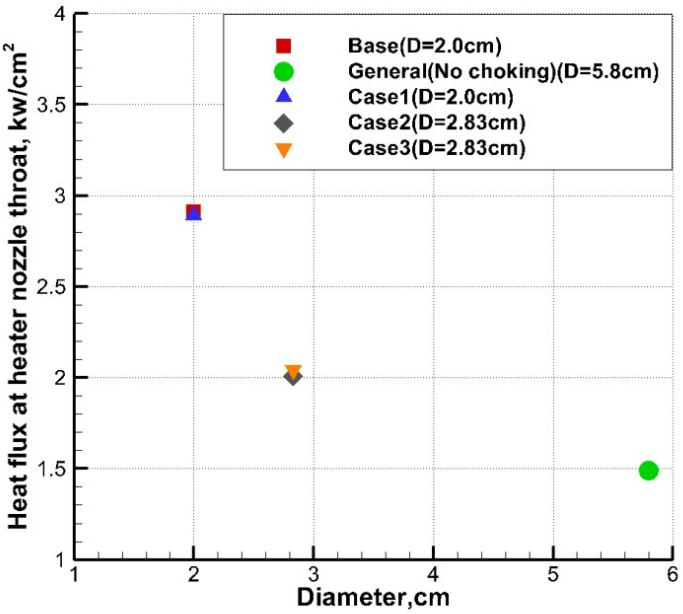

Figure 3.14: Heat flux at the heater nozzle throat

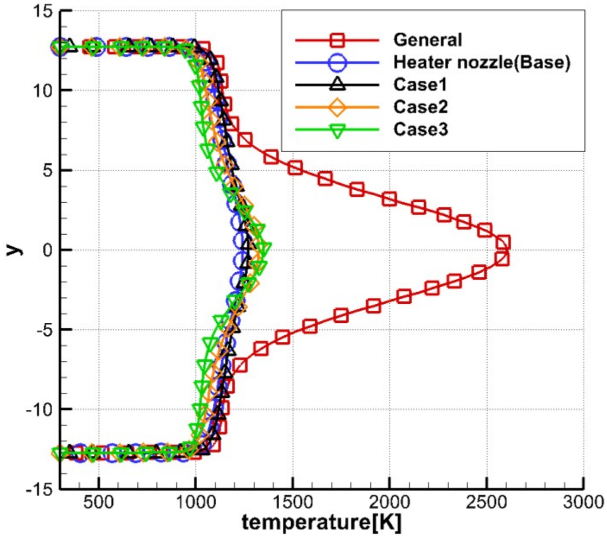

(a) x=310

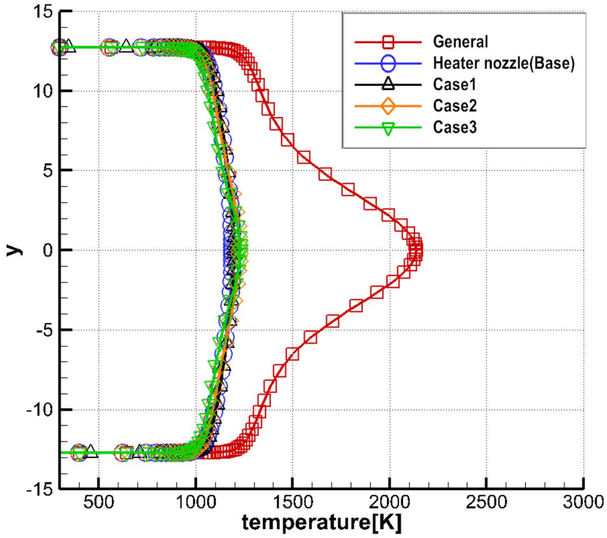

(b) x=320

Figure 3.15: Radial temperature distributions of parametric study cases (Cont.)

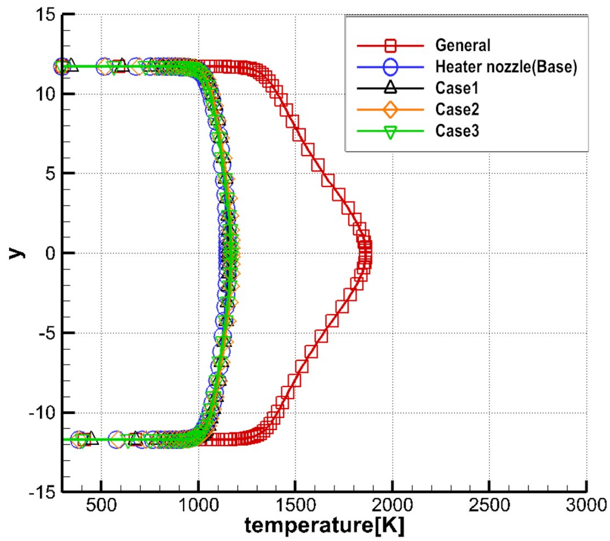

(c) x=330

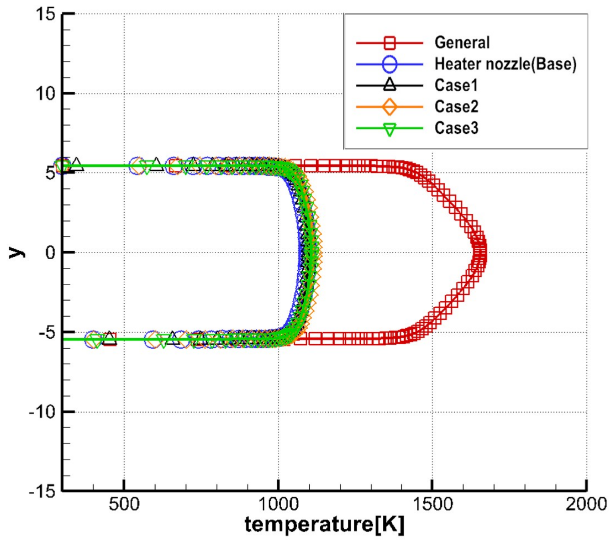

(d) x=340

Figure 3.15: Radial temperature distributions of parametric study cases

3.2 Diffusers in Various Types

3.2.1 General diffusers

There are two types of diffusers: second-throat cylindrical diffuser (Figure 3.16a) and center-body diffuser (Figure 3.16a). They are the most common diffusers of an arc-heated wind tunnel. The center-body type is used in the German Aerospace Center (DLR) L2K and L3K facilities [52], and the second throat cylindrical type is used in NASA Langley arc-heated facilities [5]. Related research on diffusers has been studied for a long time, and the history of it is summarized by Miliigan et al. [53] However, numerical study for each type of diffuser under the same heater and nozzle conditions has not been conducted. Therefore, in the present study, each type of diffuser analysis is performed using the same flow conditions, and each feature is analyzed to identify its strengths and weaknesses.

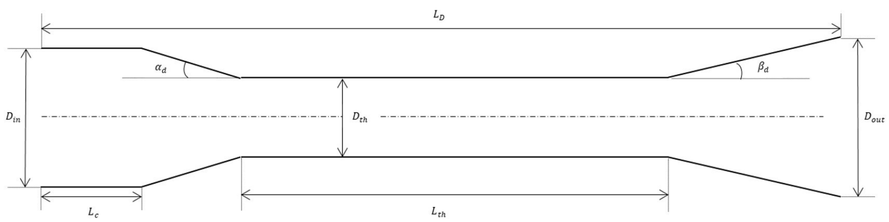

(a) A second throat cylindrical diffuser

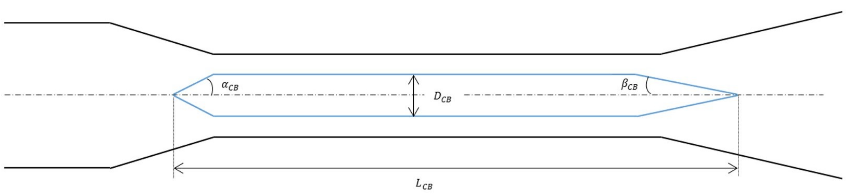

(b) A center-body diffuser

Figure 3.16: Configuration of general diffusers

A. Configuration and analysis conditions

For the comparison of the two cases, the flow was analyzed after fixing the shape of the convergence, throat, and divergent section of the diffuser. The configuration information of the diffusers is summarized in Figure 3.16 and Table 3.6.

The computational domain and grids are shown in Figure 3.17. To understand the flow characteristics of diffusers, flow analysis was performed on the second throat diffuser and a center-body diffuser with the same analysis conditions. For inflow conditions, the M6 Nozzle1 exit condition in the validation and verification section (Section 2.5 in the present study) is used, and the back pressure for each diffuser is set to 6 kPa.

Table 3.6: Specification of diffusers

Catch Cone	L_c [m]	1.0
	D_{in} [m]	1.2
Convergent Part	α_d [$\circ$]	10.0
Throat	A_{in}/A_{th}	2.25
	L_{th}/D_{th}	10.0
Divergent Part	β_d [$\circ$]	6.0
	D_{out} [m]	2.0
Center-Body	L_{CB} [m]	8.9
	D_{CB} [m]	0.16
	α_{CB} [$\circ$]	10.0
	β_{CB} [$\circ$]	10.0
	D_{CB}/D_{th}	0.2

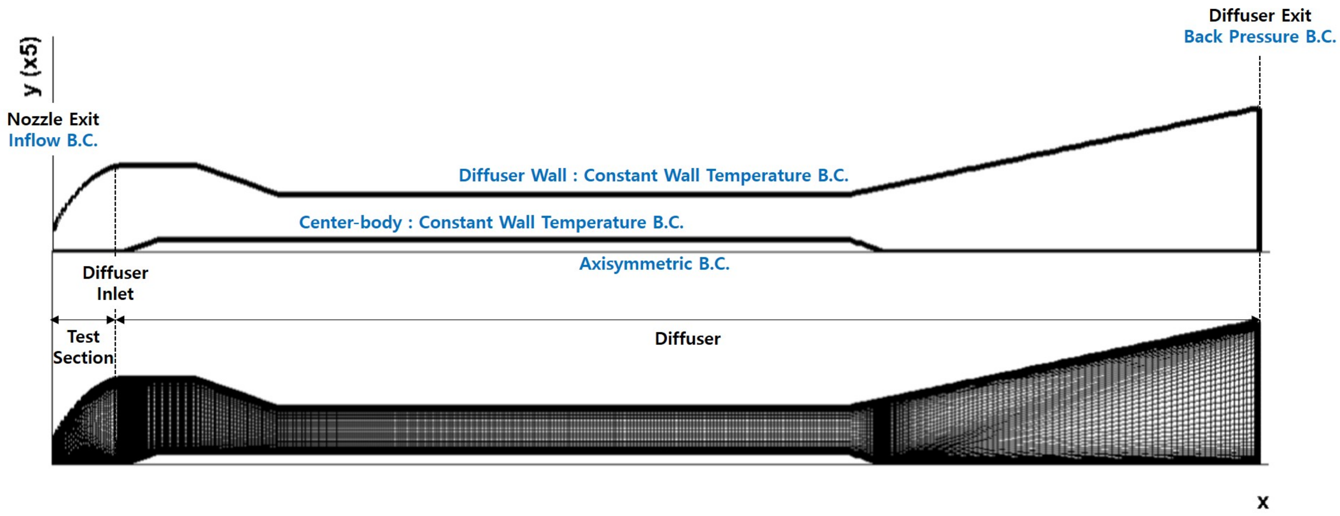

Figure 3.17: Computational domain of the center-body diffuser

B. Results and analysis

For comparison of the two diffusers in the converging section, the static pressure contour and averaged total pressure results are shown in Figure 3.18, and the pressure, Mach number, and temperature along the axis are shown in Figure 3.19. As shown in Figure 3.19c, the Mach number 6 flow expands and accelerates to about Mach number 9 through the test section and enters the diffuser inlet. In the case of the second throat cylindrical diffuser, the hypersonic flow meets the diffuser inlet and generates the first oblique shock wave, and subsequently creates several oblique shocks (a shock train), decelerating and compressing the flow. By contrast, in the case of the center-body diffuser, a double oblique shock wave is generated at the inlet as the accelerated hypersonic flow meets both the diffuser inlet and the center body. Thereafter, a strong shock–shock interaction occurs among generated shock waves, and owing to these multiple shock waves, the deceleration and compression ratios were relatively higher than those of the general second throat diffuser. Especially, as shown in Figure 3.18, most of the total pressure, approximately 97 %, is lost in the converging section of both diffusers, because the strong oblique shock waves are generated by hypersonic flow. In particular, the total pressure loss of the center-body diffuser occurs more larger and rapidly owing to the multiple strong oblique shock waves. Under the same back pressure, the bigger total pressure loss moves the location of the terminal shock wave toward diffuser inlet, and at more higher back pressure, the terminal shock wave can escape from the diffuser making experiment impossible. Therefore, the center-body diffuser with large total pressure loss due to the multiple shock waves at the inlet is disadvantageous in maximum efficiency, which is proven in the performance evaluation of diffusers section.

In the throat of the diffusers, the oblique shock wave generated from the inlet is reflected to the diffuser wall or center-body, generating the shock train, which decreased the flow Mach number and increased the static pressure and temperature as shown in Figure 3.20. In the case of the center-body diffuser, an additional shock wave is generated by the body, and the shock wave generated on the wall is reflected by the center body at a short distance. Thus, it is confirmed that the static pressure and temperature increase rate according to the length are relatively higher than those of the second throat cylindrical diffuser as shown in Figures 3.21a and 3.21b. However, because of the multiple oblique shock waves, the total pressure loss was higher than that of the general second throat diffuser as shown in Figure 3.19. At the same back pressure, due to the higher total pressure loss, the terminal shock wave in the center-body diffuser was generated inside the diffuser throat while the terminal shock of general second throat diffuser was located after the diffuser throat. In addition, when the terminal shock is generated inside the diffuser throat, the supersonic flow is reduced to a subsonic flow, flowing into the diverging section while being slightly expanded and cooled as shown in Figures 3.21a and 3.21c. This is because the boundary layer made effective area smaller along the diffuser throat.

The flow entering the diverging section is typically reduced to a subsonic flow through the terminal shock wave in the diffuser throat. This subsonic flow compressed to a back pressure as it flowed along the diverging angle, and with the same diverging configuration there is no significant difference between the two diffusers. As shown in Figures 3.22 and 3.23, in the diverging section, the total pressure loss is less than that in the converging and throat section of the diffuser, which is supersonic regions, and the total pressure is sustained at the back-pressure level. In addition, as shown in Figure 3.22, when the terminal shock is generated at the throat exit, that is, the diverging section inlet, the adverse pressure gradient near the wall due to the terminal shock becomes severe, causing flow separation, which affects the deceleration and compression at the diverging section.

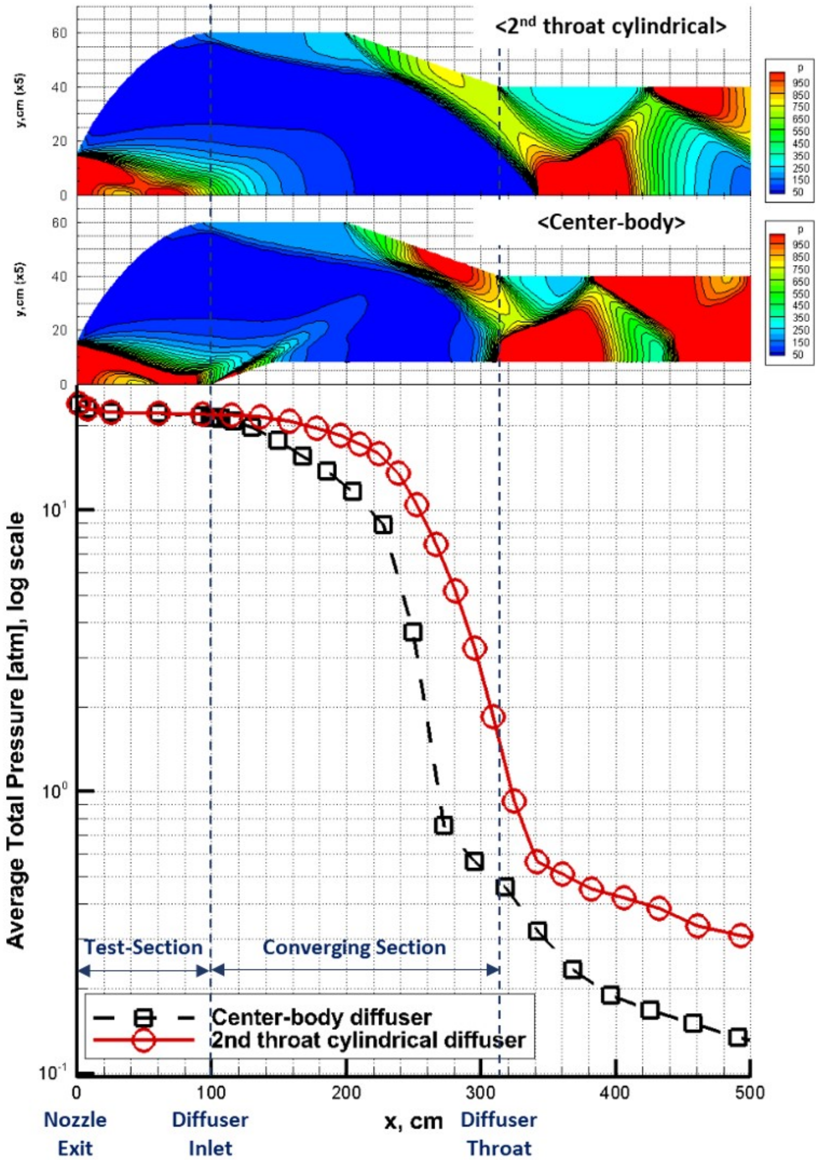

Figure 3.18: Pressure contour and averaged total pressure of converging section

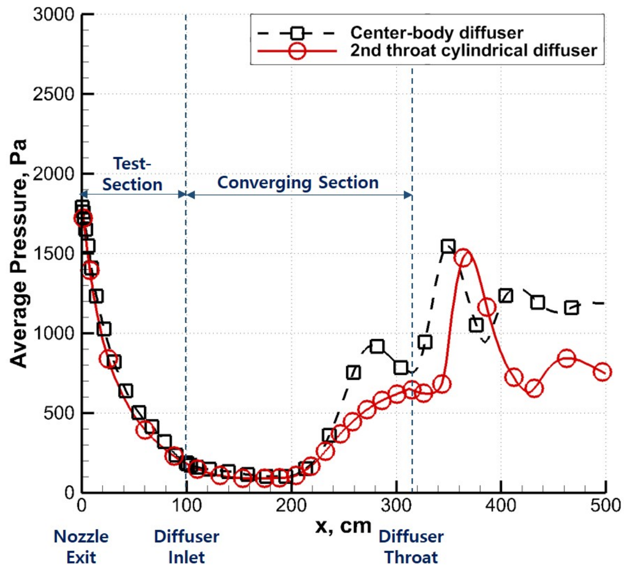

(a) Static pressure

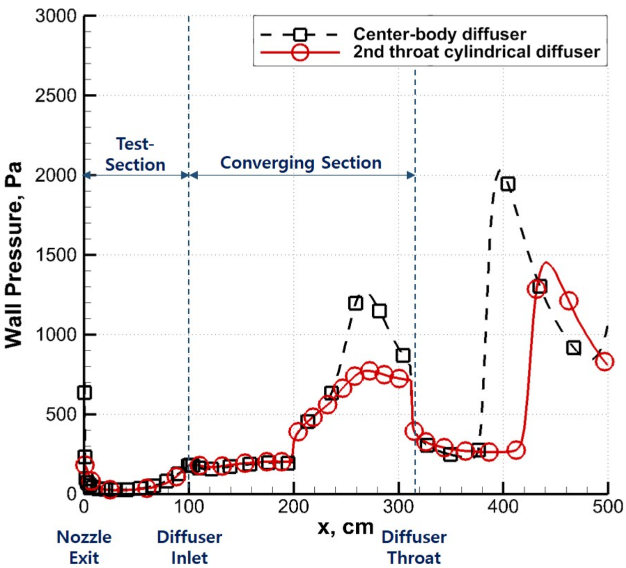

(b) Wall pressure

Figure 3.19: Averaged results along the converging section axis(Cont.)

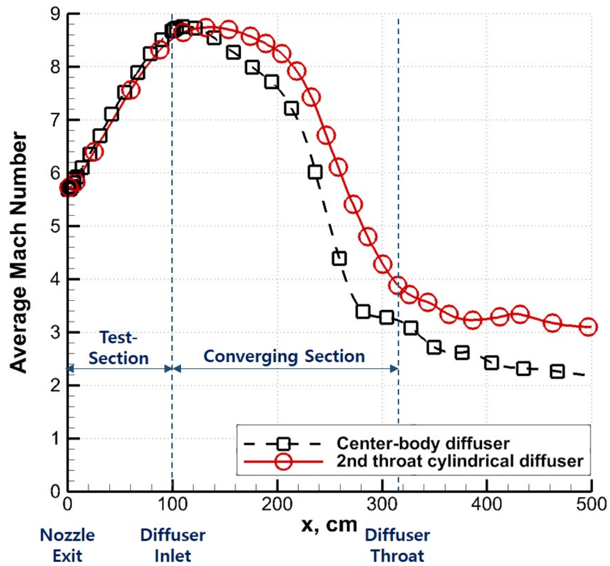

(c) Mach number

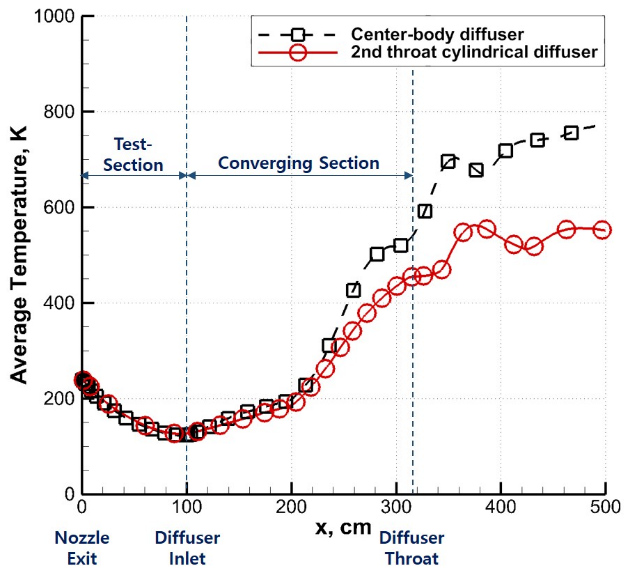

(d) Static temperature

Figure 3.19: Averaged results along the converging section axis

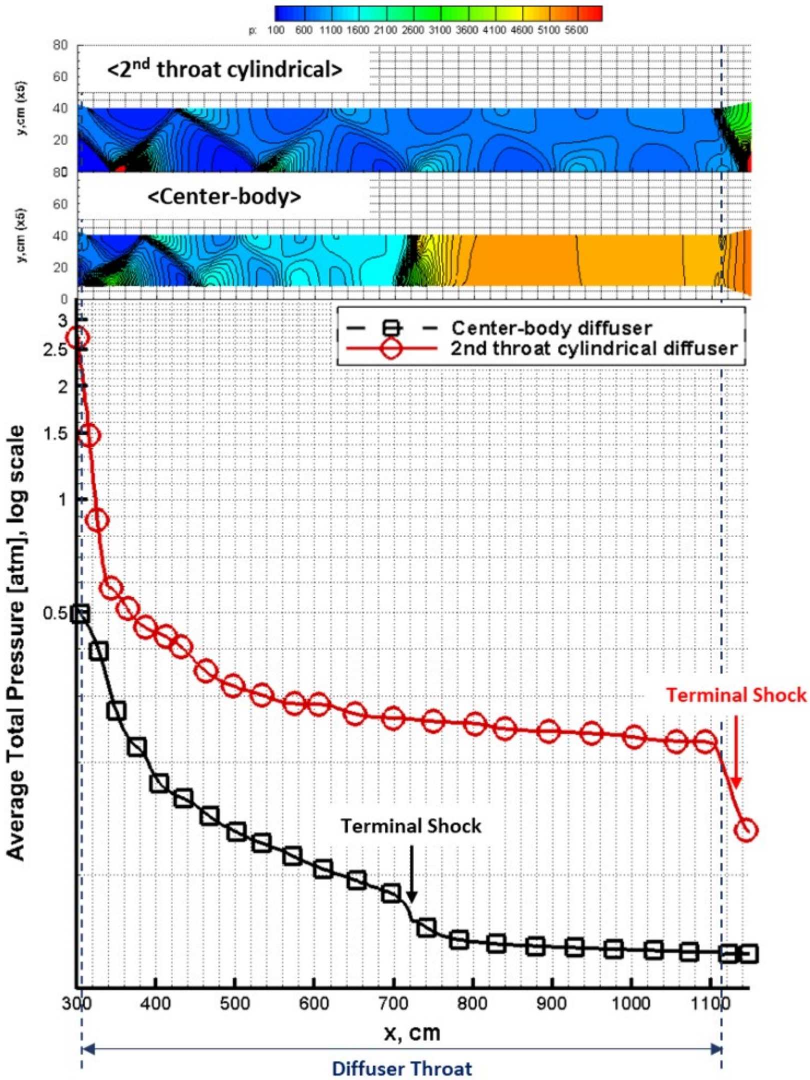

Figure 3.20: Pressure contour and averaged total pressure of throat section

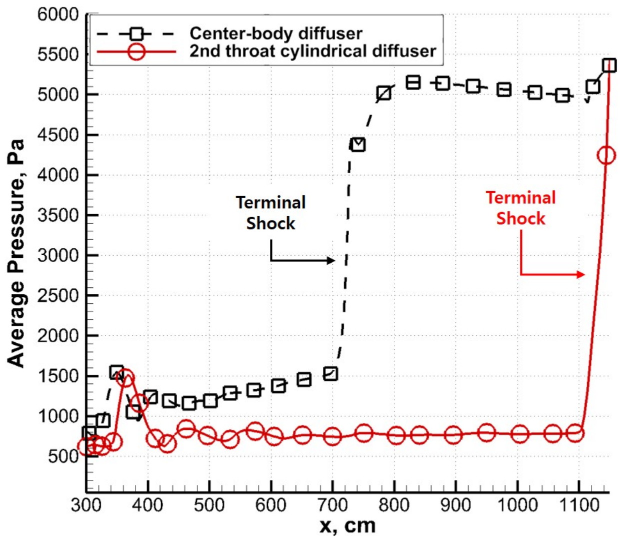

(a) Static pressure

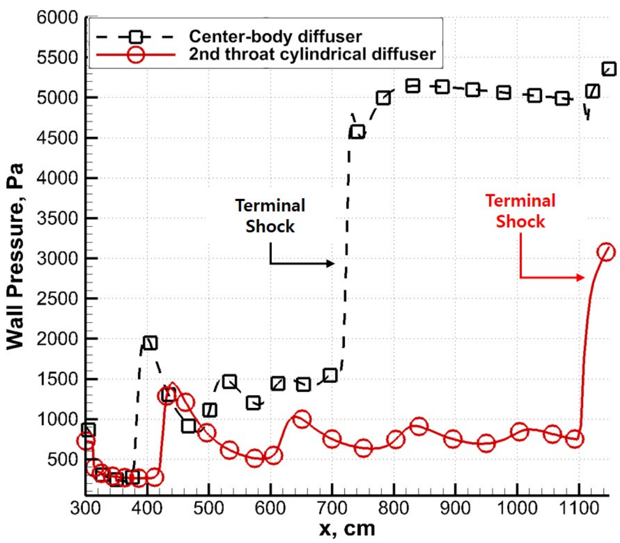

(b) Wall pressure

Figure 3.21: Averaged results along the throat section axis(Cont.)

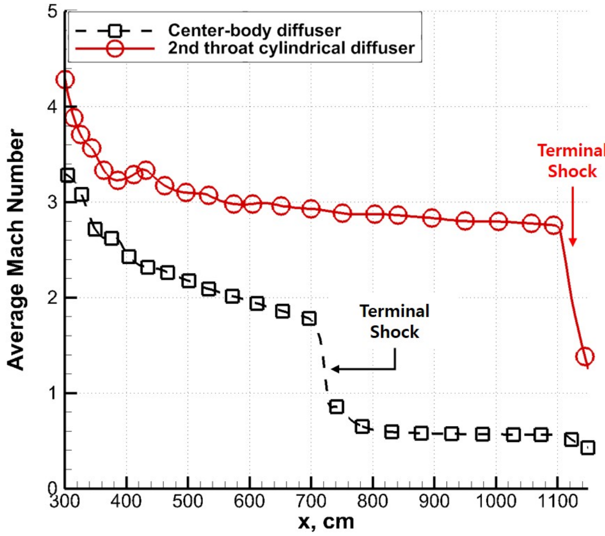

(c) Mach number

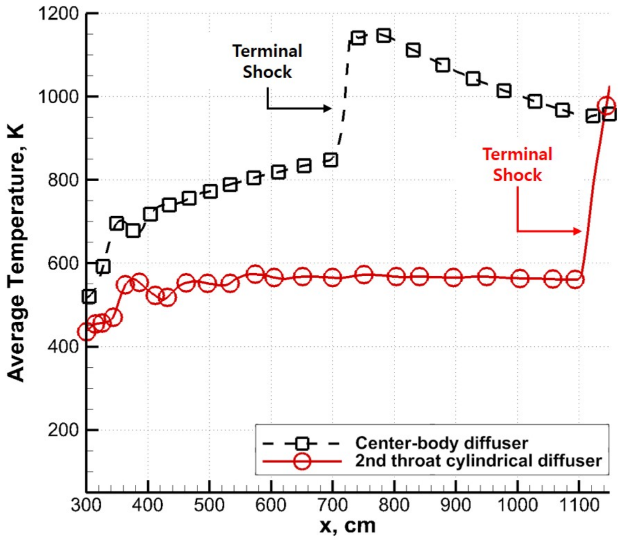

(d) Static temperature

Figure 3.21: Averaged results along the throat section axis

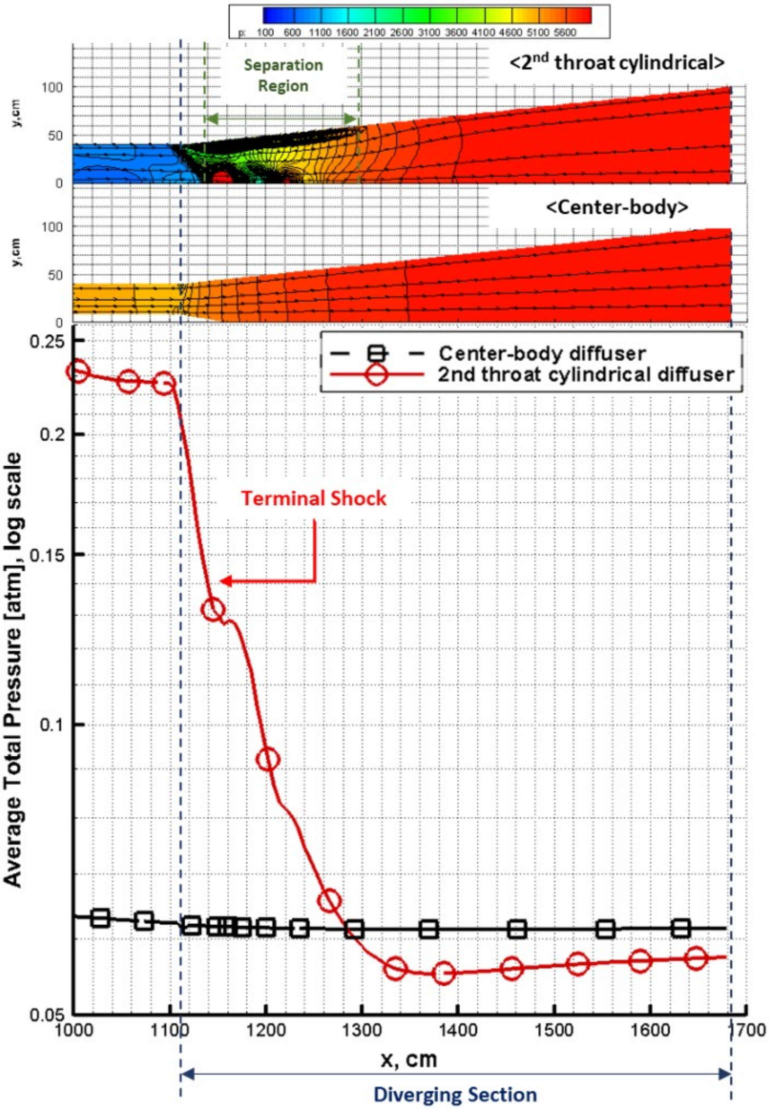

Figure 3.22: Pressure contour and averaged total pressure of diverging section

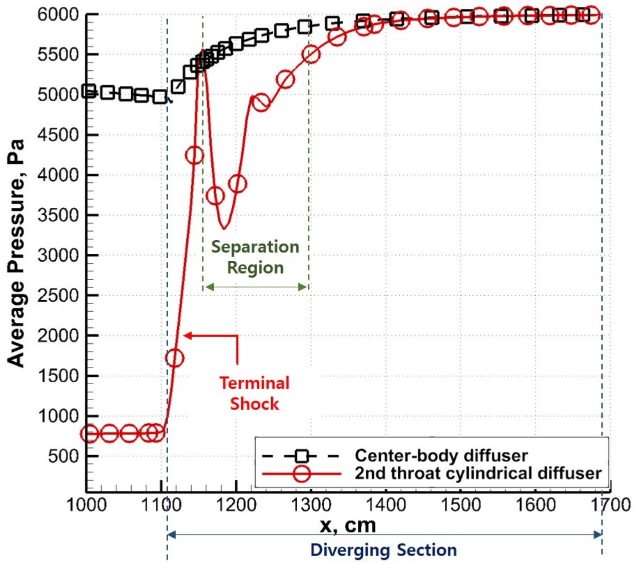

(a) Static pressure

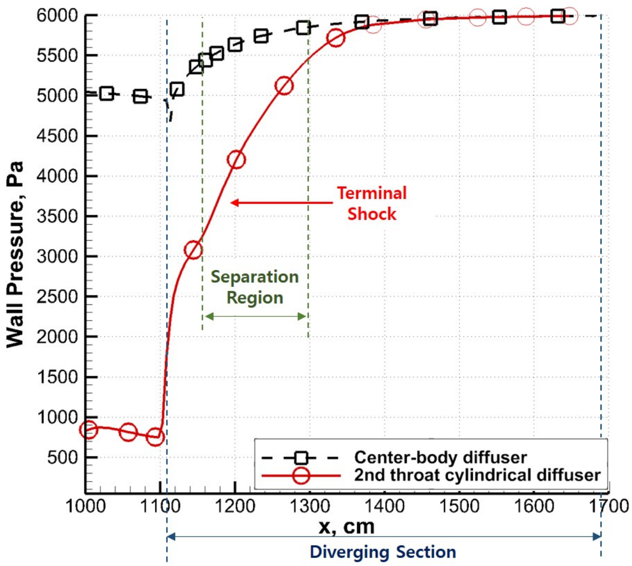

(b) Wall pressure

Figure 3.23: Averaged results along the diverging section axis(Cont.)

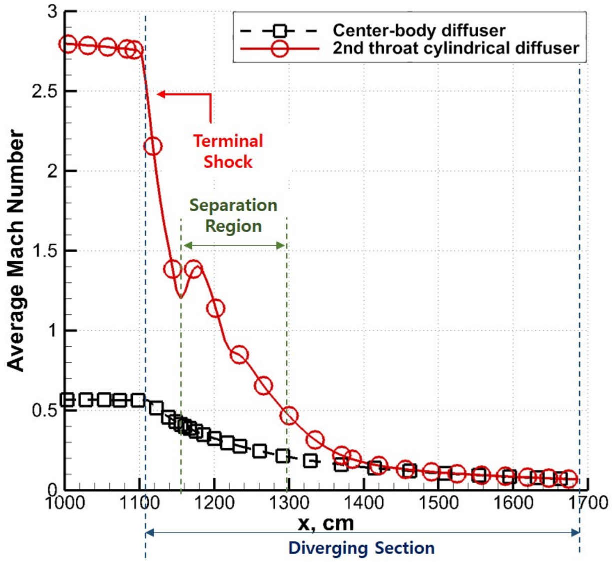

(c) Mach number

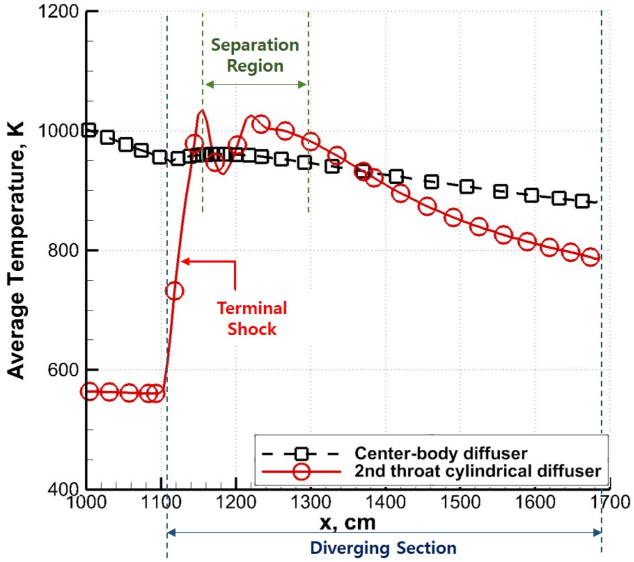

(d) Static temperature

Figure 3.23: Averaged results along the diverging section axis

3.2.2 A novel diffuser

A. Configuration of a novel diffuser

The center-body diffuser uses multiple strong shock waves to increase the static pressure in a short length. However, the total pressure loss due to these shock waves is larger than that of the second throat cylindrical diffuser, as shown in Figure 3.18; thus, the maximum back pressure that can be operated normally is lowered. Therefore, this study proposes a novel diffuser shape, as shown in Figure 3.24. This diffuser locates a center-body in the subsonic region (divergent section) such that there is no total pressure loss due to shock waves. Moreover, this configuration has a wider cooling area than the cylindrical diffuser, thus lowering the flow exit temperature. To compare the diffusers, the center-body was placed in the divergent section of the second throat cylindrical diffuser. The specific configuration of the novel diffuser is summarized in Table 3.7.

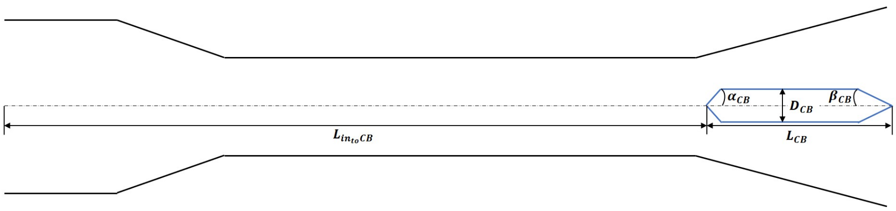

Figure 3.24: Configuration of a novel diffuser

Table 3.7: Specification of the novel diffuser

Center-Body	$L_{\text{in to CB}}$ [m]	11.63
	L_{CB} [m]	5.2
	D_{CB} [m]	0.16
	α_{CB} [$\circ$]	10
	β [$\circ$]	10

B. Results and analysis

The static pressure contour results showing the shock train and terminal shock location according to various back pressures of the novel diffuser are shown in Figure 3.25, and the pressure, temperature, and Mach number along the axis are shown in Figure 3.26. The configuration of the novel diffuser is identical to that of the diffuser shown in Figure 3.16a, except for the center-body in the diverging part. Therefore, the flow structure and variables from the nozzle exit to the throat exit (hypersonic region) are identical to that of the second throat cylindrical diffuser. Moreover, because of the identical shock train, the amount of the total pressure loss is the same, and the range of the operable back pressure and the location of the terminal shock wave exhibit similar patterns.

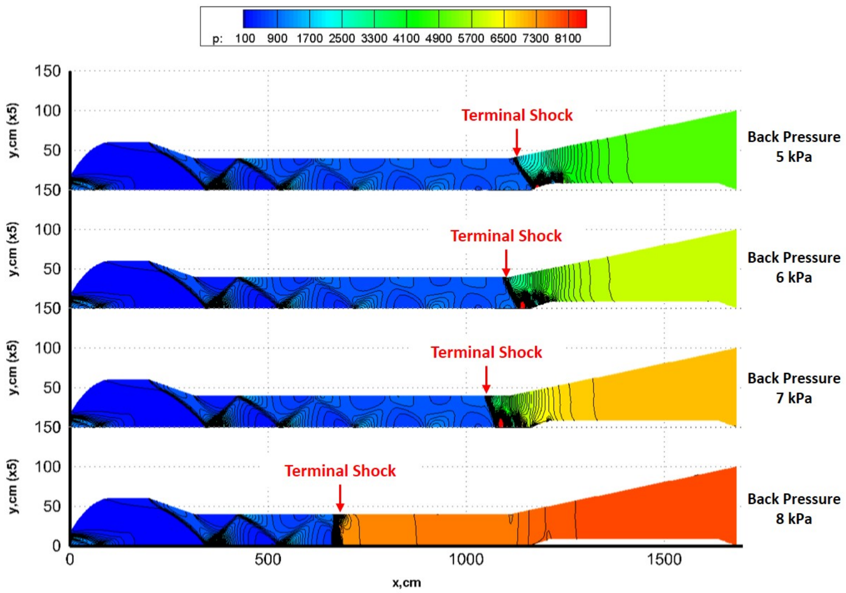

Figure 3.25: Pressure contours of the novel diffuser in various back pressures

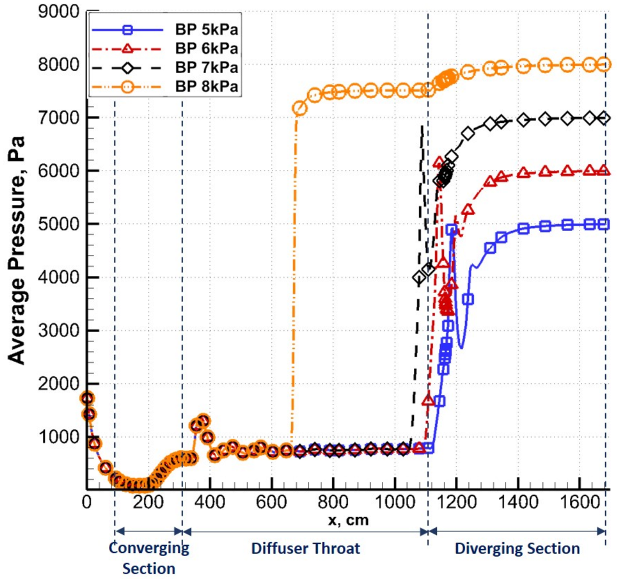

(a) Static pressure

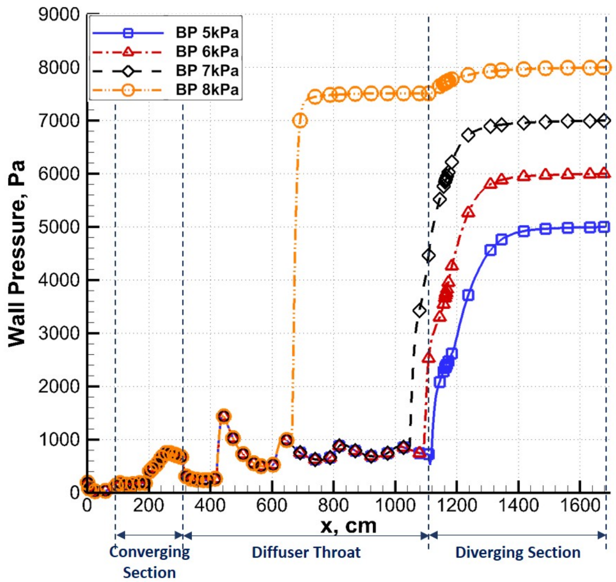

(b) Wall pressure

Figure 3.26: Averaged results along the novel diffuser axis(Cont.)

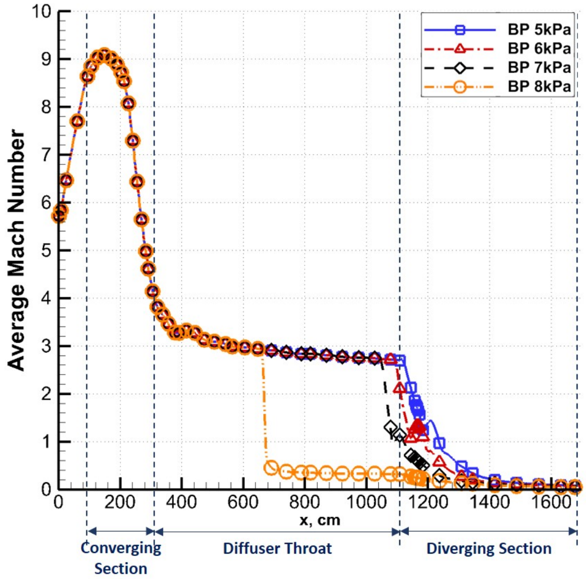

(c) Mach number

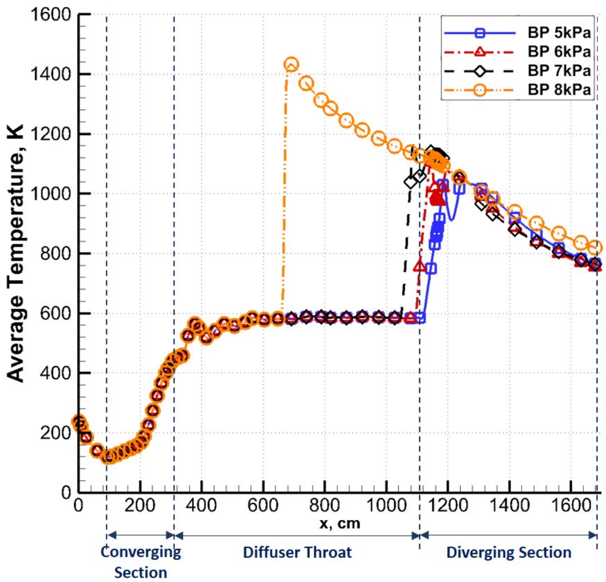

(d) Static temperature

Figure 3.26: Averaged results along the novel diffuser axis

3.2.3 Performance evaluation of diffusers

An efficient diffuser can reduce the test cost by increasing the experiment time and alleviating the vacuum requirements. Generally, the efficiency of a diffuser is evaluated by the diffuser pressure ratio. $[12, 54, 55]$; Therefore, to evaluate the maximum efficiency of each diffuser, the back pressure was varied from 5 kPa ($P_{bp}/P_{nozzle\,exit} = 2.74$) to 8 kPa ($P_{bp}/P_{nozzle\,exit} = 4.4$) with a step size of 1 kPa. In addition, the diffuser exit temperature and enthalpy were used as performance evaluation variables, because a low exit temperature and a low enthalpy are advantageous for reducing the installation and testing costs of the heat exchanger. The diffuser exit velocity and the deceleration rate in the diffuser were also compared as the efficiency of the mechanical device after the diffuser varies depending on the flow velocity.

A. Efficiency

The supersonic or hypersonic diffuser efficiency(η) is given by Equation (3.2). [55]

$$\eta = \frac{DiffuserPressureRatio}{NormalShockPressureRatio} = \frac{P_{0,exit}/P_{0,in}}{P_{02}/P_{01}} \tag{3.2}$$

In the Equation (3.2), P_{01} is the upstream total pressure before the normal shock wave, so it can be assumed to be the same value as the diffuser inlet flow ($P_{o,in}$). The total pressure at the exit($P_{0,exit}$) can be approximated by the back pressure(P_b) because the flow is decelerated to a low Mach number at the diffuser exit. Therefore, Equation (3.2) can be simplified to Equation (3.3). According to Equation (3.3), a diffuser with high efficiency can operate up to a high back pressure (P_b) under the same upstream conditions.

$$\eta = \frac{P_{0,exit}/P_{0,in}}{P_{02}/P_{01}} \approx \frac{P_{0,exit}}{P_{02}} \approx \frac{P_b}{P_{02}} \tag{3.3}$$

In the present study, numerical analysis of the back pressure was performed to compare the efficiency of each diffuser. The wall pressure results for each value of back pressure are shown in Figure 3.27, and the final shock locations are summarized in Table 3.8. The static pressure of the center-body diffuser increased in a relatively shorter length as compared to the other diffusers (Figure 3.27). However, the center-body diffuser generated a strong shock wave, which caused a large total pressure loss. As a result, when the back pressure exceeded 7 kPa, the final shock wave emerged from the diffuser throat as summarized in the Table 3.8. This shock wave affected the experimental flow, such as the pressure and Mach number inside the test section (see the Figure 3.27d), making it impossible to operate the wind tunnel. By contrast, the second throat cylindrical diffuser and the proposed diffuser generated the final shock wave in the diffuser throat even at a back pressure of 8 kPa or higher, indicating that they could be operated at a higher back pressure. Finally, when the flow with an average Mach number of 9.1 entered the diffuser inlet, the maximum efficiency of the center-body diffuser was 0.43, whereas the maximum efficiency of the second throat diffuser and the proposed diffuser was 0.65.

Table 3.8: Location of the final shock wave

Back Pressure	Final Shock Location Written in L/D of Diffuser (Diffuser Throat Start L/D=2.7)		
	Center-body Diffuser	Cylindrical Diffuser	Proposed Diffuser
5 kPa	12.0	12.6	12.6
6 kPa	7.7	12.4	12.4
7 kPa	3.4	11.8	11.8
8 kPa	Not operable	7.2	7.1

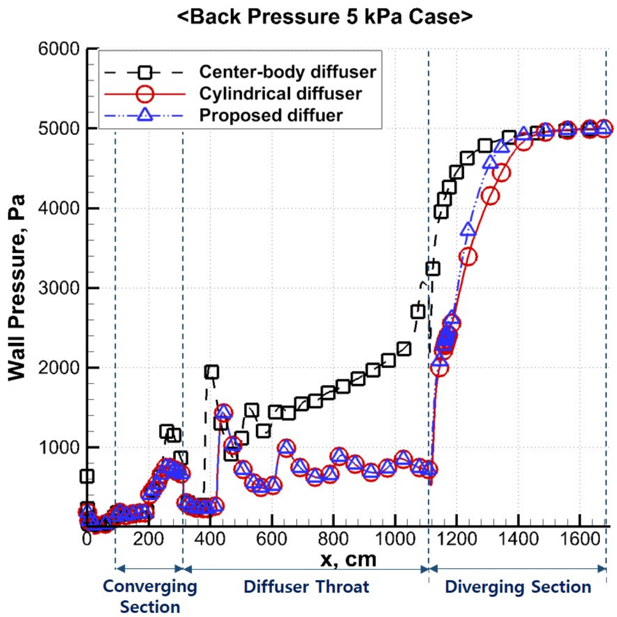

(a) Back pressure 5 kPa

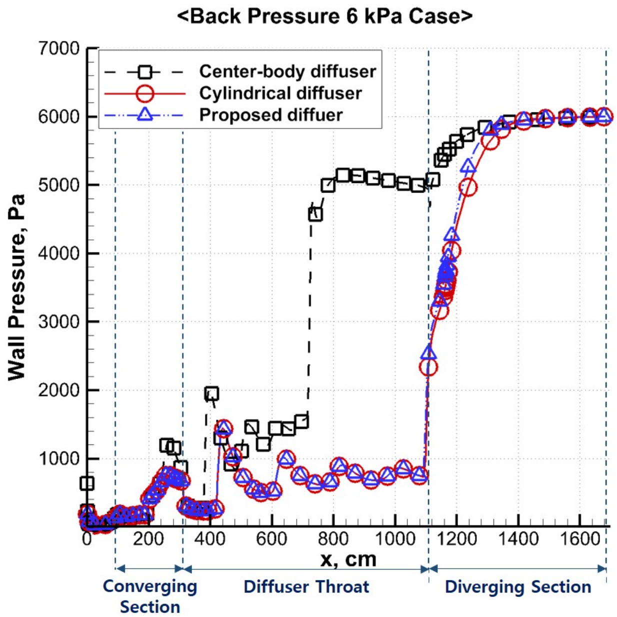

(b) Back pressure 6 kPa

Figure 3.27: Averaged wall pressure of diffusers in various back pressure(Cont.)

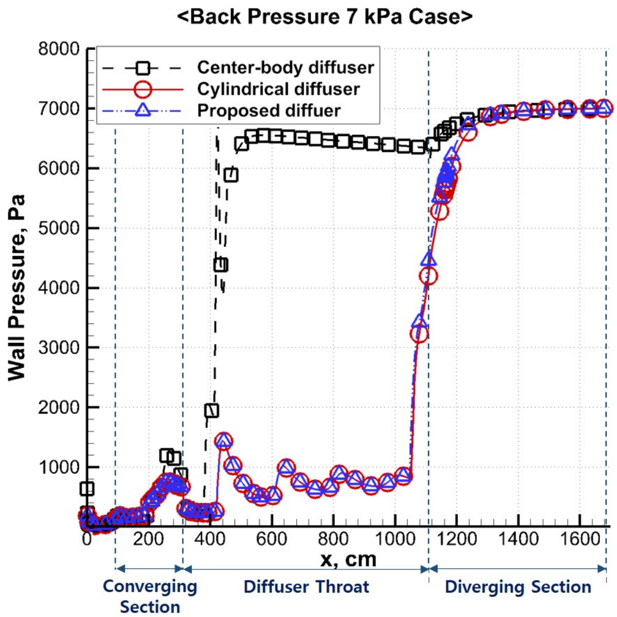

(c) Back pressure 7 kPa

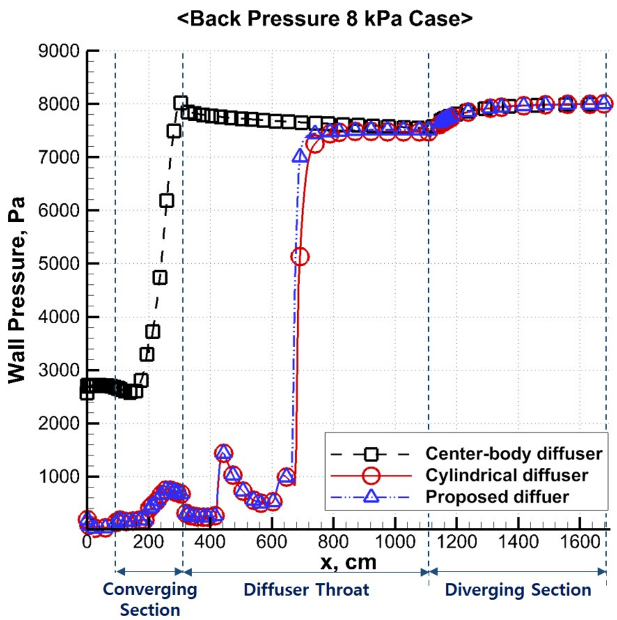

(d) Back pressure 8 kPa

Figure 3.27: Averaged wall pressure of diffusers in various back pressure

B. Temperature and enthalpy

The results of the average temperature along the axis are shown in Figure 3.28. In all types of diffusers, the flow temperature is increased by the shock train and final shock wave; after the final shock wave, the temperature showed a tendency to decrease due to the cooling effect of the diffuser wall and center-body. In the case of the center-body diffuser, the temperature increasement due to the shock train is higher than that of the other two diffusers as the center-body diffuser has a short oblique shock reflection distance and strong oblique shock waves. Meanwhile, the flow temperature in the second throat cylindrical diffuser and the proposed diffuser increased mostly due to the final shock wave; then, the temperature decreased owing to the cooling effect of the diffuser wall. In particular, in the divergent part of the proposed diffuser, the flow was further cooled by the center-body and the temperature was relatively less than that of the second throat cylindrical diffuser.

Moreover, the average temperature and enthalpy at the diffuser exit in all cases are shown in Figure 3.29. Generally, the higher the back pressure, the stronger the terminal shock wave is generated, and the temperature after the shock wave increases with the back pressure as shown in the temperature results of the second throat diffuser and the proposed diffuser. On the other hand, in the center-body diffuser, the exit temperature and enthalpy tended to decrease as the back pressure increased. This is because as the back pressure is higher in the center-body diffuser, the terminal shock wave moves to the front part of the diffuser, and the increased flow temperature and enthalpy due to the shock wave receive a larger area of cooling effect by both the center-body and diffuser wall. The exit temperature and enthalpy for the proposed diffuser were low in all cases as compared with the second throat diffuser, and both the temperature and enthalpy difference between the two diffusers increased as the back pressure increased. For back pressures of 5 and 6 kPa, the terminal shock wave was located in the divergent part; thus, the cooling length at the center-body of the proposed type diffuser was shortened. As a result, the temperature and enthalpy difference compared to the second throat diffuser was only 3 and 8 % for back pressures of 5 and 6 kPa, respectively. However, for back pressures of 7 and 8 kPa, where the terminal shock wave was generated inside the diffuser throat, the exit temperature and enthalpy difference were 11 %, showing almost the same value in each case.

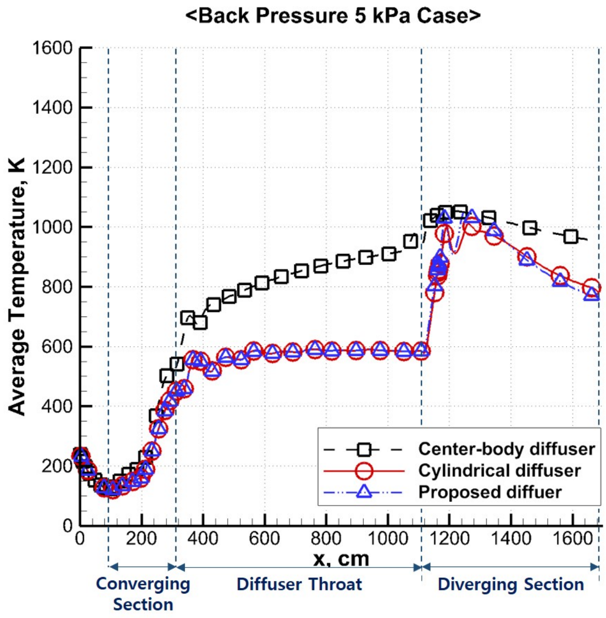

(a) Back pressure 5 kPa

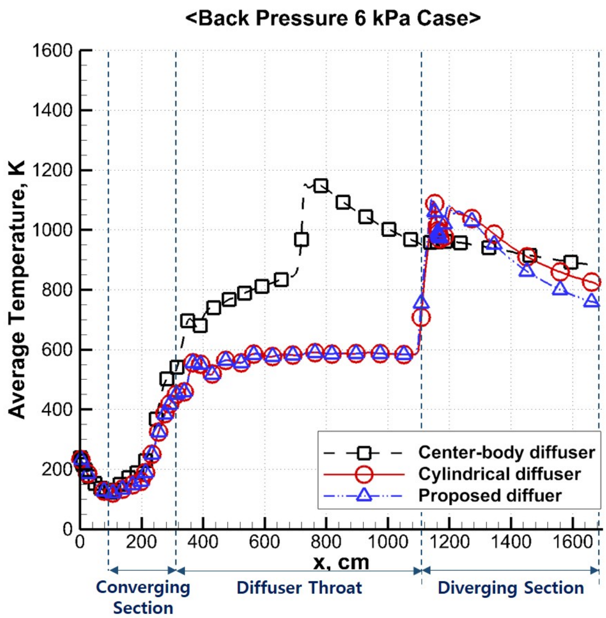

(b) Back pressure 6 kPa

Figure 3.28: Averaged temperature of diffusers in various back pressure(Cont.)

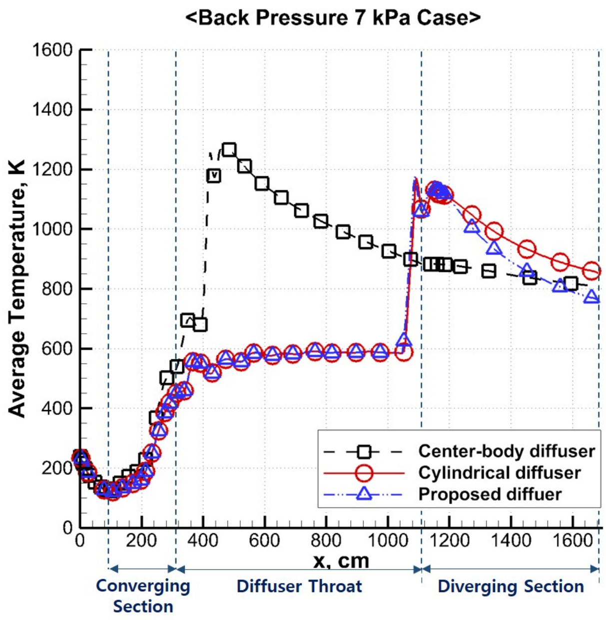

(c) Back pressure 7 kPa

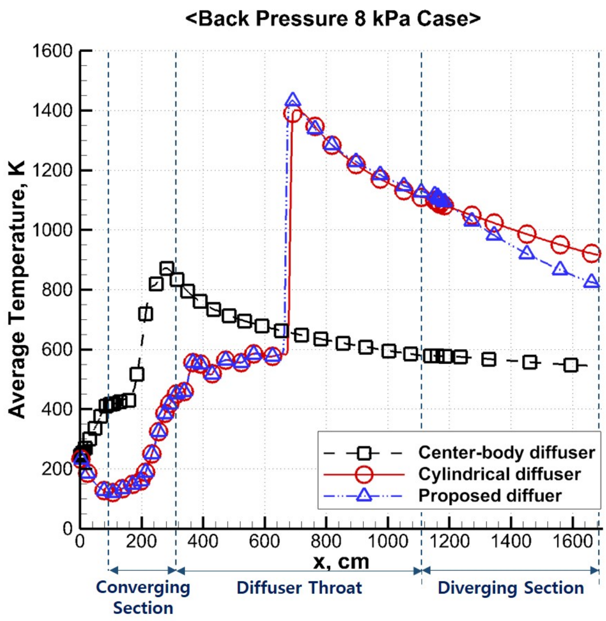

(d) Back pressure 8 kPa

Figure 3.28: Averaged temperature of diffusers in various back pressure

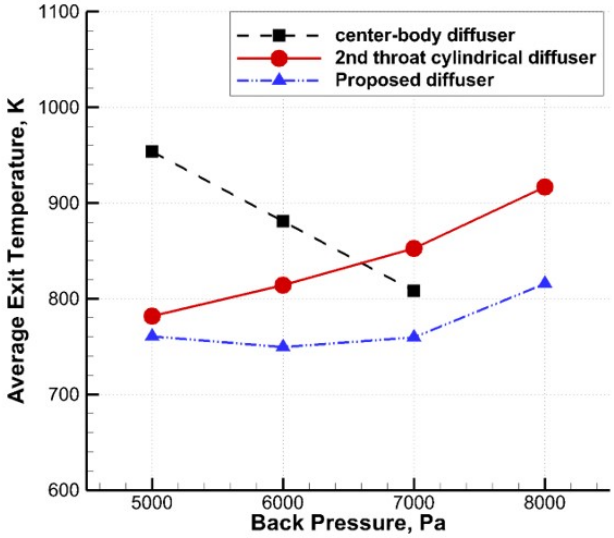

(a) Averaged exit temperature

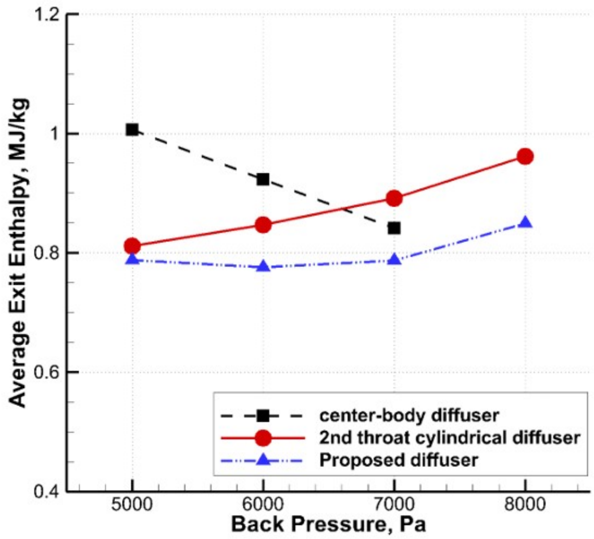

(b) Averaged exit enthalpy

Figure 3.29: Exit temperature and enthalpy of diffusers in various back pressure

C. Exit velocity

The averaged exit velocity and the deceleration rate in the diverging section of each case are shown in Figure 3.30. The deceleration rate in the diverging section was calculated using the diverging section inlet and exit velocity. Except in the case a with back pressure of 8 kPa for which the center-body diffuser was not operable, the deceleration rate in the diverging section was lowest for the center-body diffuser, followed by the second throat cylindrical diffuser and then the proposed diffuser at each value of back pressure. In the same diverging configuration, the deceleration rate of the center-body diffuser was small because the flow passed through a strong shock wave in front of the diffuser and flowed into the diverging section with the total pressure already reduced to the back-pressure level. At each value of back pressure, the exit velocity and the deceleration rate of the proposed and second throat cylindrical diffuser were almost the same, but the deceleration rate of the proposed type diffuser was slightly larger. This is because the flow temperature decreased due to the additional cooling effect by the center-body at the same mass flow rate and back pressure. Another reason could be the total pressure loss due to the friction of the center-body.

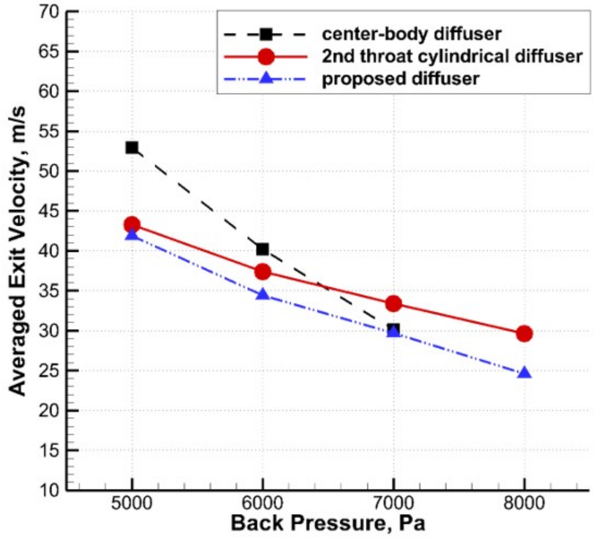

(a) Averaged exit temperature

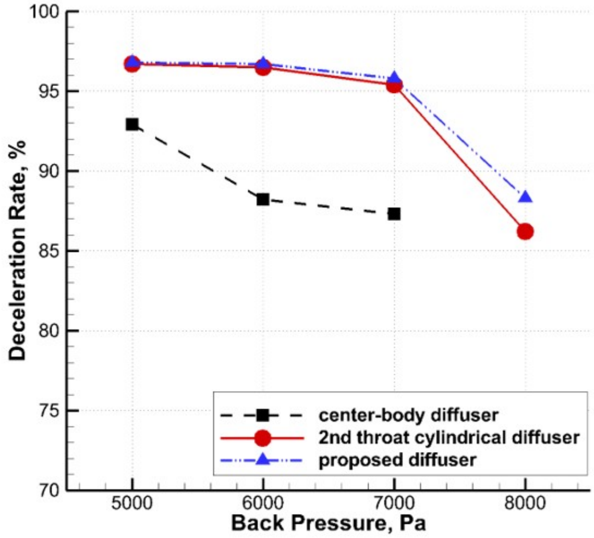

(b) Averaged exit enthalpy

Figure 3.30: Exit velocity and deceleration rate of diffusers in various back pressure

CHAPTER 4. PREDICTING CORRELATION USING MULTI-LAYER PERCEPTRON

There are two methods for designing and predicting the performance of a segmented type arc-heater: scaling study and CFD analysis. [11] The scaling study is useful for initial sizing by calculating the chamber pressure (P_0), mass averaged enthalpy (h), efficiency (η), and arc-voltage (V) of the arc-heater in a short time using the equations of Equation (4.1) $\sim$ (4.4).

$$p_0 = 935(\frac{m}{A^*})I^{0.1667} \tag{4.1}$$

$$h = (0.293A^*\frac{P_0}{\dot{m}})^{2.5} = (1.242 \times 10^6)I^{0.4167} \tag{4.2}$$

$$\eta = 52.7\dot{m}^{0.28}(\frac{I}{D})^{-0.25}(\frac{L}{D})^{-0.4} \tag{4.3}$$

$$V = (2.358 \times 10^4)\dot{m}^{0.72}I^{-0.3333}L^{0.4}D^{-0.65} \tag{4.4}$$

However, the scaling study has limitations applied only to low power arc-heaters, and the enthalpy of the actual heater is not a function of current only, but a function of current and mass flow rate, so the accuracy of enthalpy prediction is low. Arc-heater sizing and performance prediction using CFD analysis has higher accuracy, but requires a high-performance computation machine and takes more time than scaling study. Therefore, in order to overcome the limitations of design and performance prediction using scaling study and CFD analysis, this study introduces a method that is time-efficient and has similar accuracy as CFD results.

The multi-layered perceptron (MLP) model that can predict a correlation between parameters of a segmented type arc-heater is used. A code based on python [56] was developed, and predicting correlation between parameters for the performance prediction of the arc-heated wind tunnel proceeds in the following order.

1. Database building

   Select major configuration variables, flow conditions, and performance predictors for each component or the entire system of the arc-heated wind tunnel. Afterward, the results using the experimental values or CFD analysis are built into a database.

2. Deep learning using an artificial neural network model

   After performing deep learning on data using an artificial neural network model with a database as an input, a performance prediction model is derived.

3. Performance prediction using the model

   The configuration variables and flow conditions of the arc-heated wind tunnel are used as inputs, and the performance predictor variables are the outputs.

4.1 Multi-Layered Perceptron (MLP)

Multi-layered perceptron (MLP) was used as the artificial neural network model. [57] MLP is a model composed of several perceptrons stacked in layers. A perceptron is the basic unit of an artificial neural network. It calculates the weight sum of the bias and input, and it derives the result by applying a step function. There is a limitation that only linear classification is possible, and to overcome this, the concept of MLP was introduced. In the present study, an artificial neural network including forward propagation and backpropagation was used, and its outline is shown in Figure 4.1.

Four hidden layers were used, and in the input layer, values necessary for performance prediction, such as arc-heated wind tunnel configuration variables, operating conditions, and CFD analysis results, can be entered.

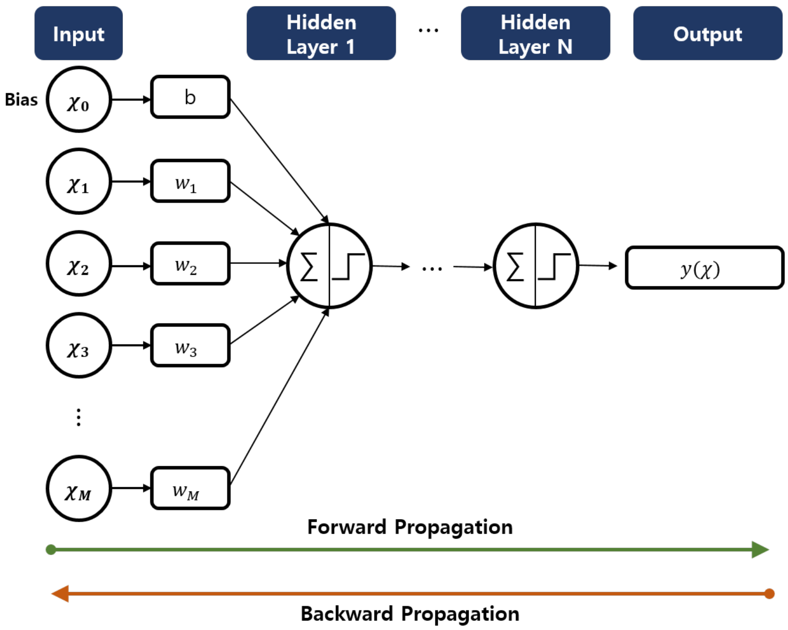

Figure 4.1: Outline of the multi-layered perceptron

The activation function determines whether the total sum exceeds the threshold value by multiplying the weight by the input value. The ReLU function (Figure 4.2) [58] was used in this study.

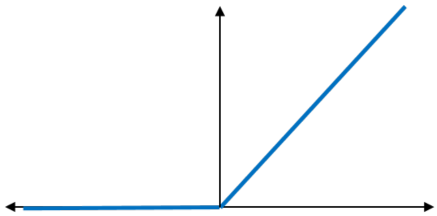

$$f(x) = \max(0, x)$$

Figure 4.2: ReLU function

As the loss function, a mean square error (MSE) regression model was used. MSE is the average of the squared errors, and its definition is as in Equation (4.5).

$$E = \sum (\hat{y}_i - y_i)^2 \tag{4.5}$$

The optimizer minimizes the loss function by optimizing the weight values in order to increase the accuracy of the output. In the present study, the adaptive moment estimation (Adam) algorithm was used as the optimizer. Adam is an algorithm that combines the momentum optimization method and the root mean square propagation (RMSprop) method, and its calculation method and outline are shown in Figure 4.3.

If the weights of all hidden layers are the same or have symmetrical weight values, the weights are not updated during the back-propagation process. Therefore, a weight initialization method is required in the MLP model, and in the present study, weight initialization was performed using the initialization proposed by Xavier. [59] This method is an initialization method based on variance adjustment, and initializes weights using values extracted based on a probability distribution.

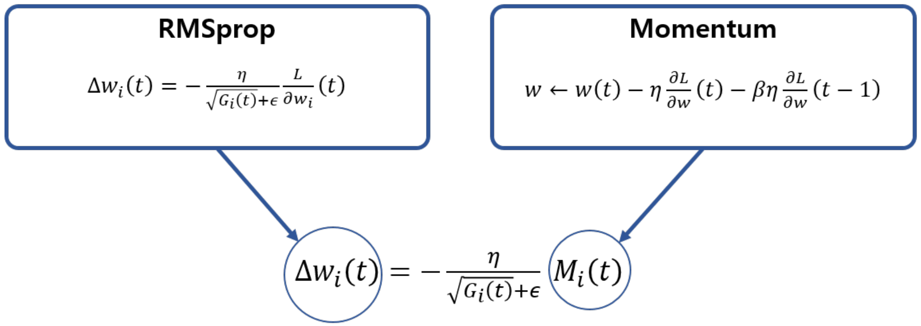

$M_i(t) = \beta M_i(t-1) + (1-\beta)\frac{\partial L}{\partial w_i}(t)$

$M_i(0) = 0$

Figure 4.3: Overview and calculation method of Adam

4.2 Predicting Correlation between Arc-Heater Parameters

The multi-layered perceptron (MLP) model is used to predict correlations between segmented-type arc-heater parameters. The prediction results are compared with the experimental values of existing segmented type arc-heaters to validate the database and MLP model.

4.2.1 Database building

According to the scaling study [14, 47] and the parametric study [45] of the segmented arc-heater, the main design parameters are the constrictor length, constrictor diameter, and nozzle throat diameter, and the main operating conditions are the current and the mass flow rate. The performance variables of the arc-heater are the pressure, voltage, mass averaged enthalpy at the nozzle throat, and efficiency. Among these variables, the heater chamber pressure is almost independent of the heater length and diameter because it is determined by the mass flow rate and the nozzle throat diameter rather than the configuration parameters of the heater. Therefore, after performing the CFD analysis of the arc-heater for various design parameters and operating conditions, two databases for MLP training are created by organizing the results of the pressure and the other three performance variables. The values for building databases are summarized in Table 4.1.

Totally, 6,400 data were extracted by performing CFD analysis using eight different heaters with 800 operating variables (20 of current, 40 of mass flow rate).

The database for pressure prediction is separately constructed containing nozzle throat diameter, current, mass flow rate, and pressure, excluding heater configuration variables and other three performance variables. Another database for predicting arc-voltage, enthalpy, and efficiency includes all configuration information and performance analysis results. The databases are built in the form of comma-separated variables (.CSV), and a part of the database is shown in Figure 4.5.

Table 4.1: Input parameters and values for MLP training

	Input Parameters	Values
Configuration Variables	Constrictor Length, cm	$10 \sim 390$
	Constrictor Diameter, cm	$2 \sim 8$
	Nozzle Throat Diameter, cm	$0.5 \sim 6$
Operating Variables	Current, A	$150 \sim 6{,}000$
	Mass flow rate, g/s	$10 \sim 800$
Arc-Heater Performance Variables	Pressure, atm	$0.5 \sim 100$
	Arc-voltage, V	$700 \sim 6{,}200$
	Mass averaged enthalpy, MJ/kg	$3.7 \sim 30$
	Efficiency	$0.2 \sim 0.6$

Nozzle Throat D	Mass Flow Rate	Current	P
1	200	500	56.96987
1	70	1000	24.099912
1	100	1000	33.902791
1	200	1000	50.004639
1	200	1000	65.520235
2	100	500	7.3115903
2	200	500	13.833146
2	300	500	20.118491
2	400	500	26.333553
2	500	500	32.458184
2	600	500	38.545759
2	700	500	44.593942
2	800	500	50.570698
2	100	1000	8.1919331
2	200	1000	15.86986
2	300	1000	23.200062
2	400	1000	30.295426
2	500	1000	37.195621
2	600	1000	43.977098
2	700	1000	50.704602
2	800	1000	57.300599
3	100	500	3.0730651
3	200	500	5.8252382

(a) Database for pressure prediction

Figure 4.4: Database of segmented arc-heaters(Cont.)

Constrictor D	Constrictor L	Constrictor L/D	Nozzle Throat D	Mass Flow Rate	Current	P	V	H	E
2.37	43.18	18.21940928	1	120	2000	45.1272	2419.967	20.20508	0.445986
2.37	43.18	18.21940928	1	150	2000	55.9752	2718.341	19.53427	0.482618
2.37	43.18	18.21940928	2	45	2000	4.225759	1454.268	25.58843	0.369297
2.37	43.18	18.21940928	2	70	2000	6.465384	1821.402	23.78206	0.424444
2.37	43.18	18.21940928	2	100	2000	9.098077	2197.641	22.26854	0.468557
2.37	43.18	18.21940928	2	150	2000	13.41903	2714.342	20.72915	0.53804
2.37	43.18	18.21940928	2	200	2000	17.68829	3194.756	19.70246	0.580677
2.37	43.18	18.21940928	2	300	2000	26.07036	4076.082	18.30954	0.639132
2.37	43.18	18.21940928	3	45	2000	1.763538	1454.301	26.1378	0.39571
2.37	43.18	18.21940928	3	70	2000	2.69882	1823.297	24.17905	0.453633
2.37	43.18	18.21940928	3	100	2000	3.789513	2207.363	22.53671	0.509731
2.37	43.18	18.21940928	3	150	2000	5.572122	2764.206	20.76612	0.559055
2.37	43.18	18.21940928	3	200	2000	7.322846	3254.842	19.61016	0.587665
2.37	43.18	18.21940928	3	300	2000	10.76257	4151.787	18.11129	0.649195
2.37	23.7	10	1	45	500	13.84853	1673.607	12.03947	0.576681
2.37	43.18	18.21940928	1	45	500	14.06403	2115.509	12.84256	0.478162
2.37	47.4	20	1	45	500	14.61012	2270.298	12.91643	0.456574
2.37	71.1	30	1	45	500	15.08118	2863.802	13.31869	0.378263
2.37	94.8	40	1	45	500	15.36984	3439.93	13.54113	0.321267
2.37	23.7	10	1	45	2000	17.14494	1183.821	22.3413	0.367936
2.37	47.4	20	1	45	2000	17.37441	1641.001	22.93448	0.273515
2.37	71.1	30	1	45	2000	17.50249	2096.089	23.23338	0.217903
2.37	94.8	40	1	45	2000	17.58458	2553.723	23.4052	0.181087
2.37	23.7	10	1	70	2000	26.29666	1447.292	20.95702	0.445278
2.37	47.4	20	1	70	2000	26.81699	1979.419	21.8723	0.34534
2.37	71.1	30	1	70	2000	27.10266	2489.583	22.35144	0.281952
2.37	94.8	40	1	70	2000	27.28486	2988.101	22.63072	0.238428
2.37	23.7	10	1	100	2000	36.89067	1724.02	19.74263	0.505884
2.37	47.4	20	1	100	2000	37.97329	2331.925	20.90062	0.401754
2.37	71.1	30	1	100	2000	38.50186	2899.794	21.52354	0.333399
2.37	94.8	40	1	100	2000	38.82562	3473.514	21.8952	0.284394
7.11	127.98	18	3	100	2000	3.646107	1718.247	21.88679	0.585127

(a) Database for arc-voltage, enthalpy, and efficiency prediction

Figure 4.5: Database of segmented arc-heaters

4.2.2 MLP training information

Using the database, MLP training is performed for the pressure and other performance variables such as arc-voltage, mass-averaged enthalpy, and efficiency. Training information, such as epoch, batch size, learning rate, etc., are summarized in Table 4.2 and Table 4.3, respectively.

Table 4.2: MLP training information for pressure prediction

Epoch	Batch Size	Learning Rate	Number of Hidden Layers
300	32	0.005	5

Number of Nodes	Training Time	Mean Square Error
127,69,38,30,27	25 minutes	1.40E-06

Table 4.3: MLP training information for other performance parameters

Epoch	Batch Size	Learning Rate	Number of Hidden Layers
300	512	0.005	6

Number of Nodes	Training Time	Mean Square Error
104,87,73,54,28,27	30 minutes	1.60E-05

4.2.3 Performance prediction

The predicted performance parameters using the trained model are compared with the experimental and the scaling study values of existing segmented arc-heaters in various sizes. The values of the JAXA 0.75 MW heater [44] as a small arc heater, the AEDC 5 MW heater [60] as a medium heater, and a NASA 60 MW IHF heater [17] as a large heater were used. The results and errors are summarized in Table 4.4 to Table 4.9, respectively. The averaged error of the performance prediction for each device is shown: in the case of the JAXA 0.75 MW heater, the pressure was 7.1 %, the voltage was 8.0 %, the enthalpy was 2.7 %, and the efficiency was 2.1 % compared to the experimental value. In the case of AEDC's 5 MW heater, the pressure was 3.0 %, the voltage was 13.8 %, the enthalpy was 6.0 %, and the efficiency was 6.4 %. NASA's IHF heater showed an error range of 4.2 % for pressure, 3.5 % for voltage, 4.9 % for enthalpy, and 4.0 % for efficiency. In addition, averaged errors are compared and summarized in Table 4.10. In the case of high-power and high-pressure heaters, the MLP prediction results are more accurate than the scaling study. Prediction using the MLP model is more accurate because the database includes the range (high power and high pressure) that the scaling study cannot predict. Also, it is proved that segmented arc-heater prediction is possible with the small data size.

Table 4.4: Comparing JAXA 0.75 MW heater results (Pressure)

Case	Experimental Results	Scaling Study		MLP Prediction	
	[atm]	P[atm]	Error[%]	P[atm]	Error[%]
1	0.516	0.486	5.8	0.613	18.8
2	0.600	0.584	2.7	0.681	13.4
3	0.692	0.681	1.6	0.748	8.0
4	0.775	0.778	0.5	0.819	5.7
5	0.862	0.876	1.6	0.891	3.4
6	0.953	0.973	2.1	0.963	1.0
7	0.563	0.530	6.0	0.624	10.8
8	0.651	0.636	2.3	0.684	5.2
9	0.747	0.742	0.7	0.760	1.8
10	0.846	0.848	0.2	0.836	1.1
11	0.947	0.953	0.7	0.912	3.6
12	1.047	1.059	1.2	0.988	5.6
13	0.590	0.560	5.0	0.706	19.8
14	0.682	0.672	1.5	0.766	12.2
15	0.792	0.784	1.0	0.828	4.5
16	0.886	0.896	1.2	0.890	0.5
17	0.996	1.008	1.2	0.952	4.4
18	1.105	1.121	1.4	1.015	8.2
		Avg.	2.0	Avg.	7.1

Table 4.5: Comparing AEDC 5 MW heater results (Pressure)

Case	Experimental Results [atm]	Scaling Study P[atm]	Scaling Study Error[%]	MLP Prediction P[atm]	MLP Prediction Error[%]
1	26.30	27.49	4.5	25.41	3.4
2	26.00	28.05	7.9	25.35	2.5
3	26.20	28.08	7.2	25.95	0.9
4	53.20	59.07	11.0	51.06	4.0
5	51.00	57.13	12.0	49.56	2.8
6	53.70	58.94	9.8	50.98	5.1
7	77.60	92.11	18.7	78.54	1.2
8	84.40	97.16	15.1	81.76	3.1
9	102.00	133.13	30.5	101.98	0.0
10	64.00	70.20	9.7	60.25	5.9
11	46.00	56.13	22.0	48.56	5.6
12	52.90	61.91	17.0	53.40	1.0
13	43.90	51.66	17.7	44.92	2.3
14	55.40	60.06	8.4	51.86	6.4
15	101.50	127.76	25.9	100.55	0.9
		Avg.	14.5	Avg.	3.0

Table 4.6: Comparing NASA 60 MW IHF heater results (Pressure)

Case	Experimental Results [atm]	Scaling Study		MLP Prediction	
		P[atm]	Error[%]	P[atm]	Error[%]
1	1.88	2.47	31.7	1.71	8.9
2	1.88	2.49	32.6	1.73	8.1
3	3.66	4.75	29.8	3.72	1.7
4	4.29	5.62	30.9	4.24	1.3
5	4.35	5.62	29.0	4.24	2.7
6	4.36	5.77	32.4	4.28	1.8
7	2.94	3.85	30.8	2.78	5.5
8	4.86	6.55	34.7	4.67	4.0
9	7.07	9.59	35.6	6.76	4.0
		Avg.	32.0	Avg.	4.2

Table 4.7: Comparing JAXA 0.75 MW heater results (Arc-voltage, Mass averaged enthalpy and efficiency)

Case	Experiment Results			Scaling Study Results			Scaling Study Error (%)			MLP Prediction Resutls			MLP Prediction Error (%)		
	V[V]	H[MJ/kg]	E	V[V]	H[MJ/kg]	E	V	H	E	V[V]	H[MJ/kg]	E	V	H	E
1	816	14.20	0.563	955	13.38	0.467	17.0	5.8	17.1	960	13.29	0.576	17.6	6.4	2.3
2	911	13.72	0.575	1089	13.38	0.491	19.6	2.5	14.6	1002	13.12	0.582	10.0	4.4	1.2
3	1041	13.40	0.581	1217	13.38	0.513	16.9	0.1	11.7	1070	12.93	0.588	2.8	3.5	1.2
4	1121	13.10	0.588	1340	13.38	0.533	19.6	2.1	9.4	1140	12.76	0.593	1.7	2.6	0.8
5	1280	12.70	0.598	1459	13.38	0.550	13.9	5.3	7.9	1210	12.59	0.598	5.5	0.8	0.0
6	1381	12.22	0.608	1574	13.38	0.567	13.9	9.5	6.8	1279	12.43	0.602	7.4	1.7	1.0
7	759	19.09	0.508	806	16.55	0.411	6.1	13.3	19.1	928	18.48	0.527	22.2	3.2	3.8
8	839	18.50	0.521	919	16.55	0.432	9.5	10.6	17.0	969	18.08	0.535	15.5	2.3	2.8
9	934	18.29	0.537	1027	16.55	0.452	10.0	9.5	15.9	1011	17.67	0.543	8.2	3.4	1.2
10	1020	17.91	0.548	1130	16.55	0.469	10.8	7.6	14.4	1052	17.27	0.551	3.1	3.6	0.6
11	1109	17.59	0.563	1230	16.55	0.484	10.9	5.9	13.9	1093	16.86	0.559	1.5	4.2	0.6
12	1191	17.01	0.572	1327	16.55	0.499	11.5	2.7	12.8	1132	16.51	0.566	5.0	2.9	1.1
13	716	22.49	0.449	720	19.04	0.378	0.7	15.3	15.9	849	22.34	0.474	18.6	0.7	5.4
14	792	22.17	0.467	821	19.04	0.398	3.7	14.1	14.9	886	21.90	0.481	11.8	1.2	2.9
15	878	21.68	0.484	918	19.04	0.415	4.5	12.2	14.3	924	21.46	0.488	5.2	1.1	0.8
16	947	21.36	0.504	1010	19.04	0.431	6.7	10.9	14.5	962	21.01	0.495	1.7	1.6	1.7
17	1018	21.07	0.520	1100	19.04	0.445	8.0	9.6	14.4	1001	20.57	0.502	1.7	2.4	3.5
18	1088	20.70	0.541	1187	19.04	0.459	9.0	8.0	15.3	1039	20.13	0.509	4.5	2.7	5.9
						Avg.	10.7	8.1	13.9			Avg.	8.0	2.7	2.1

Table 4.8: Comparing AEDC 5 MW heater results (Arc-voltage, Mass averaged enthalpy and efficiency)

Case	Experiment Results			Scaling Study Results			Scaling Study Error (%)			MLP Prediction Resutls			MLP Prediction Error (%)		
	V[V]	H[MJ/kg]	E	V[V]	H[MJ/kg]	E	V	H	E	V[V]	H[MJ/kg]	E	V	H	E
1	2080	14.89	0.343	1673	16.84	0.482	19.6	13.0	40.6	1609	14.21	0.362	22.6	4.6	5.5
2	2080	14.01	0.415	1857	15.50	0.514	10.7	10.6	24.0	1756	12.96	0.386	15.6	7.5	6.9
3	2120	16.28	0.324	1604	17.74	0.467	24.3	9.1	44.2	1527	14.79	0.349	27.9	9.0	7.7
4	3300	12.39	0.430	3025	16.20	0.614	8.3	30.8	42.8	3000	12.01	0.428	9.1	3.0	0.5
5	3360	10.67	0.471	3307	14.60	0.655	1.6	36.8	39.1	3302	10.62	0.443	1.7	0.5	5.9
6	3300	13.87	0.385	2770	17.54	0.580	16.1	26.5	50.6	2617	13.11	0.410	20.7	5.5	6.4
7	4230	10.85	0.456	4158	16.23	0.694	1.7	49.6	52.3	4205	10.58	0.448	0.6	2.4	1.8
8	4465	12.26	0.426	4014	17.36	0.672	10.1	41.6	57.7	4034	10.99	0.432	9.7	10.4	1.4
9	4830	10.35	0.420	4878	17.88	0.719	1.0	72.8	71.1	5047	10.90	0.429	4.5	5.3	2.1
10	3544	13.69	0.349	3010	18.25	0.592	15.1	33.3	69.6	2799	12.76	0.406	21.0	6.8	16.3
11	3016	11.96	0.381	2777	16.94	0.586	7.9	41.7	53.9	2685	12.84	0.416	11.0	7.4	9.1
12	3285	11.83	0.370	2945	17.13	0.598	10.3	44.8	61.6	2854	12.60	0.420	13.1	6.6	13.4
13	3050	14.75	0.345	2408	18.28	0.543	21.0	24.0	57.3	2142	14.10	0.393	29.8	4.4	13.9
14	3460	14.01	0.420	2926	16.89	0.599	15.4	20.5	42.6	2852	12.54	0.421	17.6	10.5	0.2
15	4980	9.90	0.412	4917	17.27	0.728	1.3	74.5	76.7	5078	10.44	0.433	2.0	5.5	5.0
						Avg.	11.0	35.3	52.3			Avg.	13.8	6.0	6.4

Table 4.9: Comparing NASA 60 MW IHF heater results (Arc-voltage, Mass averaged enthalpy and efficiency)

Case	Experiment Results			Scaling Study Results			Scaling Study Error (%)			MLP Prediction Resutls			MLP Prediction Error (%)		
	V[V]	H[MJ/kg]	E	V[V]	H[MJ/kg]	E	V	H	E	V[V]	H[MJ/kg]	E	V	H	E
1	2998	17.89	0.402	4594	34.92	0.511	53.2	95.2	27.2	3208	20.07	0.444	7.0	12.2	10.7
2	2998	18.22	0.411	4621	34.92	0.512	54.1	91.7	24.7	3215	20.07	0.445	7.3	10.2	8.4
3	4545	18.71	0.523	7345	34.92	0.613	61.6	86.6	17.2	4437	18.69	0.513	2.4	0.1	2.0
4	5044	18.75	0.532	8290	34.92	0.643	64.3	86.2	20.7	5102	17.89	0.533	1.1	4.6	0.1
5	5108	18.22	0.542	8290	34.92	0.643	62.3	91.7	18.7	5102	17.89	0.533	0.1	1.8	1.6
6	5133	17.89	0.543	8457	34.92	0.648	64.7	95.2	19.3	5215	17.81	0.536	1.6	0.4	1.4
7	3560	25.48	0.332	4613	46.61	0.471	29.6	82.9	41.7	3257	28.39	0.358	8.5	11.4	7.7
8	4697	24.04	0.403	6767	46.61	0.546	44.0	93.9	35.6	4596	24.83	0.398	2.1	3.3	1.3
9	5988	23.47	0.449	8901	46.61	0.608	48.7	98.6	35.3	6052	23.43	0.464	1.1	0.1	3.3
						Avg.	53.6	91.3	26.7			Avg.	3.5	4.9	4.0

Table 4.10: Average error comparison between scaling study and MLP results, [%]

	Scaling Study				MLP Prediction			
	Pressure	Arc-voltage	Enthalpy	Efficiency	Pressure	Arc-voltage	Enthalpy	Efficiency
JAXA 0.75 MW	2.0	10.7	8.1	13.9	7.1	8.0	2.7	2.1
AEDC 5 MW	14.5	11.0	35.3	52.3	52.3	3.0	13.8	6.4
NASA 60 MW	32.0	53.6	91.3	91.3	26.7	4.2	3.5	4.0

4.3 An Example of Sizing a Segmented Type Arc-Heater

To help understand an arc-heater sizing and performance prediction method using the MLP trained model, sizing and performance prediction for a 10 MW segmented type arc-heater are performed as an example. For efficient prediction, using a scaling study or references of similar power heaters, estimate the input range that might satisfy the requirements, and then predict performance parameters using a trained model by MLP to determine the size or operating condition of the heater. The method and procedure are as follows.

First, select the pressure and enthalpy of the flow to be experimented with using an arc-heater. As the requirements for the example heater, the heater chamber pressure is 20 atm and the mass averaged enthalpy is 20 MJ/kg or more.

Second, estimate the heater current that can satisfy the required enthalpy. Calculate or estimate the range of current that can satisfy the required enthalpy using scaling study or heater references. For example, the relationship between current and enthalpy using the scaling study can be shown in Figure 4.6, and the current to generate enthalpy of 20MJ/kg should be 800 A or more.

Third, estimate the maximum mass flow rate that can be experimented. The mass flow rate is predicted using the given power, required enthalpy, and estimated efficiency. Heater efficiency varies depending on its size, but after assuming efficiency as 0.4 for initial sizing, the mass flow rate is calculated using Equations (4.6) and (4.7).

$$\eta\text{(Efficiency)} \times P\text{(Power)} = h\text{(Enthalpy)} \times \dot{m}\text{(Mass flow rate)} \tag{4.6}$$

$$\dot{m} = \frac{\eta P}{h} = \frac{0.4 \times 10MW}{20MJ/kg} = 0.2kg/s \tag{4.7}$$

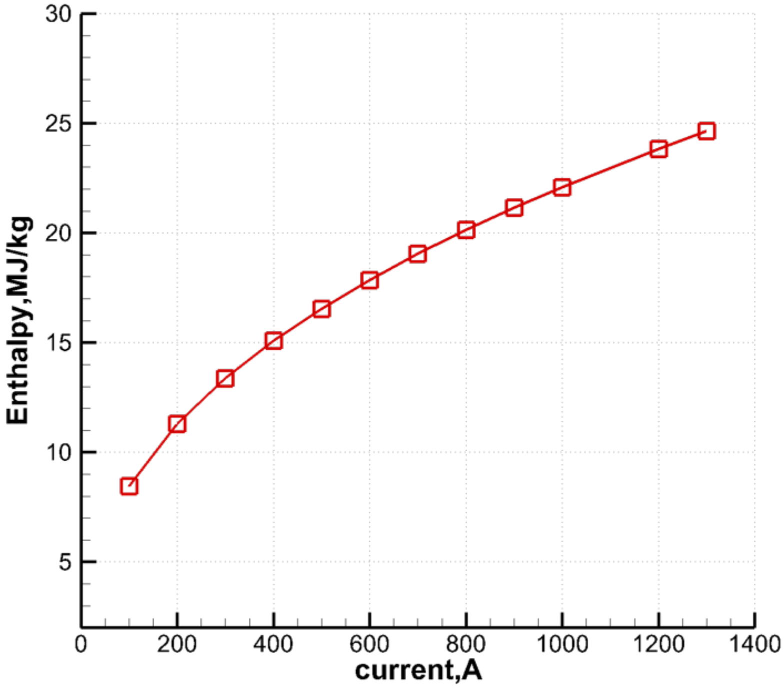

Figure 4.6: Relation of current and enthalpy using scaling study

Fourth, estimate the nozzle throat area or diameter. Estimate the nozzle throat area (A^*) that satisfies the required pressure of 20 atm using the previously predicted current and mass flow rate. The nozzle throat area can be calculated using Equation (4.1) of the scaling study or Equation (4.8) of the quasi-1D compressible flow theory [61].

$$A^* = \frac{1}{K}\frac{\sqrt{T_0}}{P_0}\dot{m} \tag{4.8}$$

Where,

$$K = \sqrt{\frac{\gamma}{R}}(\frac{2}{\gamma+1})^{\frac{\gamma+1}{2(\gamma-1)}}$$

The throat area estimated using Equation (4.8) is 4.15 cm^2, and the diameter is 2.3 cm. Therefore, the throat diameter should be less than 2.3 cm, and in the present example case, the throat diameter range from 1.4 cm to 2.3 cm is used.

Fifth, predict the pressure using the trained model. After inputting a certain range of the estimated mass flow rate, current, and nozzle throat as shown in Figure 4.7, the configuration parameters and operating conditions are selected by comparing the predicted pressure value with the required pressure.

Finally, predict the remaining performance parameters such as enthalpy, efficiency, and arc-voltage using the trained model. The range of values for the length and diameter of the segmented arc-heater considering the installation space or manufacturing and the estimated pressure, mass flow rate, and current are used as input. Then, as shown in Figure 4.8, the size of the heater can be determined based on the predicted performance of the heater.

Input Output

Nozzle Throat D	Mass Flow Rate	Current	Predicted P	Required P	P Difference
1.4	50	1000	6.77	20	-13.23
1.4	100	1000	15.23	20	-4.77
1.4	150	1000	33.06	20	13.06
1.4	200	1000	65.69	20	45.69
1.4	250	1000	87.76	20	67.76
1.4	300	1000	104.30	20	84.30
1.4	350	1000	119.22	20	99.22
1.4	400	1000	132.82	20	112.82
1.4	50	2000	8.62	20	-11.38
1.4	100	2000	20.36	20	0.36
1.4	150	2000	51.63	20	31.63
1.4	200	2000	83.13	20	63.13
1.4	250	2000	107.38	20	87.38
1.4	300	2000	125.99	20	105.99
1.4	350	2000	141.70	20	121.70
1.4	400	2000	156.13	20	136.13
1.4	50	3000	9.38	20	-10.62
1.4	100	3000	20.93	20	0.93
1.4	150	3000	48.24	20	28.24
1.4	200	3000	80.26	20	60.26
1.4	250	3000	110.17	20	90.17
1.4	300	3000	131.06	20	111.06
1.4	350	3000	148.25	20	128.25
1.4	400	3000	164.01	20	144.01
1.6	50	1000	5.74	20	-14.26
1.6	100	1000	10.34	20	-9.66
1.6	150	1000	17.40	20	-2.60
1.6	200	1000	38.41	20	18.41
1.6	250	1000	65.84	20	45.84
1.6	300	1000	84.31	20	64.31
1.6	350	1000	100.55	20	80.55
1.6	400	1000	115.34	20	95.34
1.6	50	2000	7.11	20	-12.89
1.6	100	2000	14.42	20	-5.58
1.6	150	2000	34.39	20	14.39
1.6	200	2000	63.25	20	43.25
	⋮		⋮		

Figure 4.7: Inputs and outputs of predicting heater pressure using MLP (Example case)

Input | Output

Constrictor D	Constrictor L	Constrictor L/D	Nozzle Throat D	Mass Flow Rate	Current	Predicted V	Predicted h	Predicted E	Required h	Error (h, %)
2.5	25	10	1.6	50	1000	878	22.4	0.45	20	11.88
2.5	25	10	1.6	100	1000	1469	18.0	0.54	20	9.81
2.5	25	10	1.6	150	1000	2139	15.2	0.60	20	24.09
2.5	25	10	1.6	200	1000	2643	13.6	0.62	20	32.13
2.5	25	10	1.6	250	1000	2950	12.7	0.64	20	36.45
2.5	25	10	1.6	300	1000	3229	12.3	0.66	20	38.45
2.5	25	10	1.6	350	1000	3513	12.1	0.67	20	39.62
2.5	25	10	1.6	400	1000	3806	12.0	0.68	20	40.01
2.5	25	10	1.6	450	1000	4121	12.0	0.70	20	40.01
2.5	25	10	1.6	50	2000	1180	28.7	0.34	20	43.46
2.5	25	10	1.6	100	2000	1165	26.6	0.39	20	33.13
2.5	25	10	1.6	150	2000	1739	23.7	0.47	20	18.56
2.5	25	10	1.6	200	2000	2213	22.0	0.52	20	10.05
2.5	25	10	1.6	250	2000	2573	20.6	0.55	20	2.95
2.5	25	10	1.6	300	2000	2911	19.6	0.56	20	2.20
2.5	25	10	1.6	350	2000	3232	18.5	0.58	20	7.26
2.5	25	10	1.6	400	2000	3612	17.3	0.60	20	13.68
2.5	25	10	1.6	450	2000	3957	16.6	0.62	20	16.85
2.5	25	10	1.6	50	3000	1611	31.9	0.31	20	59.70
2.5	25	10	1.6	100	3000	1381	30.3	0.33	20	51.64
2.5	25	10	1.6	150	3000	1544	28.5	0.37	20	42.58
2.5	25	10	1.6	200	3000	1951	26.7	0.42	20	33.30
2.5	25	10	1.6	250	3000	2261	25.4	0.46	20	26.93
2.5	25	10	1.6	300	3000	2531	24.2	0.49	20	20.98
2.5	25	10	1.6	350	3000	2827	23.1	0.52	20	15.30
2.5	25	10	1.6	400	3000	3139	22.3	0.54	20	11.26
2.5	25	10	1.6	450	3000	3433	21.4	0.56	20	7.23
2.5	50	20	1.6	50	1000	1695	19.9	0.51	20	0.43
2.5	50	20	1.6	100	1000	2599	15.9	0.55	20	20.30
2.5	50	20	1.6	150	1000	3303	14.7	0.57	20	26.42
2.5	50	20	1.6	200	1000	3822	14.1	0.59	20	29.51
2.5	50	20	1.6	250	1000	4199	13.7	0.61	20	31.67
2.5	50	20	1.6	300	1000	4518	13.4	0.62	20	33.08
2.5	50	20	1.6	350	1000	4825	13.2	0.64	20	34.11
2.5	50	20	1.6	400	1000	5119	13.1	0.66	20	34.65
2.5	50	20	1.6	450	1000	5411	12.9	0.67	20	35.27
2.5	50	20	1.6	50	2000	1277	27.7	0.35	20	38.42
2.5	50	20	1.6	100	2000	1832	24.0	0.42	20	20.22
2.5	50	20	1.6	150	2000	2329	20.2	0.49	20	1.11
2.5	50	20	1.6	200	2000	3091	17.2	0.51	20	14.16
2.5	50	20	1.6	250	2000	3621	16.4	0.53	20	17.93
2.5	50	20	1.6	300	2000	4022	16.1	0.55	20	19.74
		⋮					⋮			

Figure 4.8: Inputs and outputs of predicting heater parameters using MLP (Example case)

CHAPTER 5. CONCLUSIONS

5.1 Conclusion

In order to understand the internal flow characteristics of an arc-heated wind tunnel, the analysis region of the existing arc heater analysis program, ARCFLO4 code, was improved enable to analyze the full system of the wind tunnel. The calculation range of ARCFLO4, which could only calculate the thermodynamic properties and transport coefficient of high-temperature, high-pressure, and low-velocity equilibrium air, has been expanded to allow low-pressure, low-temperature, and supersonic/hypersonic calculations. When a value is out of the calculation range, it is calculated using the perfect gas equation of state, and the numerical discontinuous phenomenon that occurs at the boundary of the calculation range is improved by using the smoothing function. To validate and verify the numerical results in the low-pressure, low-temperature, and supersonic/hypersonic domains, NASA Langley AHSTF Mach 4.9 and Mach 6 nozzle were analyzed and compared with experimental values.

Using the numerical analysis program, a flow analysis was performed on the plenum mixing chamber with a heater nozzle, which ensures the stability of the arc plasma, and its characteristics were analyzed. When there is a heater nozzle, it was confirmed that the flow inside the heater and its performance do not change due to the choking effect caused by the heater nozzle even if the flow entering the plenum mixing chamber changes. As the flow inside the PM is supersonic, the mixing possibility of the main flow and the additional flow was identified and the effect of the amount and direction of the additional injected gas was analyzed. Although about 30 % of total pressure and enthalpy loss occurred by the heater nozzle, there was an advantage in that the mixing length was shortened inside the chamber. As a method to reduce the loss of the main flow by the heater nozzle, it was proposed to increase the nozzle throat area or reduce the nozzle exit area so that the Mach number at the exit of the heater nozzle can be reduced, and the parametric study was performed to confirm that increasing the nozzle throat area is effective in reducing flow loss and heat flux.

In addition, flow analysis of diffusers was performed to analyze the characteristics of representative types of diffusers; then, a diffuser with a new configuration that could compensate for the shortcomings of existing diffusers was proposed. Because the center-body is located in the diverging section (i.e. subsonic region), the novel diffuser has the advantage of reducing the total pressure loss due to the shock wave and widening the cooling area. As a result of the performance evaluation of three types of diffusers, it was confirmed that the proposed diffuser has advantages in exit temperature and velocity while maintaining efficiency. In particular, the exit temperature of the novel diffuser was 11 $\%$ lower than that of the cylindrical second throat diffuser under the same condition.

Finally, a multi-layer perceptron model that can design and predict the performance of an arc-heated wind tunnel faster than CFD analysis was introduced. By building a database according to the design variables and operating conditions of the arc-heated wind tunnel, its performance can be predicted by artificial neural networks. As an example, a database of segmented type arc-heater was built and the possibility of performance prediction using the MLP-trained model was confirmed by comparing the results with the experimental values of existing devices.

In the future, the analysis code improved in the present study and the physical characteristics of the arc-heated wind tunnel analyzed through flow analysis will help design a novel arc-heated wind tunnel, predict performance, and design additional devices for upgrading facilities. In addition, by simulating an experiment, the physical phenomena and values that are difficult to observe and measure can be predicted, and complementary research such as analysis of basic physical phenomena occurring in experimental models will be possible. Moreover, since the code can be used not only for an arc-heated wind tunnel analysis but also for flow analysis inside mechanical systems in various industries, it is possible to predict the physical properties of a device with a similar operating mechanism to that of a wind tunnel.

5.2 Future Works

Further research on analysis codes, arc-heated wind tunnel manufacturing and operating based on the numerical analysis, and performance prediction using database remain to be done.

In relation to the analysis code, three main tasks are to be performed: expansion of the governing equation, combining electric/magnetic field model, and adoption of a time-efficient calculation scheme. In the present study, the analysis code is improved, and possible to analyze segmented, Huels, and MPD heaters, but the accurate analysis for ICP heater is low. This is because, due to the operating characteristics of the ICP heater, the tangential direction momentum equation must be added for the ICP heater analysis, and the magnetic potential equation as well as the electric field analysis must be additionally considered. However, expanding the governing equation and adding the magnetic field model may increase the calculation time. This can be disadvantageous to analyze using CFD in a short time. Therefore, it will be necessary to improve the arc-heated wind tunnel analysis code using recently used time-efficient computational schemes such as the generated minimum residual method (GMRES).

Regarding the fabrication and operation of the actual wind tunnels, an optimal design for the heater nozzle and center-body of the novel diffuser is required. The optimal design of the heater nozzle should be performed in a direction in which the heat flux of the heater nozzle throat is small and the flow loss is reduced by lowering the exit Mach number. The optimal configuration of the center-body should not cause flow separation in the diverging section and should be performed in a direction that can lower the exit temperature as much as possible. For this purpose, three variables can be changed: angle, diameter, and length of the center-body. As the diameter increases, the cooling area widens, but if it is too large, flow choking may occur in the diverging section rather than the diffuser throat due to the effective area reduction by the center-body, and the converging and diverging angle of the center-body should be maintained at 3 to 5 degrees so that flow separation does not occur. Therefore, the optimal design method depending on the length is the most realistic. In addition, this study numerically simulated the experimental process, so it did not suggest the method for mounting the support for the experimental model and the center-body of the diffuser. Therefore, numerical or experimental research should be conducted from the viewpoint of practical problems that occur when manufacturing and experimenting with actual devices.

Finally, several follow-up studies are needed to improve performance prediction accuracy. First, it is necessary to expand the database using more numerical results and design variables. Second, use low-fidelity data to reduce the increased learning time due to the expanded database. Third, find unknown parameters that affect the results in the database. Also, since research on artificial neural network models is being actively conducted and various models are being developed, it would be helpful to study and introduce models suitable for the design and performance prediction of arc-heated wind tunnels.

References

[1] E. Felderman, R. Chapman, J. Jacocks, D. Horn, and W. Bruce III, "High-pressure arc heater development and modeling-status and requirements," *Journal of propulsion and power*, vol. 12, no. 6, pp. 1044–1052, 1996.

[2] R. Smith, D. Wagner, and J. Cunningham, "A survey of current and future plasma arc-heated test facilities for aerospace and commercial applications," in *36th AIAA Aerospace Sciences Meeting and Exhibit*, (Reno, NV), p. 146, 1998.

[3] A. Balter Peterson, F. Nichols, B. Mifsud, and W. Love, "Arc jet testing in nasa ames research center thermophysics facilities," in *AlAA 4th International Aerospace Planes Conference*, (0rlando, FL), p. 5041, 1992.

[4] L. Davis and D. Carver, "Initial calibration of the heat-h2 arc-heated wind tunnel," tech. rep., ARNOLD ENGINEERING DEVELOPMENT CENTER ARNOLD AFB TN, 1992.

[5] S. R. Thomas and R. W. Guy, "Expanded operational capabilities of the langley mach 7 scramjet test facility," tech. rep., The National Aeronautics and Space Administration, 1983.

[6] P. Endlich, M. Auweter-Kurtz, G. Herdrich, S. Löhle, and M. Winter, "The inductively heated plasma wind tunnel pwk3 as a means for emission experiments to rebuild radiation test cases," in *Radiation of High Temperature Gases in Atmospheric Entry*, vol. 533, pp. 55–62, 2003.

[7] B. Bottin, O. Chazot, M. Carbonaro, V. Van Der Haegen, and S. Paris, "The vki plasmatron characteristics and performance," tech. rep., VON KARMAN INST FOR FLUID DYNAMICS RHODE-SAINT-GENESE (BELGIUM), 2000.

[8] S. Laure, M. Auweter-Kurtz, S. Fasoulas, H. Habiger, and W. Roeck, "The irs plasma wind tunnels as a tool for the investigation of planet entry missions," in *28th Joint Propulsion Conference and Exhibit*, (Nashville, TL), p. 3886, 1992.

[9] S. Loehle, F. Zander, M. Eberhart, T. Hermann, A. Meindl, B. Massuti-Ballester, D. Leiser, F. Hufgard, A. S. Pagan, G. Herdrich, *et al.*, "Assessment of high enthalpy flow conditions for re-entry aerothermodynamics in the plasma wind tunnel facilities at irs," *CEAS Space Journal*, vol. 14, no. 2, pp. 395–406, 2022.

[10] R. Pugazenthi and A. C. McIntosh, "Design and performance analysis of a supersonic diffuser for plasma wing tunnel," *International Journal of Aerospace and Mechanical Engineering*, vol. 5, no. 8, pp. 1682–1687, 2011.

[11] G. Jeong, *A Study on Design and Manufacture of Arc Heater Facility Using Computational Fluid Dynamics*. PhD thesis, Graduate school of Seoul national university, 2013.

[12] P. W. Agostinelli, E. Trifoni, and R. Savino, "Aerothermodynamic analyses and redesign of ghibli plasma wind tunnel hypersonic diffuser," *Aerospace Science and Technology*, vol. 87, pp. 218–229, 2019.

[13] N. Fouladi and M. Farahani, "Numerical investigation of second throat exhaust diffuser performance with thrust optimized parabolic nozzles," *Aerospace Science and Technology*, vol. 105, p. 106020, 2020.

[14] W. Nicolet, C. Shepard, K. Clark, A. Balakrishnan, and J. Kesselring, "Analytical and design study for a high-pressure, high-enthalpy constricted arc heater," tech. rep., ACUREX CORP/AEROTHERM MOUNTAIN VIEW CA, 1975.

[15] K. H. Kim, O. H. Rho, and C. Park, “Navier-stokes computation of flows in arc heaters,” *Journal of thermophysics and heat transfer*, vol. 14, no. 2, pp. 250–258, 2000.

[16] T. Sakai, K. Sawada, and M. Mitsuda, “Application of planck-rosseland-gray model for high-enthalpy arc heaters,” *Journal of thermophysics and heat transfer*, vol. 15, no. 2, pp. 176–183, 2001.

[17] J.-I. Lee, C. Kim, and K.-H. Kim, “Accurate computations of arc-heater flows using two-equation turbulence models,” *Journal of thermophysics and heat transfer*, vol. 21, no. 1, pp. 67–76, 2007.

[18] J. I. Lee, G. Jeong, and K. H. Kim, “Computation of segmented arc-heater flows considering injection of electrode shield gas,” *Journal of Thermophysics and Heat Transfer*, vol. 25, no. 2, pp. 201–212, 2011.

[19] W. Brainerd, “Fortran 77,” *Communications of the ACM*, vol. 21, no. 10, pp. 806–820, 1978.

[20] J. D. Anderson, *Hypersonic and high temperature gas dynamics*. Aiaa, 2000.

[21] Y. Takahashi, H. Kihara, and K.-i. Abe, “Numerical investigation of nonequilibrium plasma flows in constrictor-and segmented-type arc heaters,” *Journal of thermophysics and heat transfer*, vol. 24, no. 1, pp. 31–39, 2010.

[22] J.-I. Lee, *(A) study on numerical modeling for flow analysis in arc-heaters*. PhD thesis, Graduate school of Seoul national university, 2007.

[23] B. J. McBride, *Computer program for calculation of complex chemical equilibrium compositions and applications*, vol. 2. NASA Lewis Research Center, 1996.

[24] R. N. Gupta, J. M. Yos, R. A. Thompson, and K.-P. Lee, “A review of reaction rates and thermodynamic and transport properties for an 11-species air model for

chemical and thermal nonequilibrium calculations to 30000 k," tech. rep., The National Aeronautics and Space Administration, 1990.

[25] J. M. Yos, "Transport properties of nitrogen, hydrogen, oxygen, and air to 30,000 k," tech. rep., AVCO CORP WILMINGTON MA RESEARCH AND ADVANCED DEVELOPMENT DIV, 1963.

[26] J. Bae, *Development of Equilibrium Flow CFD Code Using CEA Database and Prediction on Ablation of SiC Coating Nozzle*. Master's thesis, Graduate school of Seoul national university, 2017.

[27] H. T. Nagamatsu, J. Workman, and R. Sheer Jr, "Hypersonic nozzle expansion of air with atom recombination present," *Journal of the Aerospace Sciences*, vol. 28, no. 11, pp. 833–837, 1961.

[28] H. T. Nagamatsu and R. E. Sheer JR, "Vibrational relaxation and recombination of nitrogen and air in hypersonic nozzle flows," *AIAA Journal*, vol. 3, no. 8, pp. 1386–1391, 1965.

[29] W. Sutherland, "Lii. the viscosity of gases and molecular force," *The London, Edinburgh, and Dublin Philosophical Magazine and Journal of Science*, vol. 36, no. 223, pp. 507–531, 1893.

[30] J. Park, *CFD Code Development for Simulations of High-Voltage Gas Circuit Breakers using Overset Method with Radiation and Ablation Modelling*. Master's thesis, Graduate school of Seoul national university, 2014.

[31] V. R. Watson and E. B. Pegot, *Numerical calculations for the characteristics of a gas flowing axially through a constricted arc*, vol. 4042. National Aeronautics and Space Administration, 1967.

[32] T. Sakai and J. Olejniczak, "Improvements in a navier-stokes code for arc heater flows," in *36th AIAA Thermophysics Conference*, (0rlando, FL), p. 3782, 2003.

[33] W. P. Jones and B. E. Launder, “The prediction of laminarization with a two-equation model of turbulence,” *International journal of heat and mass transfer*, vol. 15, no. 2, pp. 301–314, 1972.

[34] D. C. Wilcox *et al.*, *Turbulence modeling for CFD*, vol. 2. DCW industries La Canada, CA, 1998.

[35] F. R. Menter, “Two-equation eddy-viscosity turbulence models for engineering applications,” *AIAA journal*, vol. 32, no. 8, pp. 1598–1605, 1994.

[36] K. H. Kim, C. Kim, and O.-H. Rho, “Methods for the accurate computations of hypersonic flows: I. ausmpw+ scheme,” *Journal of computational physics*, vol. 174, no. 1, pp. 38–80, 2001.

[37] M.-S. Liou, “Ten years in the making-ausm-family,” in *15th AIAA Computational Fluid Dynamics Conference*, (Anaheim, CA), p. 2521, 2001.

[38] M.-S. Liou, “A sequel to ausm: Ausm+,” *Journal of computational Physics*, vol. 129, no. 2, pp. 364–382, 1996.

[39] B. Van Leer, “Towards the ultimate conservative difference scheme. v. a second-order sequel to godunov’s method,” *Journal of computational Physics*, vol. 32, no. 1, pp. 101–136, 1979.

[40] P. K. Sweby, “High resolution schemes using flux limiters for hyperbolic conservation laws,” *SIAM journal on numerical analysis*, vol. 21, no. 5, pp. 995–1011, 1984.

[41] A. Harten, “High resolution schemes for hyperbolic conservation laws,” *Journal of computational physics*, vol. 135, no. 2, pp. 260–278, 1997.

[42] S. Yoon and A. Jameson, “Lower-upper symmetric-gauss-seidel method for the euler and navier-stokes equations,” *AIAA journal*, vol. 26, no. 9, pp. 1025–1026, 1988.

[43] K.-H. Kim, “Numerical investigation of plasma flows inside segmented constrictor type arc-heater,” *Aeronautics and Astronautics*, pp. 97–124, 2011.

[44] T. Sakai, T. Suzuki, K. Fujita, and T. Ito, “Calculation of high-enthalpy aerothermal environment in an arcjet facility,” *Journal of thermophysics and heat transfer*, vol. 21, no. 1, pp. 249–251, 2007.

[45] J. I. Lee, G. Herdrich, G. Jeong, and K. H. Kim, “Numerical parameter study of low-electric-power segmented arc heaters,” *Journal of thermophysics and heat transfer*, vol. 26, no. 2, pp. 271–285, 2012.

[46] R. Guy, R. Rogers, R. Puster, K. Rock, and G. Diskin, “The nasa langley scramjet test complex,” in *32nd Joint Propulsion Conference and Exhibit*, (Lake Buena Vista,FL), p. 3243, 1996.

[47] W. Winovich, J. Balboni, and A. Balakrishnan, “Experimental and analytical derivation of arc-heater scaling laws for simulating high-enthalpy environments for aeroassisted orbital transfer vehicle application,” in *20th Thermophysics Conference*, (Williams burg, VA), p. 1006, 1985.

[48] C. Park, “Experimental evaluation of real-gas phenomena in high-temperature aerothermal test facilities-a review,” in *Advanced Measurement and Ground Testing Conference*, (New Orleans, LA), p. 2207, 1996.

[49] D. W. Witte, R. G. Irby, A. H. Auslender, and K. E. Rock, “1998 calibration of the mach 4.7 and mach 6 arc-heated scramjet test facility nozzles,” tech. rep., The National Aeronautics and Space Administration, 2004.

[50] W. MacDermott, D. Horn, and C. Fisher, “Flow contamination and flow quality in arc heaters used for hypersonic testing,” in *17th Aerospace Ground Testing Conference*, (Nashville, TN), p. 4028, 1992.

[51] D. Horn, W. Bruce, III, and E. Felderman, "Results and predictions for the new h3 arc heater at aedc," in *27th Plasma Dynamics and Lasers Conference*, (New Orleans, LA), p. 2316, 2013.

[52] M. Büscher, B. Esser, K. Kindler, and V. List, "Developments at the arc heated facility lbk of dlr," in *Aerothermodynamics for space vehicles*, vol. 367, p. 357, 1995.

[53] M. Milligan and J. Bailey, "Low-density hypervelocity wind tunnel diffuser performance," tech. rep., TENNESSEE UNIV KNOXVILLE, 1963.

[54] R. Savino, R. Monti, and A. Esposito, "Behaviour of hypersonic wind tunnels diffusers at low reynolds numbers," *Aerospace science and technology*, vol. 3, no. 1, pp. 11–19, 1999.

[55] R. Hermann, "Diffuser efficiency and flow process of supersonic wind tunnels with free jet test section," tech. rep., Air Materiel Command Wright-Patterson AFB OH, 1950.

[56] G. vanRossum, "Python reference manual," tech. rep., Department of Computer Science [CS] R 9525, 1995.

[57] T. Hastie, R. Tibshirani, and J. H. Friedman, *The elements of statistical learning: data mining, inference, and prediction*. New York: springer, 2009.

[58] A. F. Agarap, "Deep learning using rectified linear units (relu)," *arXiv preprint arXiv:1803.08375*, 2018.

[59] X. Glorot and Y. Bengio, "Understanding the difficulty of training deep feedforward neural networks," in *Proceedings of the thirteenth international conference on artificial intelligence and statistics*, pp. 249–256, JMLR Workshop and Conference Proceedings, 2010.

[60] D. D. Horn and S. G. A. Brown, "Results of testing the aedc 5-mw segmented arc heater," tech. rep., ARNOLD ENGINEERING DEVELOPMENT CENTER ARNOLD AFB TN, 1974.

[61] J. D. Anderson *et al.*, "Fundamentals of aerodynamics," 2011.

초 록

초고속 비행체, 재진입 비행체의 내열 소재 및 열 보호 시스템 연구에 필수적인 지상 시험 장비로는 아크 플라즈마를 이용하여 고엔탈피 유동을 모사하는 아크 가열식 풍동이 있다. 아크 가열식 풍동은 유인 우주선의 안정성 확보를 위해 1950년대부터 연구가 수행되어 미국, 유럽, 러시아 등 항공우주 선진국에서는 다양한 규모의 장치를 구축하여 현재까지 사용하고 있다. 그러나 국내에는 아크 가열식 시험 장비가 매우 부족한 상황이며, 구축 비용의 절감을 위해 현존하는 연구시설의 기존 인프라를 이용한 장치의 구축이 요구된다. 국외의 시험장비들 또한 다른 행성으로의 재진입 연구를 수행하기 위해 개선이 지속적으로 필요한 상황이다. 따라서 본 연구는 아크 가열식 풍동의 설계, 개선 및 확장에 유용하게 적용할 수 있는 전산 해석 프로그램, 구성요소의 형상 설계 및 분석, 인공신경망 모델을 이용한 성능 예측 연구를 수행하였으며, 그 내용은 다음과 같다.

1. 해석 코드 개선 및 검증

아크히터 해석용 코드인 ARCFLO4를 아크 가열식 풍동장치 전체 시스템의 유동 해석을 위한 코드로 개선하고 검증하였다. 고압, 고온, 저속의 열적/화학적 평형 아크 플라즈마 해석을 위해 개발된 ARCFLO4 코드를 아크 가열식 풍동의 초음속/극초음속 영역의 유동 해석이 가능하도록 열역학적 변수와 전달계수의 계산 영역을 확장하였다. 또한, 시험장치의 비정상 해석을 위해 dual time stepping 시간 전진기법을 도입하였다. 개선된 유동 해석 코드는 JAXA 0.75 MW 아크히터, NASA Ames 20 MW IHF 아크히터, 그리고 NASA Langely의 마하4.9, 마하6 노즐의 유동 해석

결과와 실험 값을 비교하여 검증하였다.

2. 플레넘 혼합실과 디퓨저의 새로운 형상 제안 및 특성 분석

아크히터와 노즐 사이에 플레넘 혼합실이 있는 경우, 혼합실 내부의 유동 변화에 대한 아크 플라즈마의 안정성을 보장하기 위해 히터 노즐을 사용한 형상을 제안하였다. 히터 노즐에 의한 질식효과로 플레넘 혼합실 내부의 유동이 변화하여도 상류인 아크히터 내부 유동에 변화가 없음을 확인하였으며, 고온의 히터 유동과 상온의 추가 유입 유동의 혼합이 더 빠르게 발생하는 것을 알 수 있었다. 디퓨저에 대한 수치해석 연구는 대표적인 디퓨저 형상인 중심체형 디퓨저와 2차목 원통형 디퓨저에 대한 유동 해석을 수행하여 각 형상에 대한 장점과 단점을 파악한 후, 효율이 높은 디퓨저 형상을 제안하였다. 새로운 디퓨저의 경우, 중심체가 아음속 영역에 위치하여 디퓨저 효율은 유지되고 중심체에 의한 냉각면적 증가로 출구의 유동 온도가 가장 낮음을 확인하였다.

3. 멀티 레이어 퍼셉트론 모델을 이용한 아크히터 변수 간 상관관계 예측

인공 신경망 모델인 멀티 레이어 퍼셉트론을 이용하여 시험 장치의 성능 예측을 위한 코드를 개발하였다. 세그멘트형 아크히터들의 전산 해석 결과를 이용하여 데이터 베이스를 구축하고 유동 분석을 통해 주요 설계 인자를 선정하여 학습을 수행, 아크히터 변수 간의 상관관계 예측이 가능하도록 하였다. 멀티 레이어 퍼셉트론 모델의 검증을 위해 현존하는 소형, 중형, 대형 아크히터의 성능 변수인 압력, 아크 전압, 엔탈피, 효율을 예측하고 실제 실험값과 비교하였다.

주요어: 아크 가열식 풍동, 전산유체해석, 아크히터, 플레넘 혼합실, 디퓨저, 멀티 레이어 퍼셉트론

학번: 2017-34718

성명: 백진솔